Design of a Microwave-Initiated Pulsed Plasma Thruster (MiPPT)

Jian F. Li, Class of 2006

Submitted to the
Department of Mechanical and Aerospace Engineering
Princeton University
in partial fulfillment of the requirements
of Undergraduate Senior Thesis.

Final Report

May 4, 2006

_____

I pledge my honor that this paper represents my own work in accordance to University regulations.

ABSTRACT

The performance of gas-fed pulsed plasma thrusters (GFPPTs) is dependent on the symmetry of its current sheet. Research has shown that the lack of discharge symmetry in the spark-ignition mechanism of GFPPTs has lead to non-uniform current sheet formation. Furthermore, spark plugs used in the spark-ignition system suffer heavy corrosion rates during operation and can fail prematurely. To improve the lifespan and performance of GFPPTs, this project investigates microwave discharges as an plasma initiation source in GFPPTs. The purpose of this project is to design a microwave-initiated pulsed plasma thruster (MiPPT) and perform all detailed simulations, prototyping, and experimentation. Results indicate that the MiPPT has successfully produced microwave plasma and has been able to induce current sheet formation. Resistance measurements indicate a plasma resistance of 190 mOhm with a standard deviation of 150 mOhm. Inductance measurements indicate that the inductance of the MiPPT discharge circuit is approximately 600-1200 nHenry. Finally, high speed imagery suggests that the current sheet is biased due to asymmetric plasma injection. Future designs of the MiPPT will focus on reducing the inductance of the discharge circuit, improving tuning of the microwave cavity, and developing a system architecture for pulsed operation.

Acknowledgements

I would like to extend my sincerest gratitude and appreciation to the following people and departments:

- Prof. Edgar Choueiri of the Princeton University Electric Propulsion and Plasma Dynamics Laboratory for extending an opportunity for me to explore the field of electric propulsion.
- Glenn Northey of the Princeton University Undergraduate Machine Shop for his guidance and assistance with metal manufacturing.
- Bob Sorenson for his technical assistance with equipment at the Princeton Electric Propulsion and Plasma Dynamics Laboratory.
- Prof. Miles and Princeton Applied Physics Group for microwave leak detector and Imacon 729 LS camera.
- Jo-Ann Love for her continuing support and assistance with all undergraduate issues during these past four years.
- Jimmy Cooley of the Princeton University Electric Propulsion and Plasma Dynamics Laboratory for his guidance and mentorship throughout this project.
- Rob Murray of the Princeton University Electric Propulsion and Plasma Dynamics Laboratory for his insight into microwave engineering throughout this project.
- 2005-2006 McKinzie Senior Thesis Funding Prize for financial support of this project.
- Princeton University School and Engineering and Applied Science for their scholarship and thesis funding.
- Princeton University Mechanical and Aerospace Engineering department for their generosity in fund this project.

Table of Contents

List of Symbols

M_{fuel}	Total mass of fuel	z	Axial distance
M_{total}	Total mass of fuel, structures, and payload.	n	nth order Bessel function of the first kind
V	Velocity	K_c	Cuttoff parameter
g_o	Gravitation force on earth's surface	a	Radial distance
I_{sp}	Specific impulse of a rocket	A	Area of hole
ω_{nmp}	Resonant frequency	P	Ambient Pressure
c	Speed of light in vacuum	T	Ambient Temperature
μ	Permeability of medium	γ	Specific heat
ε	Permittivity of medium	R	Universal gas constant
x_{nm}	mth zero of nth order Bessel function of the first kind	σ_A	Collision cross section
D	Diameter of cylinder	N_e	Electron charge density
p	Number of integer half-wavelengths inside a cavity	D_a	Ambipolar diffusion coefficient
l	Length of cavity	λ	Effective radius of cylinder
E_r	Radial electric field	D_e	Electron diffusion coefficient
E_θ	Azimuthal electricl field	μ_+	Mobility of ions
E_z	Axial electric field	μ_e	Mobility of electrons
H_r	Radial magnetic field	D_+	Ion Diffusion Coefficient
H_θ	Azimuthal magnetic field	T_e	Electron Temperature
H_z	Axial magnetic field	K_b	Boltzman's Constant
ψ	Helmholtz wave function	e	Electron charge

ν_e	Electron collision frequency
R	Radius of cylinder
m_e	Mass of electron
β_{diss}	Dissociative recombination coefficient
q	Charge of capacitors
R	Resistance of circuit
L	Inductance of circuit
C	Capacitance of circuit
Δ	Eigenvalue of LRC circuit

Chapter 1: Introduction

In the past twenty years, demand for a more integrated communication network system has been increasing dramatically. Whether the goal is to deliver high quality digital media entertainment to houses around the globe or input surveillance on one specific country, the means through which all these objectives can be accomplished are geo-centered satellites. While simple low Earth orbit (LEO) satellites can provide coverage to small regions around the world, many of these satellites are required to establish a comprehensive coverage over a broad region of the globe. Hence, commercial satellite ventures and defense contractors are investing more resources on geostationary Earth orbit (GEO) satellites and highly elliptical orbits (HEO), such as Molniya satellites, where coverage spans a much greater area. Because of the larger size and weight of a GEO and Molniya satellite, one can anticipate the cost associated with these higher orbit satellites to be much greater than lower Earth orbits. A significant portion of this weight originated from propellant fuel mass needed for orbit transfers and station-keeping. To reduce the fuel weight and hence the cost of a mission, it follows that the propulsion system would need to be more fuel efficient.

There are two propulsion systems in a GEO or Molniya satellite, each optimized for a specific stages of its mission. The first stage launches the satellite into a LEO parking orbit using a solid chemical rocket, such as Boeing Delta IV or Lockheed-Martin Titan IV. The second stage consists of performing a transfer orbit from LEO to GEO or Molniya, followed by station-keeping for a specified satellite lifetime. Unlike the first stage, the second stage has several different propulsion systems to select from, either liquid hydrogen-oxygen rockets to electrical ion thrusters. It is important to understand that the first stage carries the weight of the second stage. Hence, to reduce the cost of a GEO or Molniya mission, one can either improve the performance of the first stage propulsion system and/ or select a lighter, more efficient propulsion system for the second stage. To obtain a sense of the cost per pound associated with different satellite missions, consider a Boeing Delta IV rocket launch. Delta IV can carry approximately 23,000 pounds of payload into a LEO at a cost of approximately $150 million US dollars. This translates to a cost of around $6,500 per pound of payload. A ten pound improvement of the second stage propulsion system would translate to approximately $65,000 savings.

The weight of the second stage propulsion system includes components from fuel mass and mechanical hardware. The amount of fuel consumed by any propulsion system depends heavily on the performance of the rocket, specifically its specific impulse, I_{sp}. For highly fuel efficient thrusters, such as nuclear or electrical thrusters, its specific impulse is high and fuel expenditure is low. For solid state rockets, it's specific impulse is low and fuel expenditure is high. To obtain a sense of how fuel consumption is dependent on the specific impulse, on can derive a relationship from fundamental momentum conservation relationships relating mass fractions to specific impulse. If one neglects the effects of gravity and aerodynamic drag, one would arrive at equation relating the fuel mass fraction to specific impulse, otherwise known as the rocket equation **[1]**:

$$\frac{M_{fuel}}{M_{total}} = 1 - \exp\left(-\frac{\Delta V}{g_0 I_{sp}}\right) \qquad \textit{Eq. 1.1}$$

The fuel mass ratio, M_{fuel} / M_{total}, defines the ratio of fuel mass to the entire spacecraft, which includes fuel, structure, and payload. For most space missions, the weight of the fuel constitutes the highest percentage of the total weight of the spacecraft. As shown in Eq. 1.1, this ratio is exponentially dependent on the specific impulse of the rocket. To assess the improvement in fuel mass ratio with different thrusters, consider a liquid oxygen, liquid hydrogen thruster, which has a specific impulse of about 450 seconds. To perform a LEO to GEO maneuver, the total mission ΔV is about 3.8 km/s. With these values, the fuel mass ratio is 0.58 or approximately 58% of the spacecraft would have to be fuel weight. Now consider a zeon ion thruster, where the specific impulse is around 2,500 seconds. The fuel mass ratio with this thruster is now 0.15 or approximately 15% of the spacecraft would have to be fuel weight. This suggests that one could use a smaller, cheaper launch rocket in the first stage or use the same launch rocket and have a larger satellite with more capabilities. The only caveat to using advanced propulsion systems with a high specific impulse is that they have a low thrust output, and hence their missions are much longer in comparison to liquid chemical rockets.

In addition to cost benefits, a high specific impulse propulsion system also creates opportunities for deep space missions. While instantaneous thrust output of these systems is fairly low, the total time-integrated thrust output of these rockets can be greater than chemical rockets if the mission time length are long enough. With NASA's recent announcement of newfound commitments to go back to the moon, Mars, and beyond, interests have been gathering in the field of advanced propulsion. Several concepts, including nuclear thermal rockets, solar thermal sails, and electrical thrusters, are being developed for satellite and deep space missions. Of the many types of non-chemical thrusters, electrical thrusters are one of the few which are currently in use today. Their relatively simple design and high specific impulse makes them excellent candidates for satellite maneuver, orbital station-keeping, and deep space exploration. Their only limitation is their electrical power generation unit, which constrains their total thrust output. Modern electrical thrusters offer thrust outputs in the range of milli-Newtons to one Newton.

Electrical propulsion systems are different from chemical rockets in that they use electromagnetic forces, as opposed to gas combustion, to accelerate or heat a gas. The type of electrical thruster of interest for this project is gas-fed pulsed plasma thrusters (GFPPTs), which belong to a family of magnetoplasmadynamic thrusters. They produce thrust outputs in the ranges of milli-newtons with a specific impulse of around 750 to 1000 seconds. Although their fuel efficiency is fairly low compared to other electrical rockets, their advantage is their low voltage input. Unlike other electrical thrusters which require several kilovolts input, pulsed plasma thrusters require only several hundred volts for operation. Combined with their simple design configuration, pulsed plasma thrusters are used ideal for orbit station-keeping after a satellite has reached its final orbit and electrical power is provided by solar arrays.

The main components of a pulsed plasma thruster are its capacitor, electrodes, fuel, and plasma initiation source. Figure 1 provides a schematic overview of a co-axial gas-fed, pulsed plasma thruster, adopted from Science Research Laboratory Model PT4 **[2]**. The PT4 thruster is a convenient model to serve as an example to facilitate discussions concerning characteristics and performance of GFPPTs. For future discussions relating to co-axial GFPPTs in this report, model PT4 would serve as the primary example, unless otherwise stated.

During the first stage of PT4 operation, neutral gas, such as argon, is injected through the back-plate and into the co-axial chamber. In the second stage, the objective is to create plasma to increase electrical conductivity in the electrode gap; this will allow current from a capacitor bank to flow across the gap and form a current sheet. In order to generate plasma, one technique is to apply a voltage potential across this gap to increase the collision rate between electrons and neutral gas particles. If the voltage is high enough, the gas will break down. However, the gas can also break down if the voltage is slightly below the minimum breakdown voltage if there is an external source of electrons. This is known as under-voltage breakdown and it occurs when the source of electrons are used to increase the collision and ionization rate. A detailed description of

undervoltage breakdown will be presented later in this paper. For PT4, which operates in an under-voltage condition, this external source of electrons is sparkplugs. The main advantage with under-voltage breakdown is that it allows PT4 to control the pulsing period by controlling the injection of electrons.

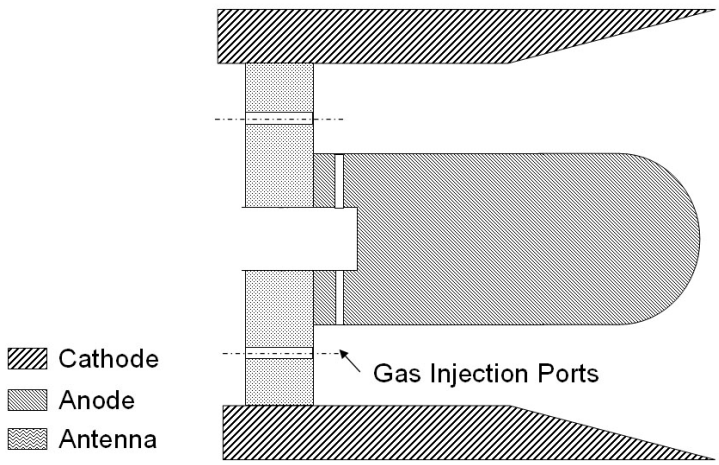

Figure 1.1: Schematic diagram of the Science Research PT4 thruster. Behind the anode back plate is the gas chamber.

While the injection of electrons increases the ionization rates, it also increases the local electrical potential, which facilitates further gas breakdown. Once plasma is formed in the electrode gap, the PT4 capacitor bank discharges spontaneously to initiate a current flow across the gap. As current flows across the plasma, a current sheet forms. Furthermore, with current flow in the radial direction, an induced magnetic field is formed in the azimuthal direction. This creates a **j x B** Lorentz body force, which accelerates the current sheet downstream of the thruster chamber. As the current sheet travels downstream, it ionizes and accelerates the neutral propellant gas particles, and thus, producing a reactive thrust force on the thruster.

An important performance parameter in GFPPTs is the uniformity of the current sheet. If the current sheet is non-uniform, gas leakage will occur, and particles are leaked out of plasma chamber without being accelerated. Since the uniformity of a current sheet is dependent on the uniformity of plasma plume, it is important that gas breakdown occurs uniformly in PT4. It has been well documented that spark-initiated GFPPTs experience a performance drop with spark initiation due to non-uniform current sheets [**2, 3, 4**]. As one will encounter in the next couple sections, much research in the field of PPTs have been devoted to improving current sheet uniformity through alternative means of electron initiation.

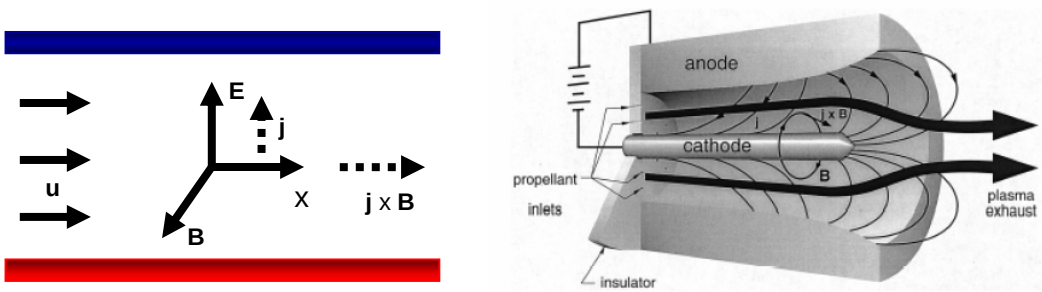

(a) **(b)**

Figure 1.2: Principle theory of electromagnetic thrusters. *(a)* Flow field interactions within an electromagnetic gap. *(b)* Schematic diagram of flow fields in an MPD thruster.

Microwave initiation is a mechanism which is well-documented and has been a robust method of plasma initiation **[6]**, **[7]**. The main objective of this project is to analyze the feasibility of using microwave plasma as one approach of improving current sheet uniformity. In order to understand how microwave plasma will improve the performance of GFPPTs, this remainder of this chapter will present a comprehensive overview of issues related to spark-initiated GFPPTs and what current research is studying to mitigate this problem. These

sections will be followed by a discussion about microwave discharge and how to apply microwave discharges to GFPPTs to improve current sheet uniformity.

1.1 Limitations of Spark Initiated GFPPTs

The source of plasma initiation on the PT4 is four sparkplugs, which are configured equidistantly on the outer anode cylinder. These sparkplugs are commercial products similar to those found in an automotive ignition system. They have a voltage input requirement of around 150 volts; their total energy consumption is around 2.5 J per spark plug. During PT4's operation, they provide a source of electrons which temporally increases the voltage potential in the co-axial electrode gap. This initiates the gas breakdown in the electrode gap.

While spark plugs are reliable source of electrons, one of their greatest limitation is their inability to inject electrons uniformly in PT4. As shown in Fig. 1.3, when a spark plug generates a spark, the plasma that is form is concentrated around the spark electrodes. Henceforth, gas breakdown occurs at a much faster rate in regions around the spark plugs, and the resulting plasma plume becomes non-uniform. This is further exacerbated with different firing delays associated with each spark plug. When one spark plug fires before the rest, breakdown will occur initially around the fired sparkplug and creates a dense plasma region around that spark plug.

In addition to non-uniform current sheets and sparkplug misfires, it has also been well documented that spark plugs suffer severe corrosion rates which often fail pre-maturely in a thruster's lifetime **[8]**. If one considers a spark plug as two electrodes with high electrical conductivity, during each sparkplug firing, there is a large electrical potential between the anode and cathode. Electrochemical chemical reactions and also occur, in which anodic ions from the anode travel across to the cathode, creating corrosion in the anode. The rates at which PT4 electrode corrosion occur has been characterized **[8]**. If one considers a thruster lifetime of ten years, one can determine that the sparkplugs would fail

much sooner than the thruster. Hence, due to difficulties with creating a uniform current sheets with spark plugs and their limited life spans, it will be extremely difficult to improve the performance characteristics of PT4 without replacing spark plugs with an alternative electron source.

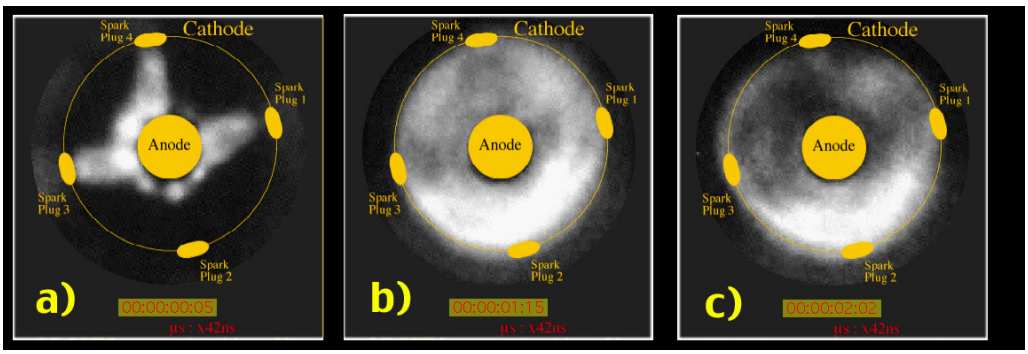

Figure 1.3: Photograph of PT4 current sheet progression when looking head-on from the back of PT4 GFPPT. The lighter regions correspond to a higher plasma and current sheet density. (a) Spark plugs initially fire to induce undervoltage breakdown. As one can notice, spark plug 2 does not appear to be firing at the same time as the other three spark plugs. (b) Breakdown occurs around spark plug 1, 3, and 4 and current sheet initializes around these three spark plugs. When spark plug 2 fires, the current sheet "shifts" to the region around spark plug 2. (c) The distorted current sheet is accelerated toward the viewer by the (j x B) Lorentz Force.

1.2 Current Research on Alternative Plasma Initiation Source

Past and current research on gas-fed pulsed plasma thrusters have attempted to use laser initiation as one alternative to spark initiation **[9]**. This work is conducted at Princeton University Electric Propulsion and Plasma Dynamics Laboratory, and it utilizes a PT4 thruster as a test sample. With laser initiation, a

laser is targeted at the back-plate of anode electrode of the PT4. If the laser energy intensity is higher than a critical intensity, this will excite electron photoemission, which releases electrons into the co-axial electrode gap. Under proper undervoltage breakdown conditions, this will initiate gas breakdown in PT4. The goal of laser initiation is to target an annular laser ring into the black-plate of the anode and initiate azimuthally symmetric breakdown, which will lead to a uniform current sheet. Experimental results have demonstrated that a uniform and annular ND:Yag laser with a energy output of 600 mJ can initiate gas breakdown in PT4 **[9]**.

While laser initiation has been proven to be a viable alternative to spark-initiation, more research would need to be invested in this technology. Particularly, there is insufficient data to indicate that the electron excitation mechanism is actually photoemission. In fact, experimental data has shown that it can not be photoemission, but instead, either thermoionic emission or material desorption on the surface of the anode **[9]**. The theory of material desorption is favored over thermoionic emission, essentially because one could actually witness a hole or ring patter on the anode when it's removed from the anode. Thus, when the laser impacts the surface of the anode, it collides and excites, sometimes even vaporizing, the molecular compounds on the surface. The vaporized or ablated material could raise the voltage potential of the electrode gap, and thus initiating gas breakdown.

One of the main disadvantages with laser initiation is the rate of material desorption on the surface of anode. Over a long period of time, the back plate could be heavily damaged from material desorption, and could possibly lead to thruster failure. This is similar to the problem experienced earlier by spark plug corrosion, but yet smaller by a couple orders of magnitude (thickness and size of anode back-plate is much larger than spark plug electrode). In order to find a robust alternative to spark plugs, a different approach would need to be taken besides laser initiation.

1.3 Microwave Discharge Initiation: Past Research and Application

The concept of microwave breakdown is a subject that is fairly comprehensive and well-studied. Microwave plasma is currently used in the metal industry, where microwave plasma arcjet is used to cut metal with high precision. In space applications, microwave plasma are used in single- and double-stage microwave electrothermal thrusters (MET) **[7, 10]**. These thrusters are similar to an arcjet thruster, but uses a plasma arc sustained by microwave energy to heat and expand propellant gas.

The physics behind microwave plasma goes in line with the discussion on gas breakdown in Appendix A. Essentially, microwave energy is used excited a specific electromagnetic field pattern in a microwave resonant cavity or waveguide. Depending on the specific field pattern, there are localized regions of high intensity electric fields oscillating with time. These fields cause translational and rotational electron excitation, and if the frequency of atomic ionization in these localized regions is greater than the frequency of recombination per oscillation, then this will lead to an electron avalanche effect, where electrons are produced exponentially with each oscillation. Gas breakdown would then occur in localized regions with the highest electric field intensity.

Theoretically, microwave initiation can be used in GFPPTs to enhance current sheet geometry. By selecting a proper electromagnetic mode which has an azimuthally symmetric electric field distribution, one could initiate gas breakdown uniformly in the co-axial thruster chamber with minimal modifications to the GFPPT design. The physical theory behind this approach is highly conceivable, and it would be fairly easy to implement. Fig. 1.4 is a theoretical electrode design of a microwave-initiated GFPPT. Essentially, a co-axial GFPPT such as the PT4 would have an electrode gap that has a constant electric potential. A microwave source such as a magnetron would be introduced to the electrode gap. One could select a frequency or redesign the electrode gap such that it sustains the resonant electromagnetic mode that is desired. After gas is injected in to the co-axial chamber, the magnetron will be activated and excites a

resonant mode in the co-axial chamber. Breakdown would then occur in regions with high electric field intensities. For GFPPT application, these regions of high electric fields would need to azimuthally symmetric and located closed to the backplate of the thruster.

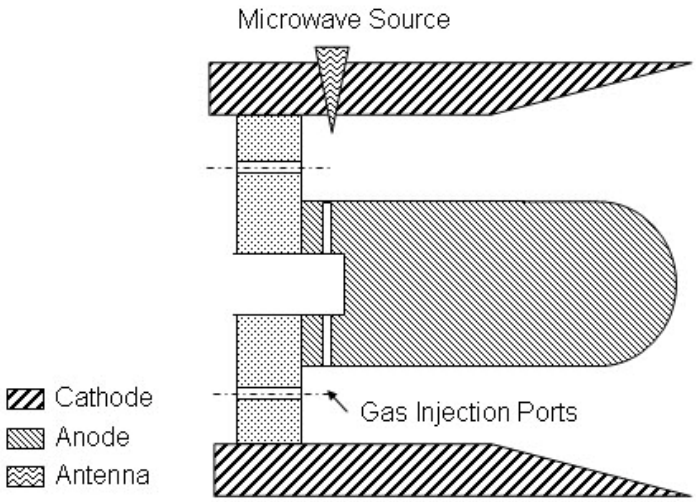

Figure 1.4: Theoretical design of co-axial GFPPT which utilizes microwave initiation.

With microwave initiation, there are two significant advantages over spark and laser initiation. The first advantage is that there a microwave energy source does not encounter the corrosion issues with spark plugs, nor does it cause electrode surface ablation. One can conceivably obtain a 2.45GHz magnetron from a conventional microwave oven and use it as a microwave source. These magnetrons are low cost to manufacture and extremely robust if used properly. One problem that magnetrons might encounter might be overheating, but this can be mitigated by actively cooling the magnetron during operation.

A second advantage of microwave initiation is that it offers unparallel energy efficiency. Compared to spark plugs and lasers, magnetrons are just as, if not more energy efficient, than spark plugs and more efficiency than lasers by a factor of nine. Table 1.1 lists compares the energy usage of a commercial 800W magnetron with four PT4 spark plugs and a 600 mJ infrared ND:Yag laser.

Table 1.1: Energy Consumption and Conversion Efficiency of four spark plugs, a 800 W magnetron, and a 600 mJ ND:Yag laser.

	Four Spark Plugs	**800W Magnetron**	**600 mJ Solid-State Laser**
Energy Conversion Efficiency.	95%	85%	2.0 – 25%
Energy Consumption (mJ)	11	8.0	2000 - 25,000

From Table 1.1, one can see that a magnetron surpasses a laser in terms of energy consumption and efficiency. This is especially important, since power constraints in space will severely limit the use of a laser. However, a microwave initiated GFPPT will be within these power constraints and would be appropriate to use. For these two reasons, microwave initiation for GFPPT would be more practical and offer better performance than both spark plugs and lasers.

1.4 Thesis Objectives

Improving the performance and lifespan of GFPPTs will be valuable for future space applications, where solar power availability is low. For example, pulsed plasma thrusters are ideal thrusters for satellites attempting station-keeping

maneuvers in distant orbits, where there are severe power constraints. As discussed previously, one approach to enhance the lifespan and performance of GFPPTs is to replace spark initiation with microwave initiation. With this mind, the primary goal of this project is to investigate using microwave discharges to initiate propellant gas breakdown in GFPPTs. Segments of this project will include designing a microwave-initiated pulsed plasma thruster and performing all detailed simulations, prototyping, and experimentation with the following objectives in mind:

1. Understand the physical mechanism of microwave discharges.
2. Design and manufacture a MiPPT prototype.
3. Develop analytical and computational models to stimulate the performance
4. characteristics of MiPPT.
5. Demonstrate current sheet uniformity during steady-state and pulsed operation.
6. Show improved thruster performance with microwave initiation.

The work presented in this proposal will be conducted at Princeton University's Electric Propulsion and Plasma Dynamics Laboratory (EPPDyL) under the guidance and mentorship of Prof. Edgar Y. Choueiri.

Chapter 2: Design of Microwave-Initiated Pulsed Plasma Thruster (MiPPT)

Gas-Fed, pulsed plasma thrusters have many different design configurations. Each of these configurations provides advantages for various applications. In selecting an optimal configuration for a microwave-initiated GFPPT, two main factors are considered. The first factor is whether the configuration has any basis from previous GFPPT design configurations. This is crucial because it allows one to compare the performance characteristics of a microwave GFPPT with other various GFPPTs. The second factor is manufacturing and cost. The microwave GFPPT is constrained to a budget and timeline, and hence, any configurations should be cost-effective and machineable. Given these two factors, the configuration that is selected for a MiPPT is a co-axial configuration with an inner cathode and other anode. This configuration reflects a family of GFPPTs that are currently being researched, such as the SLR PT4 and PT5 **[2]**.

With a co-axial configuration, a MiPPT would need to couple microwave energy into a co-axial plasma chamber. One technique of accomplishing this is to

directly inject microwave energy into the co-axial chamber by installing a magnetron. While this is feasible, one problem is that the co-axial chamber opens to the atmosphere, and microwave energy will be leaking out of the thruster. Not only is this method inefficient and extremely difficult to collect enough energy for breakdown, it also poses as a health concern to people exposed to microwave energy. An alternative technique is to design a pre-ionization chamber, where microwave energy is contained in a chamber to initiate gas breakdown, and couple it to the co-axial plasma chamber.

In this chapter, the details of designing a pre-ionization chamber and how to couple this chamber to MiPPT are discussed. First, the fundamental equations for the electromagnetic field distribution inside a wave-guide and resonant cavity are presented. Using these equations, the pre-ionization chamber will be sized to support a resonant mode. A preliminary stimulation will be presented to demonstrate that the pre-ionization chamber supports that resonant mode. Second, a description of how a MiPPT operates will be presented, with emphasis on gas injection and plasma discharge initiation.

2.1 Selecting a Resonant Cavity Mode

The pre-ionization chamber is coupled to the co-axial plasma chamber. Given the circular geometry, the most pragmatic geometry of the pre-ionization chamber is a cylindrical cavity. The sizing of the cylindrical cavity determines the resonant field distributions that can exist inside cavity. Selecting a proper resonant mode will determine where the highest electrical field intensities exist, and hence, where the highest plasma densities are greatest when breakdown occurs. In a hollow cylindrical resonant cavity, there are two specific types of resonant modes that exist: transmagnetic (TM) modes and transelectric (TE) modes. Each of these modes define whether the axial fields are magnetic or electrical fields. Ideally, a MiPPT would want the highest electric field intensities in the azimuthal direction, since this will create an azimuthally symmetric plasma distribution. Hence, for this application, the TE resonant modes would be preferred over the TM resonant

modes (TE resonant modes has magnetic field in the axial and azimuthal direction and electrical field only in the azimuthal direction).

In finding the electromagnetic field distributions inside a resonant cavity, one would need to solve Maxwell's Equations. Since the derivations of the solutions of Maxwell's Equations for a cylindrical resonant cavity is often quite tedious, the reader is referred to reference **[10]** for a complete derivation of these solutions. It can be shown that the resonant frequency that can exist in a TE or TM resonant mode cavity is given below:

$$\omega_{mnp} = \frac{c}{\sqrt{\mu\varepsilon}}\sqrt{\frac{4x_{mn}^2}{D^2} + \frac{p^2\pi^2}{l^2}} \qquad \textit{Eq. 2.1}$$

In the above expression, the *p* index refers to the number of integer half-wavelengths that can exist inside a resonant cavity. It important to note that X_{mn} for TM type modes refers to m^{th} zero of the nth order Bessel function of the first kind. For TE type modes, X_{mn} refers to the mth zero of the nth order of the Bessel function of the second kind. Appendix A.2 provides several zeros of Bessel functions of the first kind.

Given the mode and the p index of a resonant cavity, only the diameter, D, and length, l, of the cavity determines the resonant frequency inside the cavity. Since most commercial magnetrons operate at 2.45 GHz, the design resonant frequency of the pre-ionization chamber should be 2.45 GHz. From the above equation, one will notice that there are many combinations of diameters and lengths which will give a resonant frequency of 2.45 GHz for a specific resonant mode. Using the above equation, one can graph the mode chart similar to the one presented in Fig. 2.1 in selecting a proper mode and dimensions for the resonant cavity.

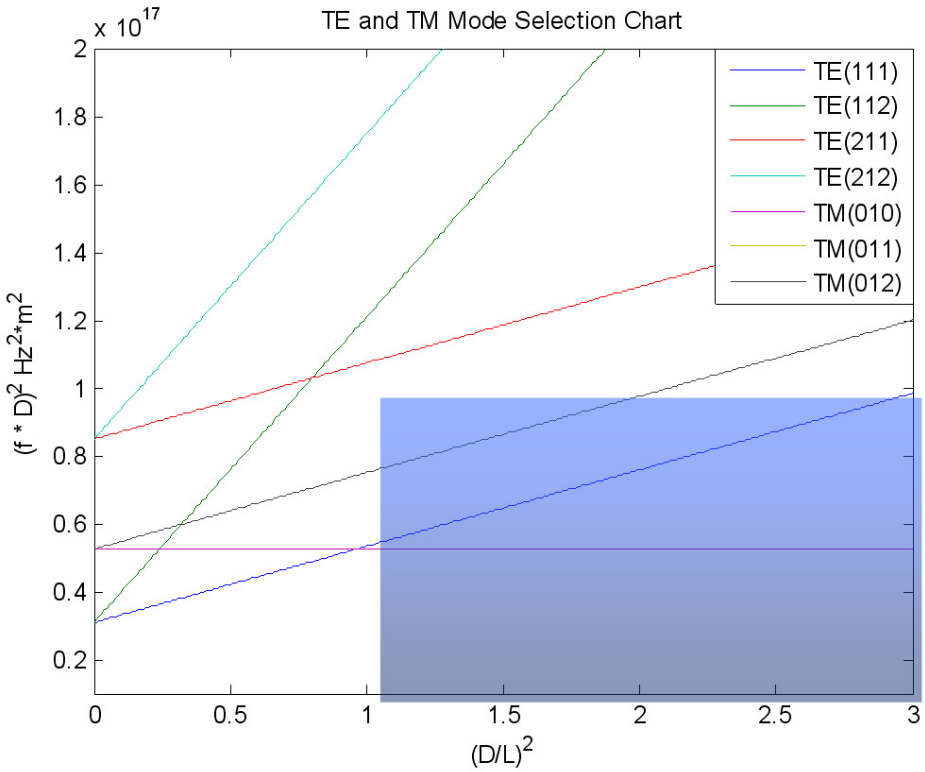

Figure 2.1: Mode Selection Chart for Cylindrical Resonant Cavity. The highlighted region represents the modes feasible in a 12.7cm diameter x 12.7cm length cavity with a resonant frequency of 2.45 GHz.

Fig. 2.1 only provides several TM and TE resonant modes from the many possible modes. However, they are the modes with the lowest (f * D) factor; in sizing the resonant cavity, one of the main goals is to make the cavity as compact as possible. Not only will this conserve weight for space applications, it will also confine microwave energy into a smaller cavity, hence increasing the energy density to initiate gas discharge. From Fig. 2.1, the highlighted region represents the various modes that could be supported in a conceivable cylindrical cavity that

has a maximum of 12.7 cm diameter and 12.7 cm length. As one can perceive, there are only three modes which could be supported in a cylindrical cavity of this size: TM_{010}, TE_{111}, and TE_{112}. Since TE_{111} and TE_{112} would produce fairly high-intensity, azimuthally symmetric electric fields, these two modes are preferred over TM_{010}. The smallest volume cavity that could be obtained with either one of these two modes is a 12.7 cm diameter x 7.366 cm length cylinder. While this could be conceivable for the purposes of this project, it is still fairly large compared to the dimensions of other pulsed plasma thrusters (i.e., PT4 co-axial electrodes are no large than 7.62 cm diameter x 6.35 cm length). An alternative to a TE_{111} and TE_{112} resonant cavity is a TM_{010} cavity. From Fig. 2.1, one will notice that the tuning of a TM_{010} cavity is independent of length. For a TM_{010} cavity, the resonant diameter is 9.53 cm and the length can be any length that is desired. For all practical purposes, a length of 1.91 cm is selected for a TM_{010} resonant cavity.

With a TM_{010} resonant cavity, one main concern is that the highest electrical field strength occurs along the axial direction, and thus the highest plasma density will be found along the axial direction. Nevertheless, one can design a plasma injection system which would take the plasma along the axial axis and inject them in the azimuthal direction. This will be discussed in a later section of this chapter.

2.2 Electromagnetic Field Distribution in a Cylindrical Resonant Cavity

The TM resonant mode has only an azimuthal magnetic field distribution and an axial and radial electric field distribution. In order to visualize the amplitudes of these field distributions inside the resonant cavity, one would need to solve Maxwell's equations again and apply the proper boundary conditions to obtain the electromagnetic field lines in a cylindrical cavity. Assuming negligible effects from the presence of plasma, dielectrics, and imperfect geometry, the complex field components for TM resonant cavities can be expressed in cylindrical coordinates as a function of the complex magnetic vector potential, psi, in the following set of equations **[10]**:

$$
\begin{aligned}
\boldsymbol{E}_r &= -i\frac{1}{\omega\mu\varepsilon}\frac{\partial^2\psi}{\partial r\partial z},\\
\boldsymbol{E}_\theta &= -i\frac{1}{\omega\mu\varepsilon r}\frac{\partial^2\psi}{\partial\theta\partial z},\\
\boldsymbol{E}_z &= -i\frac{1}{\omega\mu\varepsilon}\left(\frac{\partial^2}{\partial z^2}+\varepsilon\mu\omega^2\right)\psi,\\
\boldsymbol{H}_r &= \frac{1}{\mu r}\frac{\partial\psi}{\partial\theta},\\
\boldsymbol{H}_\theta &= -\frac{1}{\mu}\frac{\partial\psi}{\partial r},\\
\boldsymbol{H}_z &= 0.
\end{aligned}
\qquad \textit{Eq. 2.2}
$$

To solve for psi, the Helmholtz wave equation is used to describe the spatial distribution of psi in cylindrical coordinates **[10]**:

$$
\frac{\partial^2\psi}{\partial r^2}+\frac{1}{r}\frac{\partial\psi}{\partial r}+\frac{1}{r^2}\frac{\partial^2\psi}{\partial\theta^2}+\frac{\partial^2\psi}{\partial z^2}+\varepsilon\mu\omega^2\psi=0 \qquad \textit{Eq. 2.3}
$$

Assuming perfectly conducting walls, the solution of the Helmholtz wave equation for psi in a cylindrical cavity can be given below **[10]**:

$$
\psi(r,\theta,z)=J_m\left(\frac{X_{mn}p}{R}\right)\cos(m\theta)\cos\left(\frac{p\pi z}{l}\right) \qquad \textit{Eq. 2.4}
$$

For a TM_{010} mode, the above solution for psi can be simplified to the expression given below:

$$\psi(r,\theta,z) = J_0\left(\frac{X_{01}r}{R}\right)\cos(0)\cos(0) = J_0\left(\frac{X_{01}r}{R}\right) \qquad \textit{Eq. 2.5}$$

With an expression for psi, one could then substitute Eq. 2.5 into Eq. 2.2 to solve for each component of the electromagnetic fields. To simplify the expressions, each component is normalized with a –iω term, which is the coefficient for E_z. The final normalized electric and magnetic field components are given below:

$$\begin{aligned} E_z &= J_0\left(\frac{X_{01}r}{R}\right) \\ H_\theta &= i\left(\frac{X_{01}}{\mu\omega R}\right)J_1\left(\frac{X_{01}r}{R}\right) \end{aligned} \qquad \textit{Eq. 2.6}$$

As one will notice, all components of the electromagnetic fields are zero, except the axial electric field and the azimuthal magnetic field. Furthermore, the axial electric field is a function of the distance from the center of the z-axis, coupled into a zero order Bessel function of the first kind. As anticipated, the highest electric field intensity occur along the center axis of the cavity. On the other hand, the azimuthal magnetic field is also a function of the distance from the center of the axis, but it is coupled into a first order Bessel function of the first kind. Thus, one can anticipate the highest magnetic field potentials to be greatest at half the radial length from the center axis of the cylinder.

To visualize the axial electric and azimuthal magnetic fields, contour plots of these two fields are generated using the commercial software Matlab. For the axial electric fields, the non-dimensional, time-averaged values, EzEz*/2, is plotted on a contour plot with the y-axis representing the radius and the x-axis representing the length. The results are shown in Fig. 2.2. From the figure, it is evident that the maximum electric field strength occur along the center axis of the cylinder, which is anticipated from previous discussions. Similarly, for the azimthual magnetic field distributions, the non-dimensionl, time-average values, $H\theta H\theta$*/2, is plotted on a contour plot with the y-axis representing the radius and

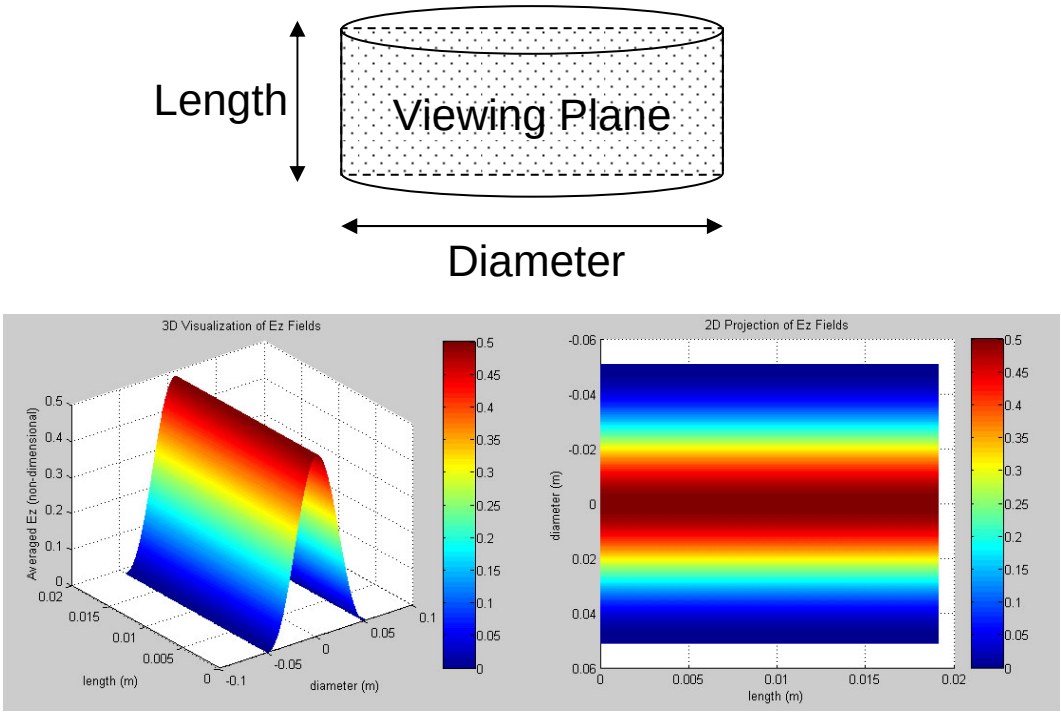

(a) (b)

Figure 2.2: Time-averaged axial field distribution of the viewing plane. Since there is axial symmetry in the cylindrical resonant cavity, field distribution is same for all viewing planes which lie in the same plane as the axial axis. (a) 3-Dimensional visualization of the normalized axial electric field amplitudes. (b) 2-Dimensional contour projection of the 3-D visualization display.

the x-axis representing the length of the cavity. This can be seen in Fig. 2.3. As predicted, the maximum field strengths occur at a distance of 4.0 cm from the center axis. While magnetic fields do not contribute a large effect to the initial gas breakdown, they might effect the transport phenomenon of the plasma as induced magnetic fields are produced in the presence of a current. This will be discussed in later chapters of this report.

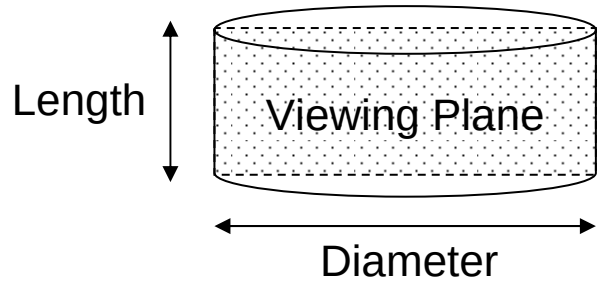

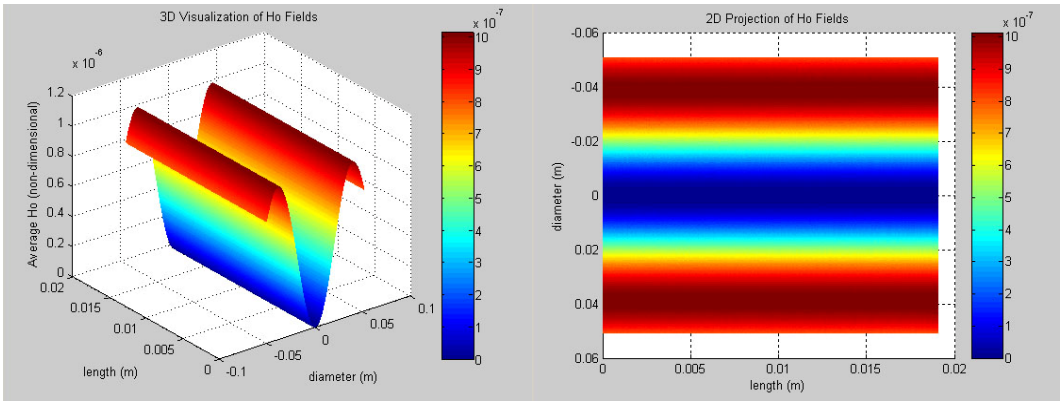

(a) (b)

Figure 2.3: Time-averaged azimuthal magnetic field distribution in the viewing plane. Due to the axial symmetry of the resonant cavity, field distribution is same for all viewing planes which lie in the same plane as the axial axis. (a) 3-Dimensional visualization of the normalized azimuthal magnetic field amplitudes. (b) 2-Dimensional contour projection of the 3-D visualization display.

2.3 Design of the Pre-Ionization Chamber

With the sizing of the pre-ionization chamber already determined, next stage of development is modifying the chamber for the MiPPT. One unique characteristic of this pre-ionization chamber is that it will also serve as a gas

distribution chamber to the co-axial electrode chamber. The initial prototype of the MiPPT has two gas feed lines which are attached to the pre-ionization chamber at an angle directed towards the center axis. Initially, gas is injected to the pre-ionization chamber through these two gas feed lines; they then diffuse across the chamber.

Several design considerations include coupling the 2.45 GHz magnetron to the cavity to excite a specific resonant mode, sizing of holes for gas injection, and distributing plasma to the co-axial chamber in an azimuthally symmetric fashion.

2.4 TM_{010} Mode Excitation with 2.45 GHz Magnetron

In order to excite a specific resonant mode in cavity, the method of introducing microwave energy into the cavity must be carefully selected. The microwave source is a commercial 2.45 GHz magnetron from a conventional oven (LG Model 246). The rated maximum power output is approximately 700 watts. A simplified diagram of the magnetron can be seen in Figure 2.4(a).

The microwave energy is dissipated from an one inch antenna probe at the top of the magnetron. The inside of the antenna probe antenna is a transmission line coupled to resonant cavities inside the magnetron. These resonant cavities surround a cathode filament which provides a steady stream of electrons when powered by a high current voltage input. The potential difference between the cathode filament and anode walls established an electric field in the radial direction while the permanent magnets induced a field in the azimuthal direction. The combined effect from both these fields moves the electrons in a spiral direction from the cathode toward the walls of the resonant cavities. The flow of electrons induces microwave field which is coupled to the probe antenna though an inductive loop antenna. Most commercial magnetron units have voltage potentials of three to four kilovolts between the anode and cathode, while the filament itself takes a five to ten amps at twenty to thirty volts to heat up and radiate electrons. The inductive loop antenna on one end of the transmission line

absorbs microwave power from these resonant cavities and transmits them to the end of the probe. The probe then excites electric fields in the axial direction and magnetic fields in the azimuthal direction. In order to couple the magnetron to the pre-ionization chamber and excite a TM_{010} mode, one would need to place the stub antenna parallel to the electrical fields of the resonant mode; with this configuration, the electric field from the magnetron antenna would excite the axial electric field from the TM_{010} cavity.

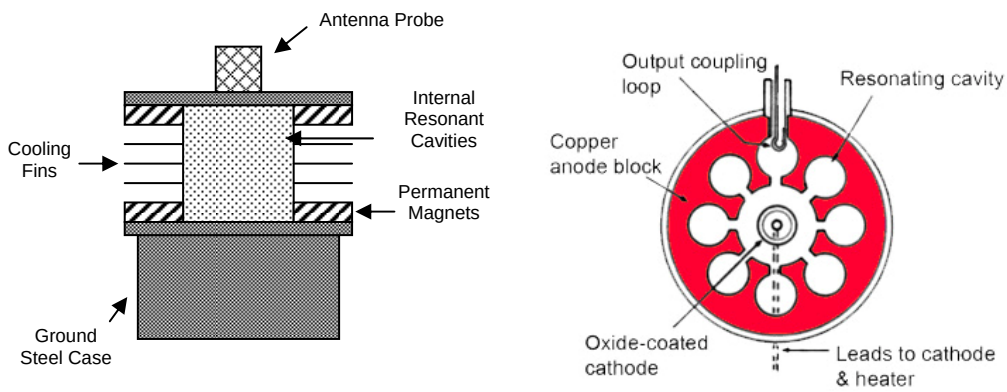

(a) (b)

Figure 2.4: (a) A schematic diagram of a commercial 2.45 GHz conventional oven magnetron from the exterior. (b) Cross-section of the internal resonant cavities with the cathode filament and inductive loop antenna coupled to these cavities. The center cathode filament provides the electrode source; electron spiral towards the resonating cavities, ultimately creating a current flow, which generates electromagnetic field resonating at 2.45 GHz **[14]**.

Although direct coupling of the magnetron to the resonant chamber is the simplest method of exciting the resonant mode in cavity, it does have one disadvantage. With this approach, there is really no technique to sample the amount of reflected power from the resonant cavity. This is an important parameter when one needs to measure the amount of power absorbed by neutral

gas and plasma. Alternatively, one could couple the magnetron to a waveguide use a triple-stub tuner to match the impedance of the waveguide and magnetron. This way, all the power from the microwave antenna does not reflect back to the magnetron. An antenna can be used to extract power from this waveguide, but it needs to be tuned to match the impedance of the waveguide for maximum power transfer. (i.e., an inductive loop antenna or a co-axial probe). Nevertheless, the setbacks of this approach are hefty waveguides, precise tuning devices, and an antenna that needs to be designed with accuracy. Comparing these two approaches, the first is more suitable for this project. For one, the goal of this project is not maximize the microwave power input into a cavity to create and sustain a high power arc discharge like those in the experimental microwave arcject thrusters **[7]**. Rather the concept is to pre-ionize the gas that is to be used to induce under-voltage breakdown. Hence, even if the capacitative coupling with the stub antenna is less than 100% efficient, that will suffice for this project as long as there is enough power to initiate breakdown. Nevertheless, without a power measurement of the reflected power, the cavity dielectric filling and magnetron can potentially overheat during operation. To protect the magnetron and resonant cavity from overheating heating, chilled water will need to cool both the magnetron and the pre-ionization chamber.

Even though tuning of the magnetron and antenna is not available with direct coupling, there is still the option of tuning the cavity by sizing of the cavity, introducing of dielectrics, applying metallic screw knobs, and varying length of probe antenna. In a previous study utilizing a similar microwave cavity with the same TM010 resonant mode, proper tuning has of the microwave cavity using the above techniques has allowed nearly zero reflected power from the cavity **[15]**. In that study, it has been found that the introduction of a probe antenna and fused-silica gas tube actually de-tunes the cavity by approximately 150 MHz, to compensate for these variables, the cavity is designed to be slightly smaller in diameter (88.6 mm in diameter as opposed to 93.2 mm in original design) **[16]**. Furthermore, they've applied a variable length probe antenna and quartz tuning rod to compensate for any further losses.

The techniques described in van Dalen **[16]** are applicable only if one has a bi-directional microwave coupler to measure the input and reflected power of the cavity. Since such a piece of equipment is not available for use in this project (beyond the budget of this project), it is rather difficult to see the effects of a variable length antenna or dielectric on the tuning of the microwave cavity. Nevertheless, one could still obtain a rather crude estimate on the effects of these variables by performing a simple experiment to heat up water using the microwave cavity. Since the cavity itself is nothing more than condensed version of a microwave oven, one can conceivably compare power inputted to the cavity by measuring the power absorbed by water in the cavity. It is essential to understand that this is only for comparative purposes and doesn't really measure the power transferred to the cavity from the magnetron (total power transferred to the cavity will require measuring power absorbed by the cavity, internal dielectric, and radiative losses, which are all tedious tasks). Using this concept, an experiment is developed to measure the power absorbed by water by varying the diameter of the cavity and length of the antenna. The results can be shown in Table 2.1.

Table 2.1: Power Absorbed by Water Using Various Cavity and Antenna Configurations

Power (Watts)	**Antenna Protrusion**		
Cavity Diameter	*Full Length (25.4 mm)*	*Half Length*	*Quarter Length*
89 mm	155 ± 20	25 ± 5	5 ± 3
95 mm	160 ± 20	30 ± 3	5 ± 4

As one can discern from Table 2.1, varying the diameter of the cavity has rather minimal effects on the tuning of the cavity. However, a more important factor is the length of the stub antenna. It appears that the power absorbed by water is directly related to the length of the antenna; while having a longer antenna de-tunes the cavity, the benefits of a longer antenna is a greater surface area to transmit microwave energy. Hence, it's important to design the cavity with maximum antenna length. Another note to consider is that while the total power

absorbed by water with full antenna protrusion is around 155 Watts, the actual power inputted to the cavity is actually greater than that. The inside of the cavity is filled with teflon, which is an excellent insulator. Even with teflon filling, the aluminum material used to make manufacture the cavity actually heats up approximately 5 to 10 degrees. At a minimum there would be at least 200 – 300 Watts in the cavity when the magnetron is on.

2.5 Gas Distribution and Injection

It is essential to have the neutral gas injected uniformly into the co-axial chamber; otherwise, it would lead to a non-uniform plasma density distribution. The gas feed lines to the MiPPT have a diameter of approximately 0.50 cm; while one could conceivability design a MiPPT with a large number of feed lines to ensure gas uniformity, a simpler and more practical design is to use pre-ionization cavity as a gas distribution chamber. With this design, gas feed line would be connected to the pre-ionization chamber and the chamber itself would be placed behind the co-axial chamber. Holes would be drilled on the face of the pre-ionization chamber in such a fashion that gas from the pre-ionization chamber is injected uniformly throughout the co-axial chamber. In other words, when gas is injected into the pre-ionization chamber, it will first pre-mix in the pre-ionization chamber, and then diffuse across the holes on the face of the chamber into the cathode-anode gap. By designing an azimuthally symmetric hole pattern (i.e., an annular configuration), one could control the gas distribution in the co-axial chamber. A schematic of this design is presented in Fig. 2.5.

While designing the hole pattern is essential to the performance of the MiPPT, sizing of the holes will also be important. There are two design parameters to consider in regards to sizing of the holes. The first parameter is to ensure microwave energy does not propagate across these holes, since the dissipated energy will no longer be available to break down neutral gas. The second parameter is to maximize the exit velocity of the gas. This variable is

crucial to the momentum transfer of the exiting gas to the MiPPT, which would result in additional thrust to the MiPPT.

In order to determine the maximum diameter of the hole before microwaves can propagate across them, one needs a brief background on microwave propagation. If we treat the holes as cylindrical waveguides, one can obtain an empirical relationship for the electric and magnetic field distribution, much similar to the result to the cylindrical cavity presented earlier in this paper. For a TM_{mn}-type mode propagation, these field lines are given below in cylindrical coordinates **[11]**:

$$
\begin{aligned}
E_r &= -\frac{i\beta}{k_c} E_0 J'_n(k_c r)\exp i(-n\theta - \beta z) \\
E_\theta &= -\frac{\beta n}{k_c^2} E_0 \frac{1}{r} J_n(k_c r)\exp i(-n\theta - \beta z) \\
E_z &= E_0 J_n(k_c r)\exp i(-n\theta - \beta z) \\
H_r &= \frac{\omega\varepsilon n}{k_c^2} E_0 \frac{1}{r} J_n(k_c r)\exp i(-n\theta - \beta z) \\
H_\theta &= -\frac{j\omega\varepsilon}{k_c} E_0 J'_n(k_c r)\exp i(-n\theta - \beta z) \\
H_z &= 0
\end{aligned}
\qquad \textit{Eq. 2.7}
$$

To determine the cutoff frequency for a TM_{mn}-type propagation mode in a cylindrical waveguide, we need to apply the boundary conditions for the cylindrical waveguide. Assuming the cylinder is a perfectly conducting wall (i.e., metal compound), then the electric field tangential to the wall is zero, or E_θ and $E_z = 0$.

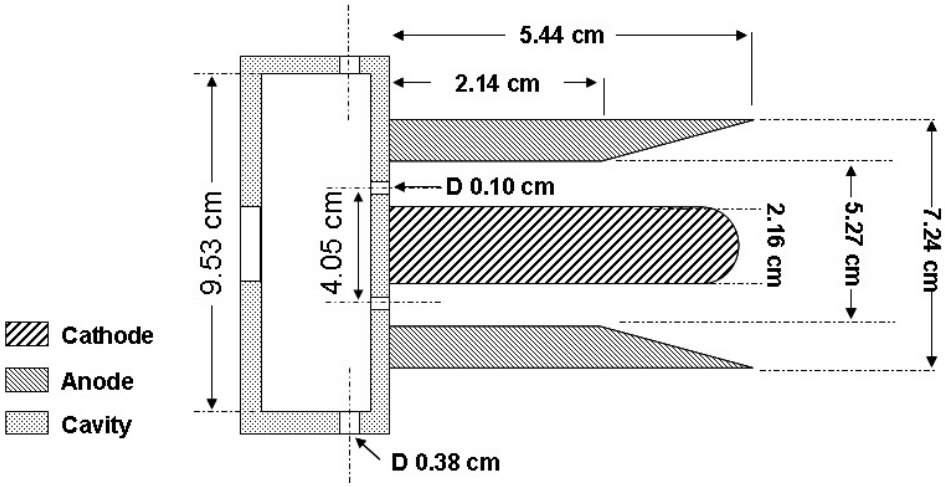

(a)

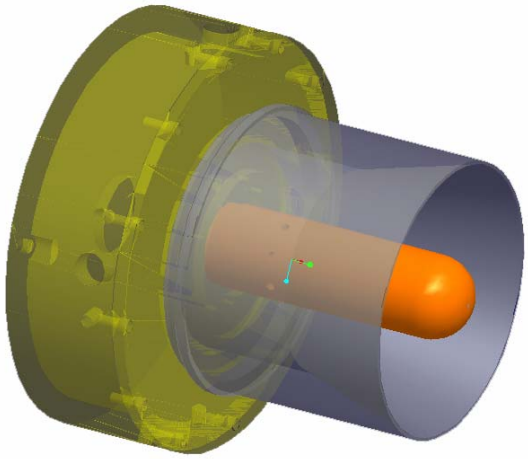

(b)

Figure 2.5: **(a)** Schematic diagram of pre-ionization chamber which also serves as a gas distribution chamber. **(b)** Computer aided design of the pre-ionization chamber with corresponding electrodes.

In order for this condition to be satisfied,

$$J_n(k_c a) = 0,$$
$$or \qquad \textit{Eq. 2.8}$$
$$k_c = \frac{x_{mn}}{a}.$$

In the above equation, X_{mn} correspond the mth zero of the nth order Bessel function of the first kind. The lowest value for variable is x_{01}, which correspond to 2.40. We can relate cutoff wave number, k_c, to the cutoff frequency using the following relationship:

$$f = \frac{k_c}{2\pi_c\sqrt{\mu\varepsilon}} \qquad \textit{Eq. 2.9}$$

Hence, assuming the medium is free space ($\mu = \mu o$, $\varepsilon = \varepsilon o$), we can calculate the cutoff frequency. The minimum diameter size necessary to propagate a TM_{mn} mode microwave is 9.2 cm. Similarly, one can obtain a similar expression for TE_{mn}-type mode propagation. The field distribution can be given below in cylindrical coordinates:

$$E_r = -\frac{\omega\mu n}{k_c^2} H_0 \frac{1}{r} J_n(k_c r)\exp i(-n\theta - \beta z)$$
$$E_\theta = \frac{i\omega\mu}{k_c} H_0 J'_n(k_c r)\exp i(-n\theta - \beta z)$$
$$E_z = 0$$
$$H_r = -\frac{i\beta}{k_c} H_0 J'_n(k_c r)\exp i(-n\theta - \beta z) \qquad \textit{Eq. 2.10}$$
$$H_\theta = -\frac{\beta n}{k_c^2} H_0 \frac{1}{r} J_n(k_c r)\exp i(-n\theta - \beta z)$$
$$H_z = H_0 J_n(k_c r)\exp i(-n\theta - \beta z)$$

Applying the same boundary condition (perfect conducting walls), one would arrive at a cutoff condition very similar to the cutoff condition for TM_{mn}-type modes.

$$J'_n(k_c a) = 0,$$
$$or \qquad \textit{Eq. 2.11}$$
$$k_c = \frac{x'_{mn}}{a}.$$

Here, X'_{mn} corresponds to the mth zero of the nth order differential Bessel Function of the first kind. Every zero corresponds to a specific mode, and the lowest mode is TE_{11} with a X'_{mn} of 1.84. Using Eq. 2.11, we find that the minimal diameter for a TE_{mn}-type propagation mode is 7.0 cm. Hence, the maximum injection hole size would need to be less than 7.0 cm to contain microwave energy in the pre-ionization chamber.

With the size limit imposed from the microwave containment constraint, the next parameter to consider is the velocity and gas flow rates through the injection holes. The holes can be treated as nozzles with a (A_e/A^*) ratio of 1. In order to sustain chocked flow without shocks in the channel, the chamber pressure to exit pressure ratio would need to be at least 1.893. Assuming that ambient pressure ratio is 100 mTorr (in space applications, the ambient pressure is much less), the minimal gas pressure in the chamber will need to be 190 mTorr in order to obtain chocked flow through the channel. The next parameter to optimize is the mass flow rate; the compressible mass flow rate can be given by *Eq. 2.12*.

$$\dot{m} = \frac{AP}{\sqrt{T}}\sqrt{\frac{\gamma}{R}}\left(\frac{\gamma+1}{2}\right)^{-\frac{\gamma+1}{2(\gamma+1)}} \qquad \textit{Eq. 2.12}$$

The maximum mass flow rate through the injection ports is limited by the mass flow rates of the gas feed line. Ideally, one would want to maximize the hole

size, but at the same time, he or she also do not want all the gas to leak out of the pre-ionization chamber. A residue amount is necessary for gas discharge in the chamber. On the PT4 GFPPT thruster, the gas injection hole sizes are approximately 0.23 cm. Initially, this is the hole size designed for MiPPT. Nevertheless, as one will encounter later in this report, this hole size is too large to maintain the minimum pressure for microwave breakdown. In the final MiPPT prototype design, the hole size is 0.10 cm.

2.6 Plasma Injection

Once the injected gas fill the co-axial chamber, the magnetron is pulsed and excites a TM_{010} resonant mode in the resonant cavity. As discussed previously, one of the challenges of the utilizing a TM_{010} resonant cavity mode is that the maximum electric field intensity occurs along the axial axis, which suggests that the highest ionization rates will occur along the center of the cavity. Initially, the MiPPT is designed to inject plasma from the center cathode, as seen in Fig. 2.5. However, this design proves to be ineffective and gas injection ports through the cathode are removed. In order to ensure uniform gas mixing in the pre-ionization chamber, swirl is going to be introduced into the cavity through vectored gas feeding lines.

Finally, sizing of the plasma injection holes will also be crucial. While previous analysis has determined a hole size of 0.10 cm, one still needs to model the plasma transport process. With this design, there are two parameters to consider. The first consideration is to contain microwave energy within the resonant cavity. The second consideration is to overcome the plasma quenching diameter. From Section 2.4, the maximum hole size before microwave energy can propagate is 7.0 cm. For the second consideration, one needs to consider the frequency of electron diffusion losses to the walls of the injection holes as it flows through the cylindrical hole. In calculating a hole size such that it will not quench the plasma as it flows through the hole, there are two general design guidelines. Referring to Fig. 2.6, the first guideline suggests that the diameter of the hole size

must be larger than twice the mean free path, lambda, of the plasma. The second guideline is that the length of the hole should be smaller than lambda. The second condition is often the weaker of the two conditions, and it often does not always need to be satisfied. Both of these conditions ensure that the plasma has a low probability of colliding and recombining with the walls of the cavity. However, there are still recombination losses due to electron-ion recombinations and electron-neutral particles collisions during this transport mechanism. These effects would be discussed in later chapters of this report.

Lambda for plasma can be calculated using the relationship below **[13]**:

$$\lambda_{rmp} = \frac{1}{n\sigma} = \frac{kT}{P\sigma} = \frac{1}{3.218 P_{Torr} \sigma_{\overset{o}{A}}} cm \qquad \text{Eq. 2.13}$$

For the performance of MiPPT, the plasma pressure, to a first order estimation, is essentially the gas pressure of the pre-ionization chamber. The collision cross section of argon plasma can be estimated as 140 Angs **[12]**. Using these two estimates for argon pressure, the mean free path is 0.037 mm. Hence, the hole must be larger than 0.074 mm. A convenient hole size of 0.10 mm is selected for the plasma injection ports. While smaller holes would allow more holes to be machined to the anode, the machinability and plasma diffusion losses will increase.

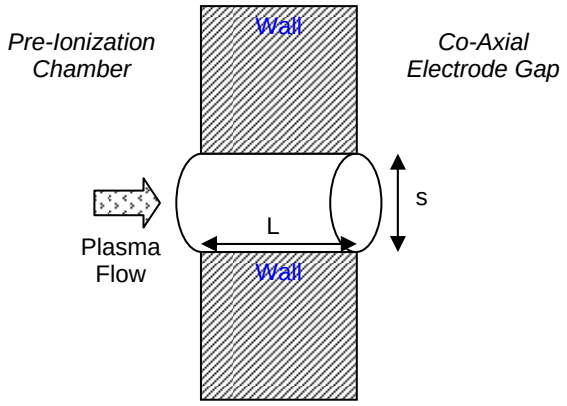

Figure 2.6: Plasma injection hole sizing. To prevent plasma quenching, the hole diameter, s, needs to be greater than twice the mean free path of the plasma; the hole length, L, should be less than the mean free path, although this is a weak condition and doesn't always need to be satisfied.

2.7 Mechanics of Undervoltage Breakdown

In order to design a proper cathode and anode, one would need a solid understanding of under-voltage breakdown, which is the principal discharge mechanism for all spark-initiated GFPPTs. To begin, the process of neutral gas breakdown is dependent on specific parameters which will minimize the voltage required for breakdown. In an electrode gap where there is an applied electric voltage, there is a stable electric field between the electrodes. The strength of this electric field is simply E = V/d. Gas breakdown occurs when the electric field strength exceeds a critical breakdown potential. When this happens, ionization frequency of the seed electrons exceed the diffusion frequency, which will lead to electron propagation. While electric potential effects gas breakdown, two additional parameters also influence the presence of gas breakdown. The first is gas pressure. If the pressure of the neutral gas increases, then the probability of electron-neutral particle collision increases. With a higher probability of collision, there are more energy and momentum transfer, and if the collision energy is

greater than neutral gas excitation energy, then ionization will occur. The second parameter to consider is electrode gap distance. If the gap distance increases, then electric field strength decreases due to the inverse relationship between electric field and gap distance. A lower electric field length would indicate a lower ionization frequency, since the number of high-energy collisions will decrease. The dependence between electric potential, gas pressure, and electrode gap distance is captured in the Paschen Curve **[13]**.

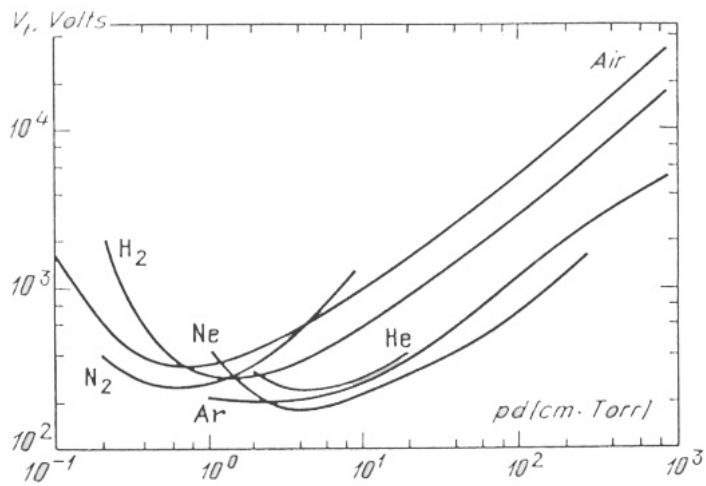

Figure 2.7: Breakdown voltage dependence on the gas pressure and electric-potential gap separation **[12]**. For most gases, there is a minimum voltage potential that is required for breakdown and this potential occurs at P*D*. If PD is smaller than P*D*, then the breakdown potential will increase due to the lower collision rates. If PD is higher than P*D*, the breakdown potential will also increase, because the average kinetic energy per collision will decrease (increased collision rates).

Even though the minimal voltage appears to be a logical voltage setting for PPT application, it turns out that one can obtain discharge even below this

setting, using a phenomenon known as under-voltage breakdown. With under-voltage breakdown, electrons from an external outside source are injected into the cathode-anode gap. They accumulate at the cathode and anode, thus forming a temporary spatial charge. This temporary spatial charge augments the electric field strength, and at a critical under-voltage setting, one can obtain a spontaneous discharge. The merits of under-voltage breakdown are that it requires less voltage for breakdown and it adds flexibility to create more uniform current sheets. With under-voltage breakdown, one can essentially "shape" the current sheet by essentially controlling where electrons are injected. By injecting electrons in an azimuthally symmetric fashion, one will ensure that discharge occurs uniformly. When spark plugs are reliable sources of electron, they inject them in a non-uniform fashion.

2.8 Anode and Cathode Design

The design of the anode, cathode, and electrode gap is limited by the design of the capacitor. The capacitor hardware is obtained from a SLR PT4/PT5 thruster to reduce cost and facilitate rapid prototyping of the MiPPT. The PT4/PT5 electrodes have an inner anode diameter of 2.20 cm and an outer cathode diameter of 5.27 cm; the electrode gap distance is 1.54 cm. From discussion of undervoltage breakdown, gas breakdown is a function of the electric potential, electrode gap, and gas pressure. In order to implement a PT4/PT5 capacitor into a MiPPT thruster, the MiPPT must operate in the same breakdown conditions as PT4/PT5. Given that the capacitors are only rated at a specific voltage, one would need to adopt the same gap distance from the PT5/PT5 to ensure that undervoltage discharge occurs successfully. Furthermore, for comparative reasons, the cathode and anode are designed using the same dimensions so a direct comparison between MiPPT and GFPPTs can be made. The finalized sizing of the electrodes can be seen in Fig. 2.5.

2.9 High Voltage Power Supply

The design requirements for a magnetron power supply is a high current power output (eight to ten amperes) for its cathode filament and a high voltage output (2000 – 3000 volts) to establish an electric potential between the cathode filament and the resonant cavities. In addition, the voltage output of the power supply needs to be attenuated, so that microwave energy output from the magnetron can be controlled. Finally, the power supply would need to be pulsed at a specified frequency, and hence, a pulsing circuit would need to be developed.

For the first challenge, obtaining a high voltage, high current power supply is rather expensive and beyond the budget limits of this project. However, most commercial microwave units are equipped with a high voltage, high current power supply. The caveat is that their power output cannot be varied and that they are not designed to be pulsed. Nevertheless, with slight modifications one could easily modify this power supply unit to include a variable transformer to control the power output. From previous discussions of a commercial magnetron, one understands that these units operate by emitting electrons from the cathode filament and these electrons are accelerated in a spiral fashion to produce an induced electrical and magnetic field. To control the power output, one could theoretically control the current input to the cathode filament, which effectively would control the number of electrons emitted from the filament and hence the power output of the magnetron. This can be accomplished by utilizing a variable transformer (i.e., a variac) to the AC input line of the high current transformer. Figure 2.8 shows the power schematic of a modified magnetron power supply with variable current output.

From Figure 2.8, one can notice that a 0.82 μF capacitor is used to "smooth" out the voltage output coming out of the high voltage transformer. Nevertheless, as one would notice in later of this section, the voltage output of this high voltage power supply is oscillatory, resembling a square wave. This would indicate that the capacitors have no influence in "smoothing" the voltage output. While this seems odd, it is not too surprising given that most commercial

microwave ovens utilize the most cost-effective components, which aren't exactly the most precise and reliable equipment for scientific measurements. The frequency of oscillation is approximately 60 Hz, which is the same frequency as AC power input to the transformers. Pulsing this power supply is a matter of pulsing the power input to the low voltage, high current filament transformer.

While one can easily pulse the power supply, it does not imply that one is able to pulse the magnetron effectively. The filament in the magnetron takes time to equilibrate, and this delay time will be critical in the pulsing scheme of MiPPT. Typically, a filament will take anywhere in the order of nanoseconds to warm up and emit electrons, which wouldn't effect the pulsation mechanism, since most gas-fed, pulsed plasma thrusters operate for microseconds during a second pulsing rate. Nevertheless, one interesting observation about the magnetron is that it takes a substantially long period to warm up and emit microwaves when it is initially powered up (usually on the order of 10 seconds. See Figure 2.10). This is noticed during a microwave leak test, in which a microwave probe is placed inside a Faraday cage with an exposed magnetron antenna. When the magnetron is initially powered, it takes approximately 10 seconds or so before microwaves can be detected by the probe. Before this time, no indications of microwaves can be observed on the microwave probe meter. If one is to analyze the voltage output during this initial 10 seconds, one would notice that the voltage output is much more negative (around -7 kilovolts). After ten seconds or so, the power supply stabilizes to a steady -4 kilovolts at 60 Hz, at which point microwaves can be detected. This is a rather bizarre phenomenon, and one could only speculate that this is a consequence of the low quality and workmanship of the electrical components.

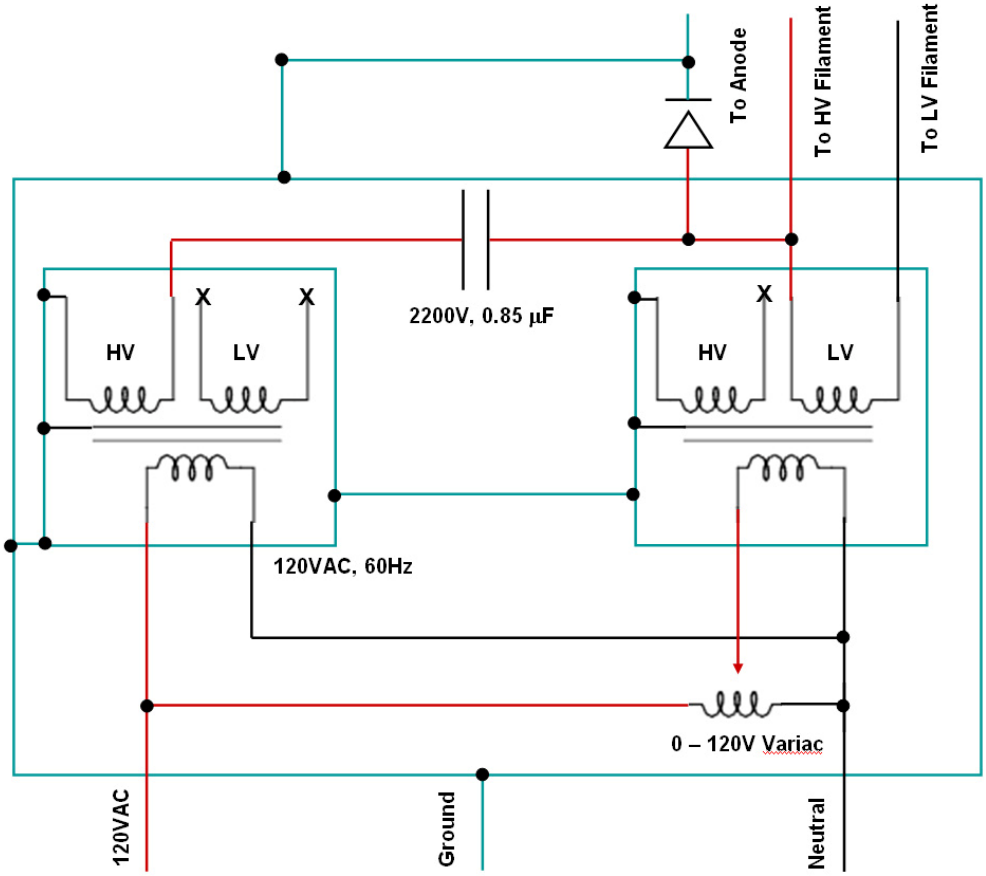

Figure 2.8: Magnetron high voltage power supply schematic with a variable power transformer. By varying the power input into the low voltage, high current transformer, one can effectively vary the power output of the magnetron. One important thing to note is that the anode or body of the magnetron is also connected to the cathode of the MiPPT. During normal operations, the cathode is kept at a 250V potential, which means that this entire power supply is "floating" at 250V.

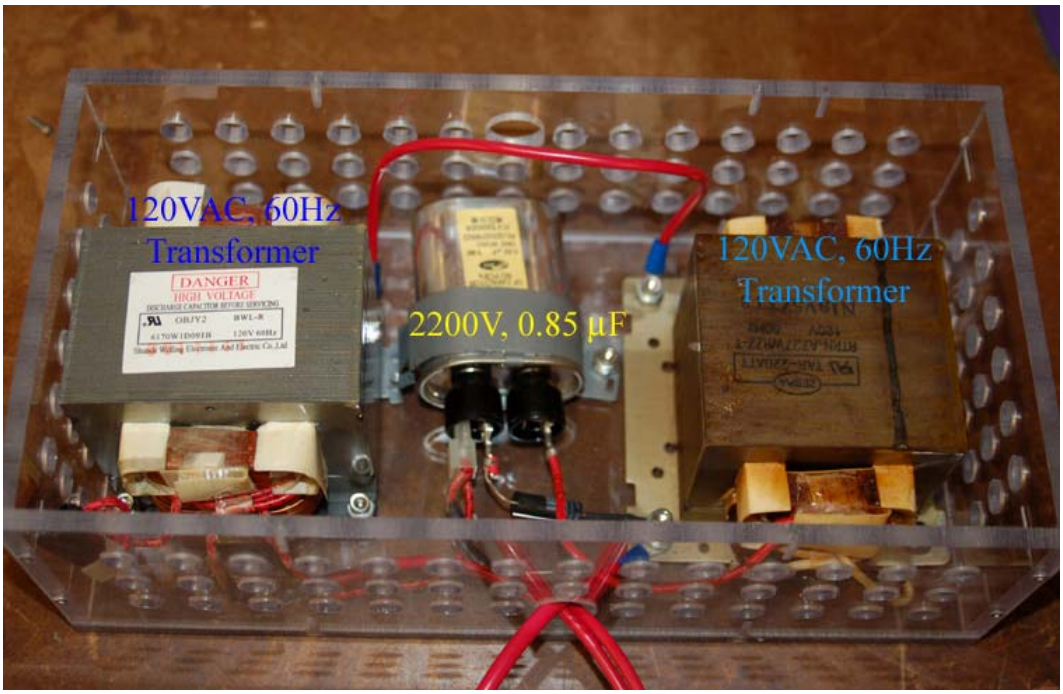

Figure 2.9: Image of the high voltage power supply incased in non-conducting, clear acrylic box. A non-conducting acrylic box is used, because the power supplies are floating at 250V.

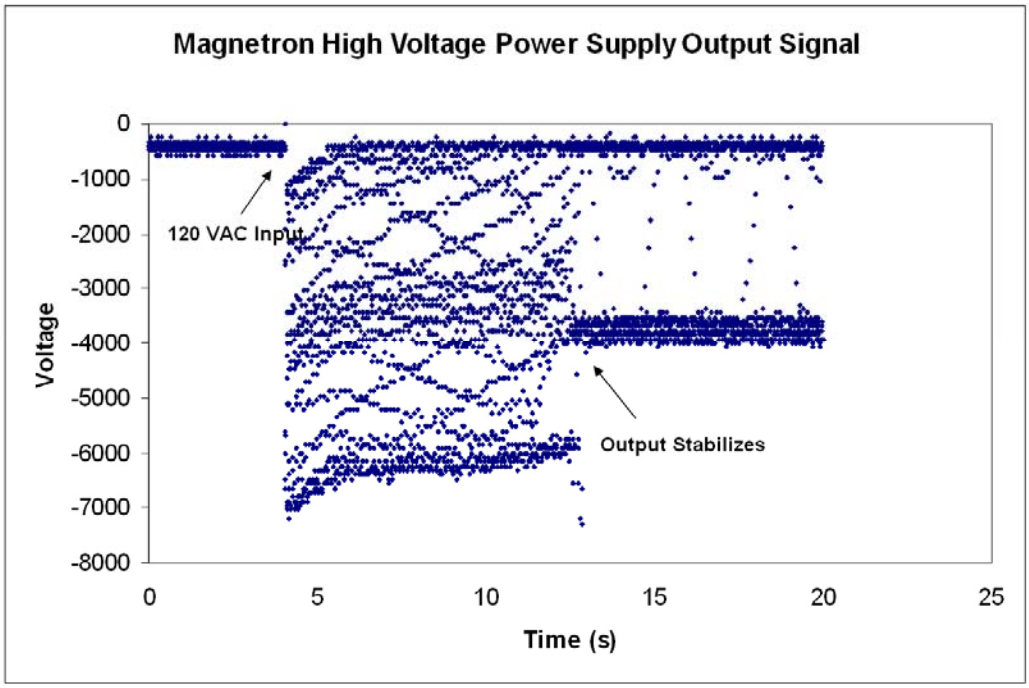

Figure 2.10: Voltage output of the high voltage, high current power supply during the initial 15 seconds. It takes approximately 10 seconds before the power stabilizes to give a 60Hz step function with a voltage output of 0 to -3800V.

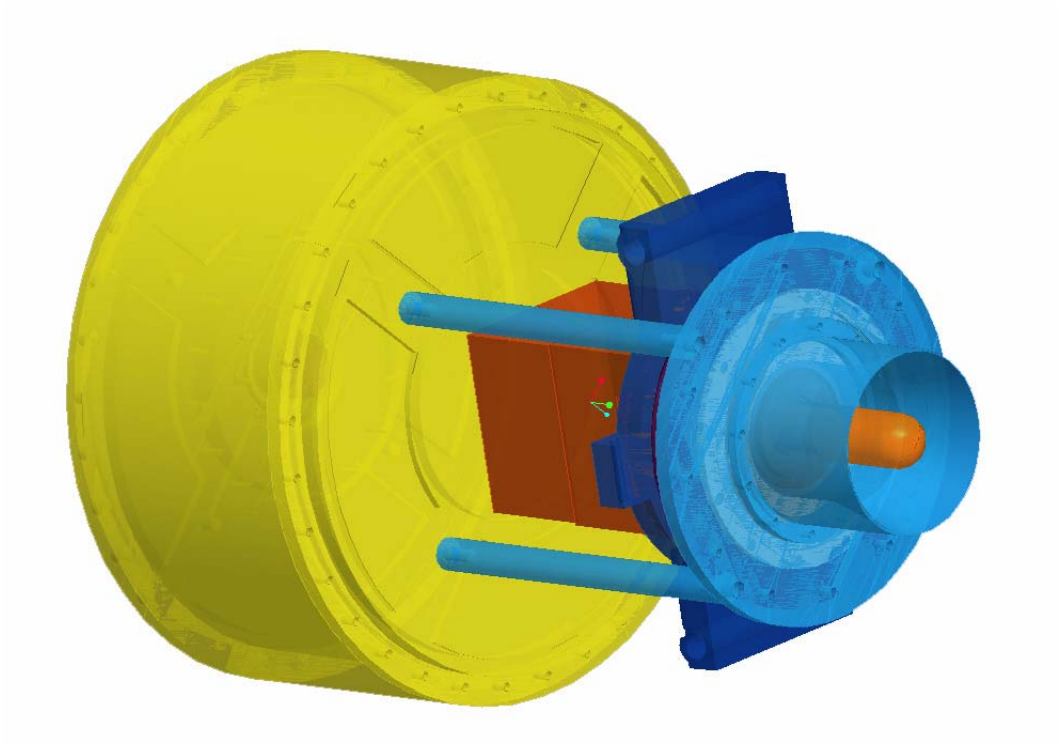

Figure 2.11 CAD schematic of the final design configuration of the MiPPT. Missing from this schematic are the capacitors (located inside the yellow outer cover), the water cooling lines, and the gas injection lines.

Chapter 3: Finite Element Analysis and Plasma Model

The analysis presented in previous sections of this paper offers a broad perspective on the design of the MiPPT. For example, the mathematical derivation of an ideal microwave cavity does not include geometric deformities or the influences of dielectric fillings inside the microwave cavity. Moreover, the plasma injection mechanism would need to be carefully analyzed to ensure successful electron transport across the microwave cavity. For both of these challenges, one needs to obtain a more concrete simulation of the MiPPT by employing much more capable software and developing a comprehensive plasma model. The first challenge is to model the microwave cavity in its entirety in a finite element program such as Comsol Multiphysics. The second challenge involves analyzing atomic ionization and electron loss rates. In this section of the paper, a through description of both of these models is presented to elucidate some of the issues to take into consideration during the testing phase of this project.

3.1 Microwave Field Model Utilizing Finite Element Analysis

Although the microwave cavity used for MiPPT is designed to sustain a TM_{010} resonant mode, there might be other modes that are excited due to the manufacturing inaccuracies and the presence of other deformities on the cavity. For example, holes would need to be machined into the cavity for gas feeding lines and microwave antenna. Furthermore, the presence of a Teflon dielectric used to seal the cavity will further deviate the cavity from an ideal, perfectly tuned TM_{010} microwave cavity. In order to analyze the effects of all these characteristics of the MiPPT microwave cavity, a finite element model will be used to analyze the electromagnetic fields inside the cavity. For this task, a highly specialized finite element and modeling software, Comsol Multiphysics (Femlab) v3.2, is used.

One of the most difficult tasks of modeling using finite element analysis is to determine whether one's model captures all the physical processes occurring inside the model. While Comsol Multiphysics has the capability of integrating electromagnetic effects with fluid dynamics and heat transfer, the model developed for this project only analyzes electromagnetic effects. The assumption behind this is that the gas flow and heat transfer do not affect the resonant electromagnetic fields. However, one important point to keep in mind is that when gas breaks down, one then has a conductive plasma inside the cavity. At this point, the electrical characteristics of the plasma will begin to have an effect on the resonant mode of the cavity. Nevertheless, for the purposes of this model, one only wishes to analyze the resonant fields before gas breakdown. Once breakdown has occurred and capacitors are discharged, the electromagnetic field distribution is no longer of interest. Hence, analyzing the non-plasma electromagnetic field distribution would be sufficient for this project.

Using Comsol Multiphysics serves many advantages for finite element modeling. For instances, it has an interactive three-dimensional environment and it doesn't require any esoteric computer programming language. Obviously, with all computer programs, there are limited flexibility in allowing the user to define

certain parameters. While the physical modeling of the microwave cavity with all dielectric insertions, holes, and magnetron antenna is fairly straight-forward, one challenge that has been encountered is the modeling of the magnetron antenna. The antenna of the magnetron is simply a stub antenna with an inductive loop at one end to extract microwave energy from the magnetron resonant cavities. Basically, microwave energy from the resonant cavities induce a current flow in the antenna, which flows to the stub antenna and radiates into space as electromagnetic fields. While this is a fairly simple concept, Comsol Multiphysics does have not seem to have the feature to specify these parameters. Rather, all microwave energies are emitted from a feature known as a "port," which effectively is analogous to a waveguide opening. Unfortunately, this is also the most critical aspect of this microwave field model, since a microwave source and its coupling characteristics define the resonant electromagnetic fields inside the cavity. Hence, since a stub antenna is not a waveguide, modeling the antenna is rather cumbersome. To overcome this challenge, two approaches have been developed to mimic the characteristics of the stub antenna. In the first approach, one models the stub antenna by defining the electrical field vectors on the surface of the antenna. In the second approach, one will attempt to model the antenna as a probe from a co-axial transmission line.

3.1.1 TEM Microwave Source with Defined Electrical Field Vector

While modeling the magnetron antenna with directional current flow is not a feature with Comsol Multiphysics, one can model the antenna by defining the electric field vectors on the surface of the emitting plane. With Comsol Multiphysics, one needs to first select the source plane (which is simply the surface of a cylinder representing the antenna) and define that as the "port." The next phase is to determine the microwave resonant mode type (i.e., transmagnetic, transelectric, or transelectromagnetic). Since current is flowing on the surface of the magnetron, the electric fields will lie parallel to the surface of the antenna. Assuming that the microwave direction of propagation is normal to the surface (see Figure 3.1), one would need a mode where the electrical field lies in the

transverse direction, either transverse electric (TE) or transverse electromagnetic (TEM). As one would encounter later, either one of these modes would give the same results. The next phase is to determine the mode number, which adopts the same number notation as any resonant microwave modes. Rather than selecting a specific one, one could choose to manually define the electric or magnetic fields to define the mode. In this case of a cylindrical stub antenna, one can define the electric fields to lie within the axial direction of the cylinder (which is parallel to the surface of the cylindrical surface).

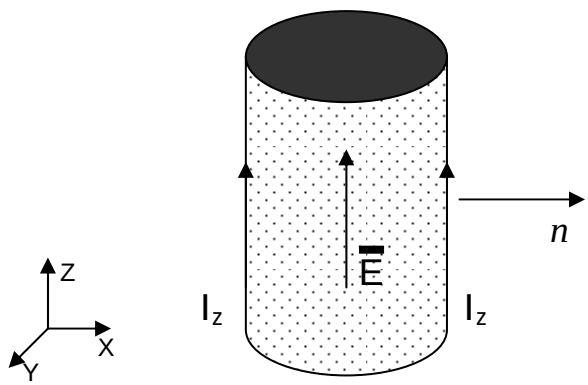

Figure 3.1: Comsol Multiphysics Microwave Antenna Modeling. A cylinder is used to model a magnetron stub antenna. The direction of propagation is normal to the surface of the cylinder, and the electric fields lie in the axial direction of the cylinder.

The results of the finite element analysis of the electromagnetic field stimulation can be seen in Figure 3.3. As one will notice, the electric fields are symmetric with the highest intensities along the center axis of the cavity. Electric field intensities decrease with distance from the center axis, which are confirmed by theoretical calculations from previous section of this report. For the most part, the electric field intensities are fairly uniform with minor discrepancies due to the mesh sizes of the finite element analysis and structural imperfections in the

cavity. While the electric field agree well with theoretical calculations, the normalized magnetic field intensities appear to be fairly weak, relative to the intensities around the stub antenna (see Figure 3.3.b).

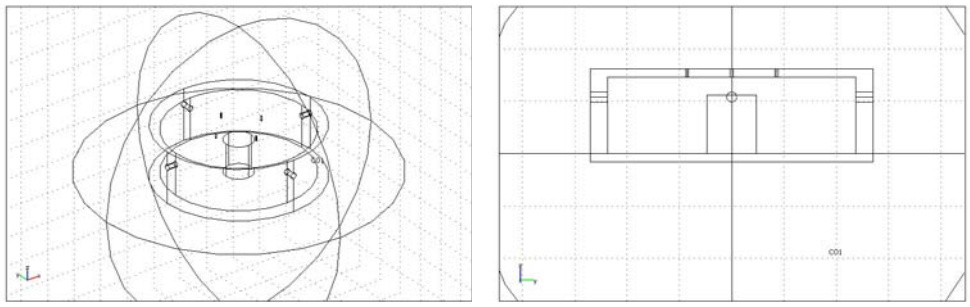

Figure 3.2: Three-dimensional CAD drawing of the microwave cavity with a magnetron antenna. The antenna has dimensions 19 mm in diameter and 21 mm in length.

Even though the magnetic field intensities are not as strong as previously predicted with theoretical calculations, the simulation is fairly indicative of what theoretical predictions would show. Nevertheless, there are still issues that need to be addressed with this model. For example, one needs to question the influences of a microwave source on the local electromagnetic fields. It is no surprise that the electric and magnetic fields are both strongest closest to the antenna, but the question arises as to whether there is actually a resonant mode inside this cavity. It is difficult to determine what the resonant mode the antenna is actually exciting, given the dominating field intensities being emitted from the surface of the antenna. In order to determine the mode that the antenna is exciting, a much small antenna would need to be stimulated.

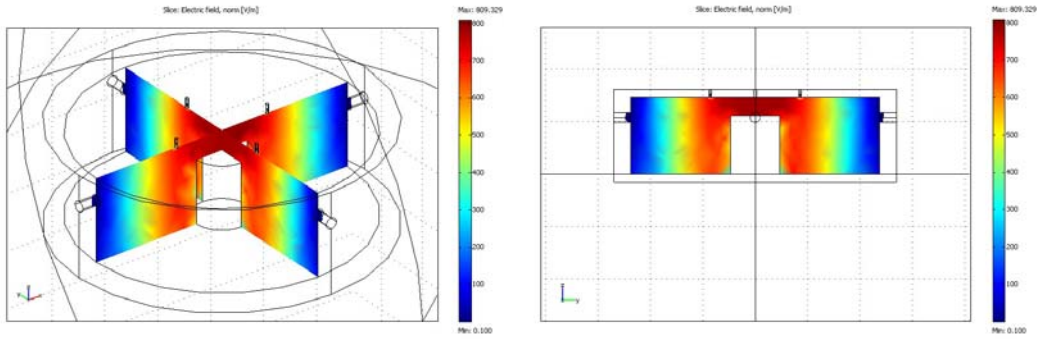

(a)

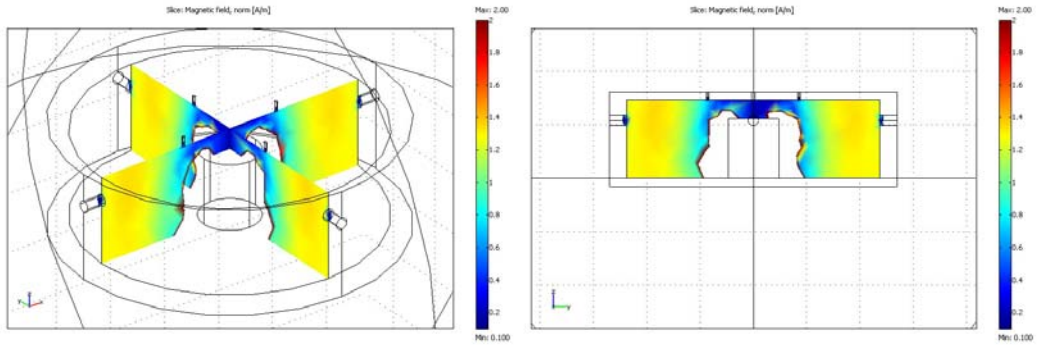

(b)

Figure 3.3: Comsol Multiphysics finite element analysis of electromagnetic fields in microwave cavity. **(a)** Normalized electric field intensities from an overview perspective and from a side perspective. **(b)** Normalized magnetic field intensities from an overview perspective and a side perspective. White regions inside the cavity represent intensities which are beyond the scale limit.

By replacing the antenna in the previous stimulation with a smaller antenna (6.4 mm diameter and 13 mm length), one can actually visualize the resonant mode that the antenna is exciting. As shown in Figure 3.4, the electric

and magnetic fields are similar to those in the previous stimulation with the large antenna. However, what differentiate these new results with the previous results are the field intensities. Rather than having the microwave fields from the antenna dominate the resonating fields, one can actually see the resonant electromagnetic fields inside the cavity. Similar to the previous simulation, the electric and magnetic fields both resemble those from a TM_{010} resonant cavity, with the magnetic fields being slightly weaker than predicted.

In addition to using a smaller antenna to visualize the induced electromagnetic fields, another approach that might be of future interest is to replace the stub antenna with a co-axial probe. While this doesn't serve a purpose for this project, it does enlighten future research in MiPPT if one decides to replace the magnetron and use a co-axial microwave transmission line. In terms of mechanical design, the advantage with this approach is flexibility in isolating the magnetron from the cathode of the thruster. As one may recall, the magnetron and the high voltage transforms are "floating" at 250 – 300 V, which could potentially be dangerous if something accidentally shorts the circuit. By isolating the two parts, one could reduce the risk of shorting this system.

3.1.2. MiPPT Cavity with Co-Axial Coupling

One of the main advantages with Comsol Multiphysics is the ability to model a co-axial microwave source with alacrity and ease. The software has predefined parameters set in memory, which simplifies the modeling for the user. For a stimulation of the electromagnetic fields using a co-axial transmission line and probe antenna, one simply has to enter the geometry into the software and determine the plane where the co-axial microwave source will be emitting from. Figure 3.5 shows a three-dimensional CAD model of the microwave cavity used in this simulation.

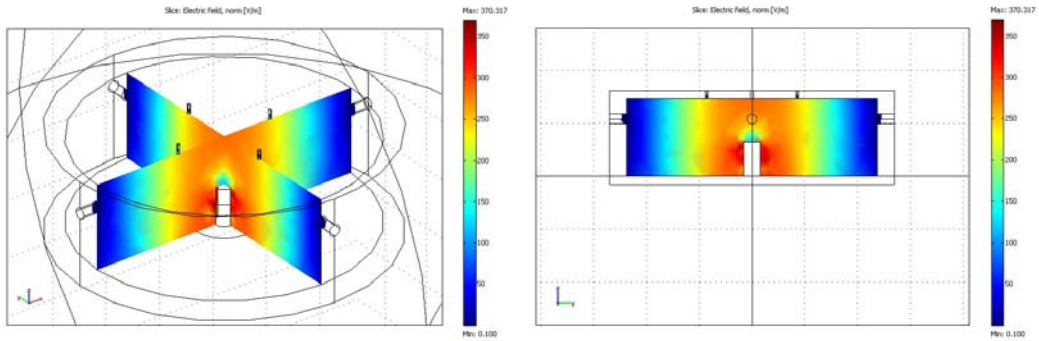

(a)

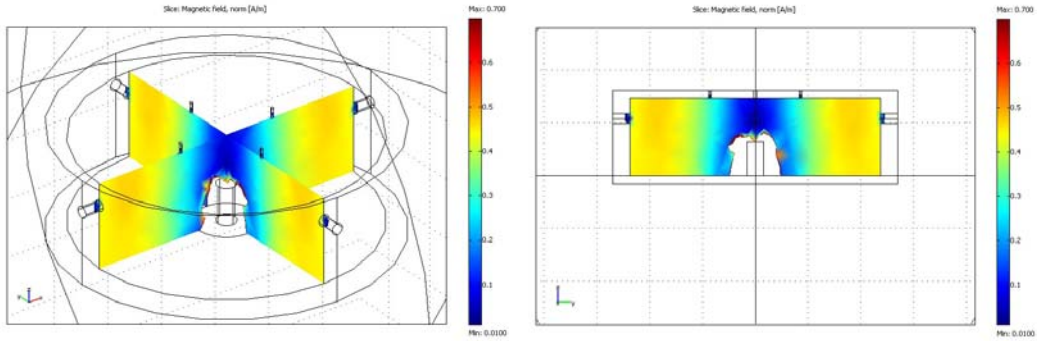

(b)

Figure 3.4: Comsol Multiphysics simulation of electromagnetic field intensities of a TM_{010} microwave cavity with antenna dimensions 6.4 mm diameter and 13 mm length. **(a)** Electric field intensities from an overview angle and side angle. **(b)** Magnetic field intensities from an overview angle and side angle.

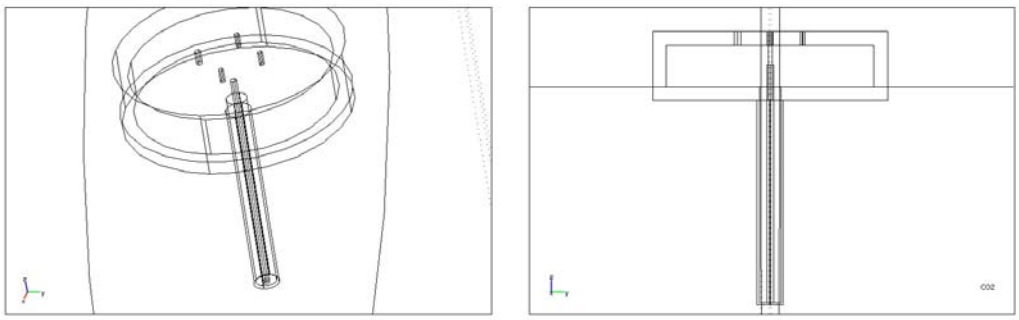

Figure 3.5: Three-dimensional CAD drawing of microwave cavity with a co-axial transmission line. The dimensions of the cavity are same as those used for previous simulations with stub antenna. The co-axial transmission line has a length of 100 mm and diameter of 12 mm. Internal center wire has a diameter of 3.0 mm and it penetrates 13 mm into the cavity.

The stimulation results using a co-axial transmission line to couple to a microwave cavity can be seen in Figure 3.6. Similar the electromagnetic fields from two previous stimulations with a stub antenna, the highest field intensities lie around the antenna (or, probe in this stimulation). Nevertheless, the electromagnetic field distribution that is excited with this microwave cavity clearly resembles those of a TM_{010} mode. One interesting note is that the electric field intensities above the antenna do not seem to be as strong as those around the antenna. This same result can be seen in the small stub antenna stimulation, where the fields are actually arcing over the top of the antenna. This doesn't seem to be the case with the long stub antenna, where the electric fields are actually more intense above the antenna. As one has already seen before, this might be a consequence of the geometric characteristics of the antenna.

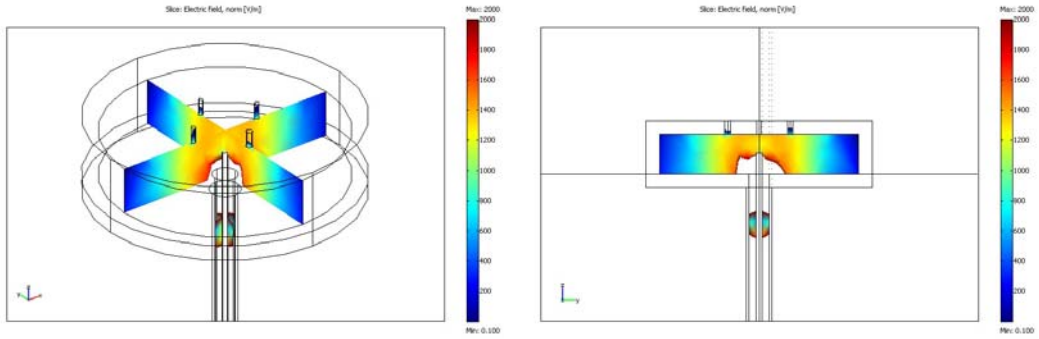

(a)

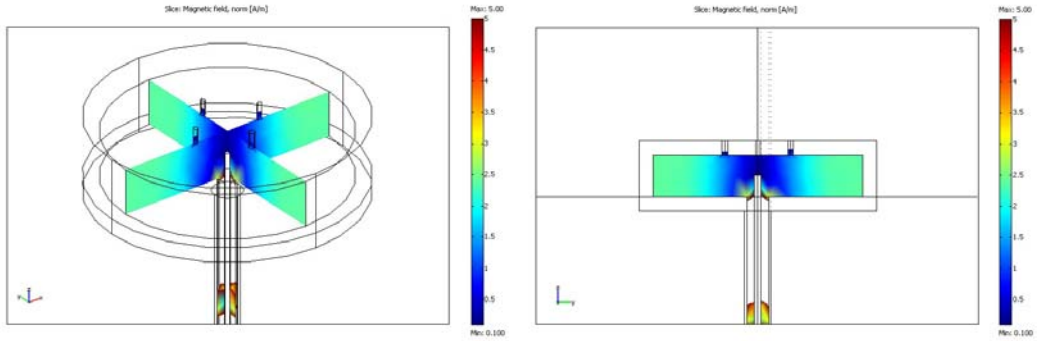

(b)

Figure 3.6: Comsol Multiphysics simulation of the electromagnetic fields inside a TM010 microwave cavity with a co-axial transmission line. **(a)** Normalized electric field densities from an overview angle and a side angle. **(b)** Normalized magnetic field densities from an overview angle and a side angle. The white regions inside the cavity indicate of intensities higher than the given scale.

In both the simulations with a stub antenna and a co-axial transmission source, one notices that maximum electromagnetic fields tend to surround the microwave antenna source. One can use these results to motivate the design of the internal Teflon filling. As discussed in early sections of this report, the design requirements for the Teflon filling is to be able to seal cavity in vacuum as well as provide adequate mixing of the gas and plasma before they are injected to the outer electrodes. From these results, one can add an additional requirement to deliver the gas to a region around the antenna where the electromagnetic field intensities are greatest. However, if the gas is too close to the antenna, the gas might melt the Teflon.

3.2 Plasma Model

The plasma model describes the electron loss rates when the microwave fields disappear, such as when the plasma is transported across an injection port. As one recalls from the previous section of this paper, microwave plasma is initially generated in the microwave cavity which will then be injected across a pressure gradient through a hole. The diameter of this hole is designed so that the flow is choked and the microwave energy would not be able to propagate across this hole. Since one objective of this design is to successfully transport plasma across this hole without significant plasma recombination rates, one would need to analyze how plasma decays with time. In order to do so, a better understanding of the ambipolar diffusion rates, radiative recombination rates, and dissociative recombination rates would need to be obtained.

3.2.1 Ambipolar Diffusion Losses

In the presence or absence of a microwave field, electrons will encounter ambipolar diffusion losses, or losses to the walls of the cavity, injection holes, and dielectric insertion. The ambipolar diffusion rate can be given simply as:

$$\left(\frac{\partial n_e}{\partial t}\right)_{diffusion} = -\nu_{diff} N_e = -N_e\left(\frac{D_a}{\lambda^2}\right) \qquad \text{Eq. 3.1}$$

n_e = initial electron charge density
D_a = ambipolar diffusion coefficient
λ = effective radius of the cavity

From Raizer **[13]**, the ambipolar diffusion coefficient can be given by Eq. 3.2 and the effective radius of a cylinder can be given by Eq. 3.3.

$$D_a \approx D_e \frac{\mu_+}{\mu_e} = D_+ \frac{T_e}{T} = \mu_+ \frac{k_b T_e}{e} \qquad \text{Eq. 3.2}$$

D_e = electron diffusion coefficient
μ_+ = mobility of the ions
μ_- = mobility of electrons
D_+ = ion diffusion coefficient
T_e = temperature of electron
T = temperature of gas
K_b = Boltzman's Constant
e = electron charge

$$\left(\frac{1}{\lambda}\right)^2 = \left(\frac{2.4}{R}\right)^2 + \left(\frac{\pi}{L}\right)^2 \qquad \text{Eq. 3.3}$$

R = radius of injection hole
L = length of injection hole

Substituting Eq. 3.2 and Eq. 3.3 into Eq. 3.1, one would obtain the ambipolar diffusion rate of electron recombination.

$$\left(\frac{\partial n_e}{\partial t}\right)_{diffusion} = -N_e \mu_+ \frac{k_b T_e}{e}\left(\left(\frac{2.405}{R}\right)^2 + \left(\frac{\pi}{L}\right)^2\right) \qquad \text{Eq. 3.4}$$

3.2.2 Radiative Recombination Losses

The loss of electrons associated with radiation recombination is of the form A(+) + e → A + hvu. The recombination coefficient associated with this mechanism is dependent on two main factors, mainly the frequency of recombination and the cross section of collision. Generally, an approximate model of this process can be given in Eq. 3.5 **[7, 17]**.

$$\left(\frac{\partial n_e}{\partial t}\right)_{RR} = -\bar{v}_e \sigma_c N_e^2 \qquad \text{Eq. 3.5}$$

ν_e = electron collision frequency
σ_c = cross section of collision
N_e = initial electron density

For simplicity, one can assume a Maxwellian electron energy distribution, which would give an average collision frequency given by Eq. 3.6 **[13]**. For the specific case of argon plasma, the collision cross section has well been documented and its value can be found in **[18]**.

$$\bar{v}_e = \left(\frac{8 k_b T_e}{\pi m_e}\right)^{1/2} \qquad \text{Eq. 3.6}$$

T_e = temperature of electron particles
m_e = mass of electron

Finally, substituting the collision frequency and collision cross section into Eq. 3.5, one would obtain an equation for the radiative recombination decay rate.

$$\left(\frac{\partial n_e}{\partial t}\right)_{RR} = -\left(\frac{8k_b T_e}{\pi m_e}\right)\left(1.5\times10^{-19}\right)N_e^2 \; cm^{-3}s^{-1} \qquad \text{Eq. 3.7}$$

3.2.3 Dissociative Recombination Losses

Dissociative recombination involves a reaction scheme of the form A(2)+ + e → A + A*. Typically, this is the quickest mechanism of recombination in a cold plasma, such as those resulting from a glow discharge. The rate of electron decay associated with this process has a form similar to radiative recombination and it is presented in Eq. 3.8.

$$\left(\frac{\partial n_e}{\partial t}\right)_{diss} = -\beta_{diss} N_e^2 \qquad \text{Eq. 3.8}$$

β_{diss} = dissociative recombination coefficient.

For argon plasma, it has been shown that the recombination coefficient is a function of mainly of the electron temperature **[19]**. The exact relationship can be seen in Eq. 3.9.

$$\beta_{diss} = 9.1\times10^{-7}\left(\frac{300}{T_e(^oK)}\right)^{0.61} \qquad \text{Eq. 3.9}$$

Substituting the coefficient into Eq. 3.8, one would obtain the dissociative recombination decay rate of argon.

$$\left(\frac{\partial n_e}{\partial t}\right)_{diss} = -9.1\times10^{-7}\left(\frac{300}{T_e(^oK)}\right)^{0.61} N_e^2 \qquad \text{Eq. 3.10}$$

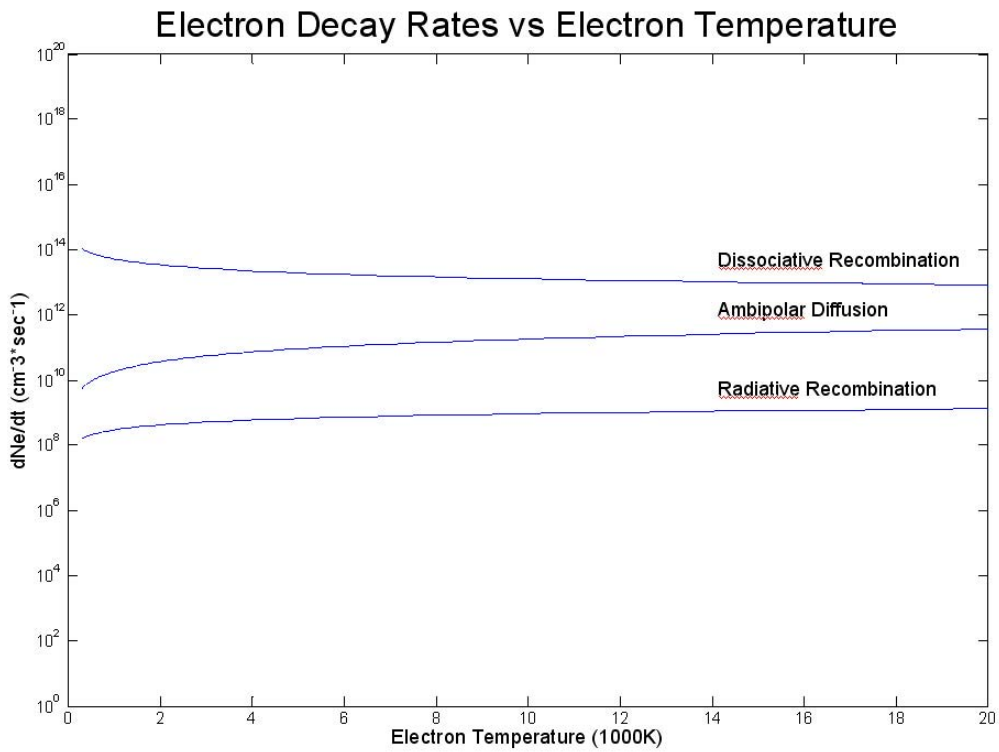

Figure 3.7: Electron decay rates as a function of electron temperature. This stimulation assumes a gas temperature of 400 K and an initial electron density of 10^{10} cm^{-3}.

3.2.4 Total Electron Decay Rate

With the three electron decay rate equations obtained above, one can then calculate the total electron recombination for during the plasma injection process. The cavity pressure has been found to be approximately 10 Torrs with a molecular temperature of around 400 Kelvin. Previous studies on microwave

argon plasmas have found that electron number densities at these conditions to be approximately 10^8 to 10^{12} cm^{-3} **[20]**. The upper extreme condition is typically found only in a perfectly tuned cavity with maximum energy transfer and a stable arc discharge. As described later in this report, the discharge inside the MiPPT resembles an arc discharge, but still not as dense and conductive as an arc discharge. A fairly conservative approximation of the electron number density inside the MiPPT would be around 10^{10} cm^{-3}.

The electron temperature range inside the MiPPT cavity ranges between 1 to 2 eV. Research on atmospheric argon arc discharges suggest a upper electron temperature of limit of 2 eV **[7]**. Since the plasma inside the MiPPT is a low-pressure plasma, the temperature should not exceed 2 eV. With values for the electron number density and the electron temperature, Eqs. 3.4, 3.7, and 3.10 can all be solved as function of electron temperature. The results of this calculation can be seen in Figure 3.11.

Figure 3.7 indicates that the dominant electron loss process is dissociative recombination. At an electron temperature of 1.0 eV, dissociative recombination decay rate is approximately two orders of magnitude greater than ambipolar diffusion and four orders of magnitude greater than radiative recombination rates. Considering only dissociative recombination as the dominant loss mechanism, the decay rate at 1.0 eV is approximately $1.167*10^{13}$ $cm^{-3}s^{-1}$. The total residence time of the plasma inside the injection holes can be estimated by first determining the sonic speed of argon at the given temperature and pressure conditions. While this may not represent the true speed of the electrons as it is injected across the ports, it does provide a lower limit on the speed of the electron (this speed actually represents the speed of the molecular ions as it flows across the hole, which is typically much slower than electrons due to their larger mass). The sonic speed can be given simply as $\sqrt{\gamma_{\arg on} R_{\arg on} T}$, and assuming negligible boundary layer effects, the residence time of the plasma is approximately 6.8 μsec. Finally, assuming a constant decay rate as the plasma flows across the injection port, the total electron density change during the injection process is approximately 8.0e7 cm^{-3}. Since the initial plasma density is approximately 10^{10} cm^{-3}, which is three

orders of magnitude greater than the total electron density change, the overall electron recombination and diffusion losses would have minimal effect in the injection of plasma across the injector ports.

It is important to note that while a constant decay rate is assumed, this would represent the upper limit in the total density change. As the plasma decays, the recombination rates decreases. However, the discrepancy between the time-varying recombination rate simulation and the constant rate simulation rate is minimal (less than 0.01 percent). Hence, results from this analysis indicate that that a hole diameter of 0.1 cm is sufficient to allow enough plasma to be injected without being recombined or lost to walls.

Chapter 4: Characterization of MiPPT

As a conceptually new gas-fed pulsed plasma thruster, the MiPPT requires extensive testing to understand the limitations of the operation envelope of this thruster. Some essential performance parameters include thrust output, mass efficiency, specific impulse, and power consumption. While these parameters are important for final detailed design, they are not critical for initial testing. The first stages of development would focus on demonstrating the feasibility of a microwave induced breakdown and to show the improvements of this concept over other pulsed plasma thruster designs. Hence, at this stage, understanding the fundamental parameters, such as plasma inductance, resistance, and residence time, are the main emphasis of the experiments described in the following sections. With a solid understanding of these fundamental characteristics, one can then apply optimization techniques to improve performance, reduce weight, and enhance reliability.

The first series of experiments will concentrate on producing microwave breakdown with high reliability. Once microwave breakdown can be achieved, the

next stage of development is to produce a current sheet, which essentially demonstrates the thrust producing capability of the MiPPT. By analyzing the structure of the current sheet, one can gain insight into the performance of the MiPPT and its advantages or disadvantages over other gas-fed, pulsed plasma thrusters.

4.1 Visualization of Microwave Plasma

Among one of the first validations of the resonant mode calculations and finite element analysis of the resonant cavity is to demonstrate gas breakdown using a prototype cavity. As one may recall in previous sections, breakdown in microwave fields is dependent on various parameters, mainly the intensity of the electric field strength, the frequency of field oscillations, and the gas pressure. Using argon gas, previous research has characterized microwave breakdown at various microwave frequencies **[20]**. Results for argon breakdown at 2.80 GHz is reproduced in Figure 4.1 to provide an approximation of the test conditions of the MiPPT experiments **[13]**. From Figure 4.1, the minimum electric potential required for breakdown occurs at around a gas pressure of 2 to 8 Torrs, and thus, one would expect breakdown to occur in this gas pressure range. While the frequency used for MiPPT is 2.45 GHz, the discrepancy between comparing a 2.8 GHz and 2.45 GHz argon breakdown should be minimal since the cutoff frequency of higher older resonant modes using this cavity geometry is around 3.2 GHz.

From Figure 4.1, the curve for gas breakdown at 2.8 GHz is negatively slopped below 4 Torrs and positively sloped above 4 Torrs. This suggests that one would need higher microwave energy density as pressure increases or decreases above or below 4 Torrs, respectively. For the experiments described below, initial breakdown is attempted at around 1 – 10 Torrs. In order to operate below or above this gas pressure range, one would need to improve the energy transferred to the cavity using appropriate tuning techniques. From previous experiments measuring power transferred to microwave cavity, it has been roughly estimated

that 200 to 300 Watts are transferred to the cavity when the magnetron is powered on. The magnetron has a rated power of 700 Watts.

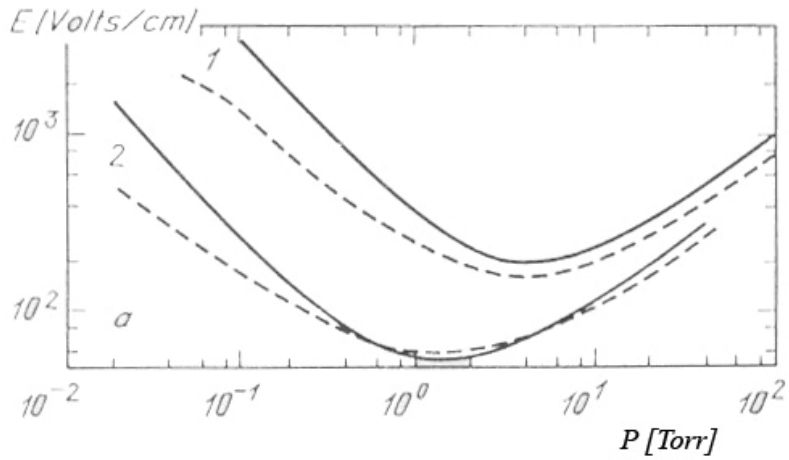

Figure 4.1: Minimal electric field distribution for argon breakdown at 2.8 GHz at various microwave frequencies. **1)** Breakdown frequency is 2.8 GHz. **2)** Breakdown frequency is 0.99 GHz. Dotted curve representing experimental data and solid curve representing theoretical calculations **[13]**.

The goal of the first series of experiments is to determine the minimum pressure at which plasma can by stabilized by microwave energy. To accomplish this, a MiPPT prototype without a cathode is mounted onto a Plexiglass vacuum gas chamber with the back of the thruster positioned into the tank. The tank is pumped down to 0.1 mTorr pressure with a roughening pump, followed by a diffuser pump. Once the cavity is in vacuum, gas is injected into the cavity of the MiPPT prototype and the high voltage magnetron power supply is switched on. Gas pressure and mass flow rate can be controlled by an external needle valve on the gas injection line. One can determine the minimum gas breakdown pressure by varying the gas pressure and looking for the presence of a bright clear, violet

light inside the microwave cavity. A schematic of experimental setup is seen in Figure 4.2.

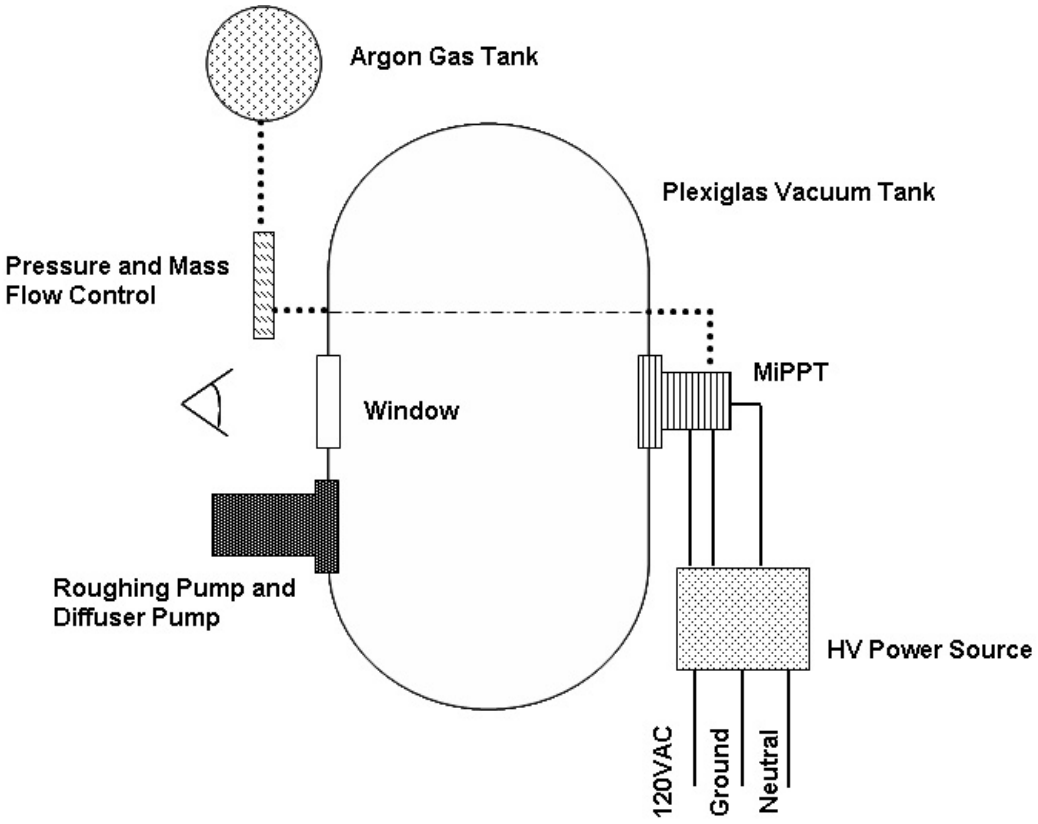

(a)

Figure 4.2 ***(a)***: Simplified schematic experimental setup of argon breakdown visualization.

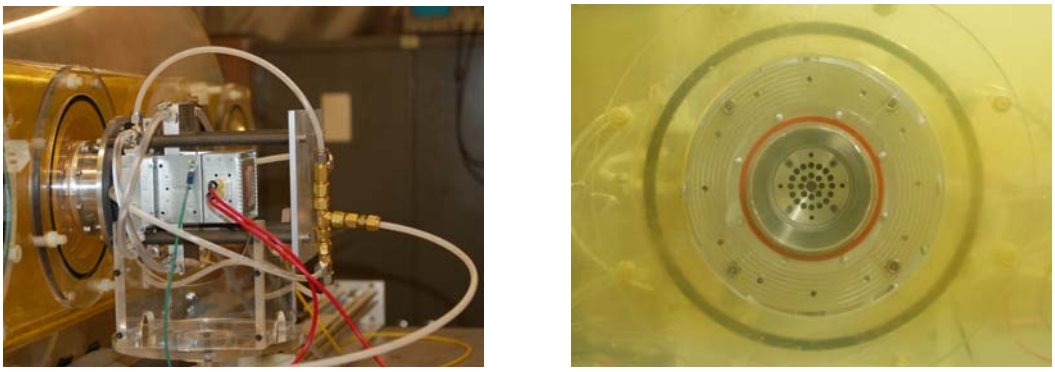

(b)

Figure 4.2 ***(b)****:* MiPPT prototype mounted into the plexiglass vacuum tank. Image of the electrodes of the MiPPT without the center cathode. In its place is a faceplate sealed with clear acrylic window.

Given the experimental setup described above, argon gas is injected into microwave cavity and pressure is increased until plasma is formed. It is found that the minimum and maximum pressure for gas breakdown is approximately 7.0 Torrs and 13 Torrs, respectively. While the plasma itself is difficult to distinguish between each pressure conditions, one detail that has been noticed during these experiments is that the plasma at higher pressure breakdowns tend to be hotter and brighter in color. While one can sustain plasma at 0.70 Torrs for long periods of time without any material failure (over 5 minutes), sustaining plasma at 13 Torrs for 2 to 5 minutes usually results in material failure of the inside Teflon filling. Figure 4.3 shows a sequence of images of the microwave plasma taken at a pressure of 13 torrs.

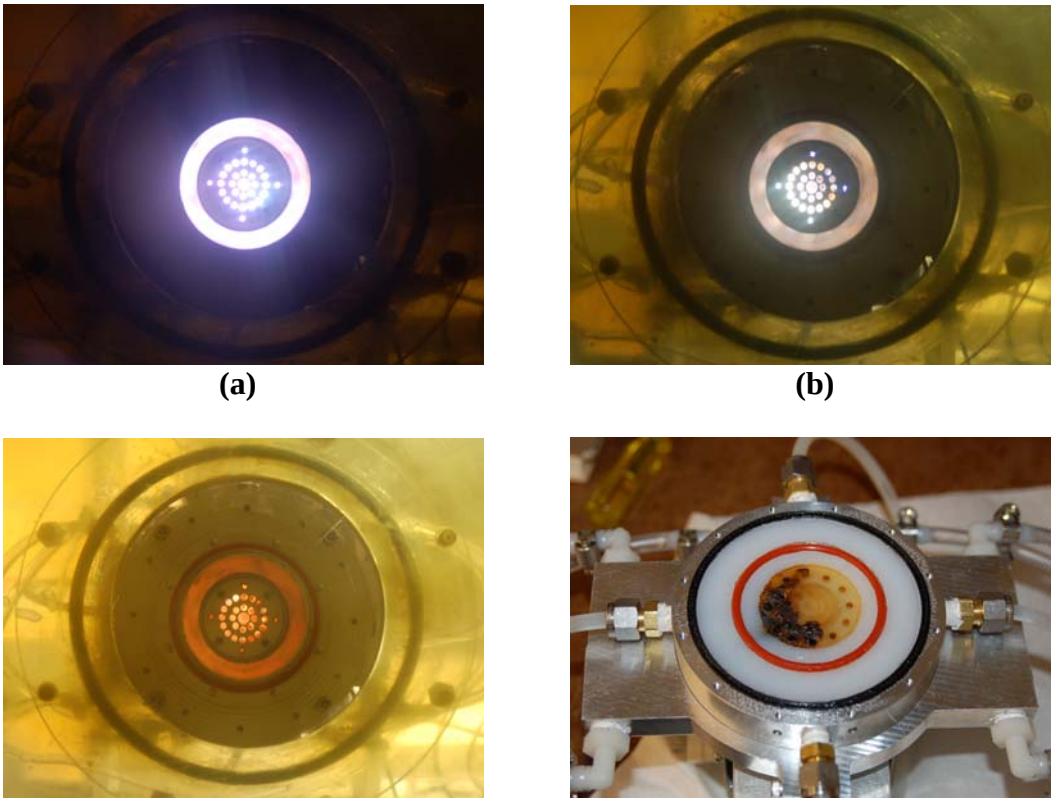

(a) **(b)**

(c) **(d)**

Figure 4.3: Images from microwave plasma visualization over a period 2 minute period at a gas pressure of 13 Torr and a mass flow rate of 5.0 mg/s. **(a)** Initial microwave breakdown with bright discharge glow. **(b)** Microwave breakdown after a period of 1 minute. Initial signs of Teflon ablation can be seen. **(c)** Microwave breakdown after a period of 2 minute. The light spectrum is dark red, indicating heavy Teflon ablation inside cavity. **(d)** Visualization of the failed Teflon after complete ablation.

Another detail that is worth nothing is the time evolution of the plasma as it is sustained in the cavity for long durations of time. When a 60Hz power supply

is applied to the magnetron, the magnetron emits microwave power intermittently into the cavity. If the power loss rate in the cavity is less than power absorption rate, the total power in the cavity will theoretically build up with time. This essentially increases the power that is absorbed by the plasma, which increases the temperature and intensity of the plasma. This can also be seen visibly as the plasma transforms from a bright clear light into a dark violet blue light, followed by dielectric material ablation and eventually, material failure. Figure 4.3 outlines such a sequence of events; from these visualizations, one can deduce that the initial plasma is fairly inchoate and suffers from radiative losses (similar to a glow discharge). As time progresses, power builds up in the cavity, which intensifies the plasma, creating a denser and hotter plasma

A final detail which will have significant impact in later discussions is the structure of the plasma inside the microwave cavity. From Figure 4.3(a), there is a presence of a slight bias in the light intensity spectrum. One can notice that a corner of the visualization window is more brighter than the rest, indicating a slightly higher energy density. Furthermore, from analyzing the pattern of the failed Teflon filling (Figure 4.3(d)), only one region of the Teflon actually failed, suggesting that plasma inside the cavity is skewed in energy distribution. More evidence suggesting this bias can be seen in later experiments, but initial implications suggest that this would lead to an azimuthally non-symmetric current sheet.

4.2 Microwave Plasma Characterization

In order for plasma to conduct current to form a current sheet, it is essential that the resistance of the plasma be extremely low. In previous pulsed plasma thrusters, the resistance of plasma produced using under-voltage breakdown is in the range of milli-ohms to one ohm. One of the main reasons why a low resistance plasma is required lies in the capacitor discharge time; by reducing the resistance, one would have reduced the RC time constant, resulting in a quicker discharge.

In measuring the resistance of the microwave plasma, a 100 kOhm resistor is connected in series with the 1.0 kV power supply to the cathode of the MiPPT. When gas breaks down, current is conducted through the plasma; as the plasma intensifies, there is a time-varying characteristic resistance associated with the plasma. One could measure this resistance by measuring the voltage drop between the two cathode and anode of the MiPPT and extrapolate the resistance function from basic electronic circuit theory. The experimental schematic is provided in Figure 4.4.

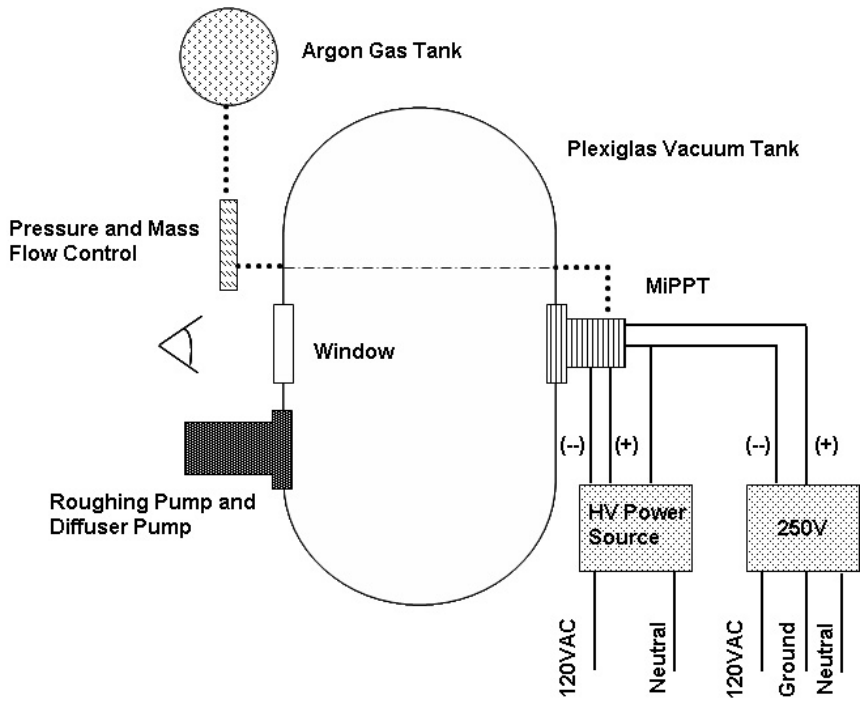

Figure 4.4: Simplified schematic diagram of the plasma characterization experiment. Missing from this schematic is the cooling water lines and the 100 kOhm resistance attached in series to the negative potential of the 250V power supply.

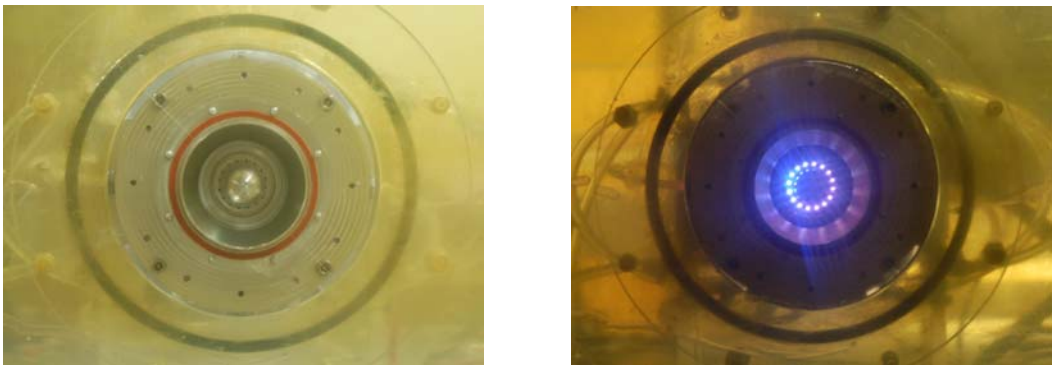

(a) **(b)**

Figure 4.5: Microwave plasma characterization experiment using a center cathode. **(a)** Visualization of the MiPPT electrodes in side the plexiglass vacuum tank. **(b)** Microwave plasma visualization of the MiPPT with center cathode and injection ports.

Results from the above experiments can be shown in Figure 4.5(b) and 4.6. In the plasma visualization experiment, one can visualize the ring structure from the injection port pattern. Similar to Figure 4.3, the plasma structure inside the cavity is fairly uniform with a slight bias in one side of the electrode. Implications of this result will be critical in the initial formation of a current sheet.

Figure 4.6 traces the voltage potentials in the magnetron high voltage power supply and the 250V bias to MiPPT electrodes. As discussed in previous discussions concerning the high voltage power supply, one notices that the HV power output is scattered for the first ten seconds before finally stabilizing at an output of approximately 2000-3000 volts. A short delay after the power supply stabilizes, there is a sharp voltage between the cathode and anode of the MiPPT drops, indicating the presence of a highly conductive plasma. The voltage drop oscillates between the initial 250V input and 0 volts at the same frequency of the HV power supply (60 Hz). This suggests that the plasma is pulsing at same rate as the power input. Essentially, when high voltage is applied to the magnetron, plasma is formed; when the high voltage is removed, the plasma disappears.

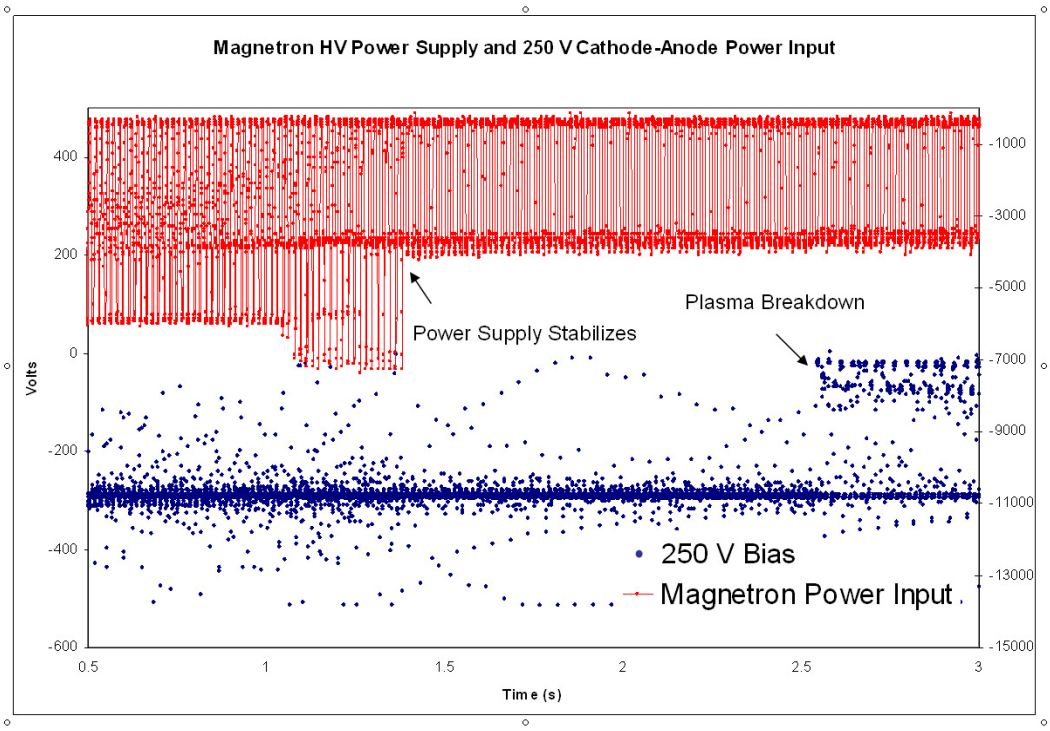

(a)

Figure 4.6(a): Voltage between anode and cathode of MiPPT at pressure of 9.0 Torr and gas flow rate of 0.70 mg/sec. Initial voltage between the cathode and anode of the thruster is 250 volts. **(a)** Extended image capture of the voltage output of the magnetron high voltage power supply and voltage between the cathode and anode.

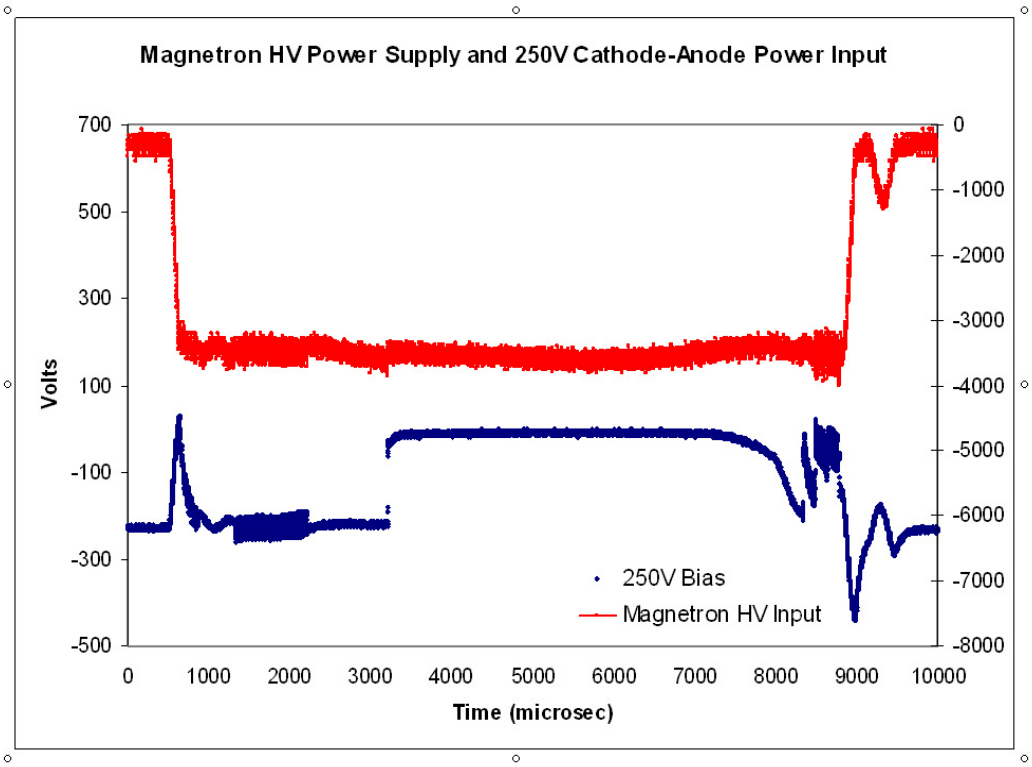

(b)

Figure 4.6(b): Voltage between anode and cathode of MiPPT at pressure of 9.0 Torr and gas flow rate of 0.70 mg/sec. Initial voltage between the cathode and anode of the thruster is 250 volts. **(b)** A refined image captured of the high voltage power supply and voltage between cathode and anode.

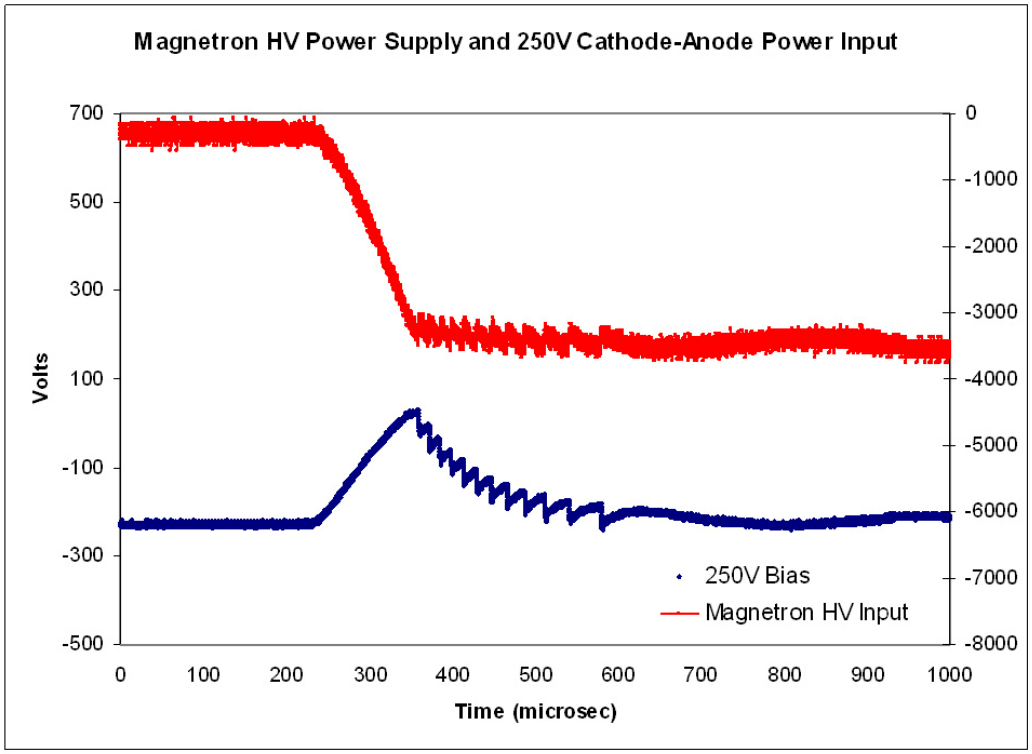

(c)

Figure 4.6(c): Voltage between anode and cathode of MiPPT at pressure of 9.0 Torr and gas flow rate of 0.70 mg/sec. Initial voltage between the cathode and anode of the thruster is 250 volts. **(c)** A response indicting the initial plasma breakdown that occurs. Once plasma is formed, the Q of the cavity significantly decreases, resulting in the plasma disappearing.

Figure 4.6(b) shows the actual response of the plasma when a high voltage pulse is applied to the magnetron. Once can see that plasma initially forms, disappears, and then returns in a stabilized form. Essentially, one phenomenon which could be causing this is the Q of the resonant cavity. Since plasma is

conductive gas, it significantly increases the Q of the cavity and hence, reducing the power transferred to the cavity from the magnetron. However, as power builds up in the cavity, the microwave energy becomes high enough to induce and sustain a secondary breakdown. Figure 4.6(c) indicates that the response time of the first breakdown is in the order of 150 microseconds. As discussed in the next section, this is more than sufficient time to form a current sheet.

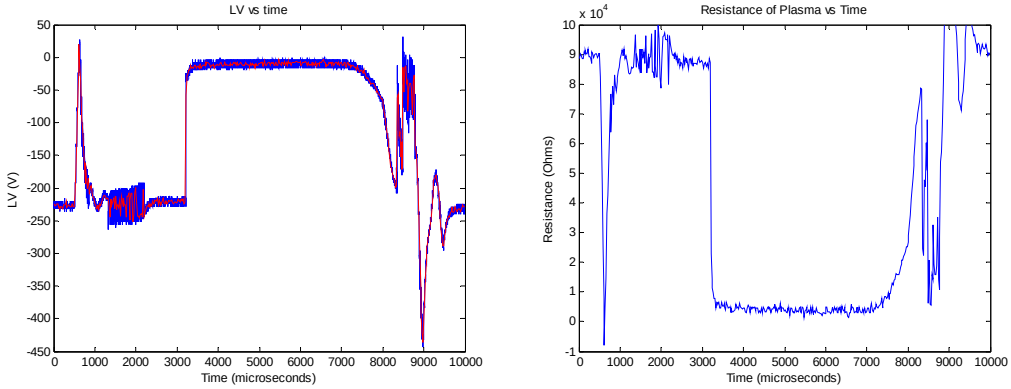

(a) **(b)**

Figure 4.7: Resistance of plasma as a function of time. **(a)** The blue curve represents the actual data points obtained. The red curve correspond to a polynomial spline-fitting function used to reduce the noise of the system. **(b)** The curve shows the resistance of the plasma and capacitor-cathode circuit as a function of time. The resistance can be calculated simply by solving the unknown resistance of the plasma with known values of a large series resistor (100 kOhms) and power supply voltage (250V).

In order to calculate the resistance of the plasma inside the cavity, one could model the entire system as a voltage divider. The 250V power supply is in series with a large resistor (100 kOhms) and the resistance of the plasma and MiPPT. When the circuit is closed (when plasma forms), one could measure the voltage drop, and the resistance of the plasma is simply a function of this voltage drop.

The time-varying resistance plot of a microwave plasma pulse indicates that the lowest plasma resistance occurs during initial phases of breakdown. As one can see from Figure 4.7(b), the sudden drop in voltage indicates the formation of a highly conductive plasma. Nevertheless, once plasma forms inside the cavity, the Q of the cavity is significantly reduced. The plasma can only be sustained for a period of about 100 – 200 milliseconds. As power amplifies inside the cavity over a period of 3 milliseconds, gas breaks down again, resulting in low plasma resistance.

4.3 Current Sheet Formation and Visualization

The formation of a current sheet between the cathode and anode of the MiPPT depends on a large change in current with respect to time. As one recalls, the goal of this project is to induce undervoltage breakdown by injecting plasma into the electrode gap. In theory, regions of highest plasma densities occur around the injection ports, since pre-ionized plasma is greatest around these regions. Since the injection ports are uniformly distributed around the back plate of the cathode, breakdown would then occur symmetrically, which will stimulate an azimuthally symmetric current sheet.

In order to clearly visualize the formation of a current sheet, a large capacitor bank would need to be attached in series to the cathode of the MiPPT. When pre-ionized plasma is injected into electrode gap, current is allowed to flow between the electrodes and the capacitors discharge. The sudden change in current induces an arc discharge which quickly ionizes the gases around the discharge, forming a conductive plasma medium. For these experiments, a 75 uF capacitor is connected in series to a 250V power source and the cathode of the thruster. An ultra-high speed camera, Imacon 729 LS, is projected into the back of the cathode and anode of the MiPPT. In order to trigger the Imacon camera, a current transformer is used to monitor the current flow between the electrodes. The signal from the current transformer is monitored by a high-speed oscilloscope, which

then releases a trigger to fire the Imacon camera. A simplified schematic layout of this experiment can be seen in Figure 4.7.

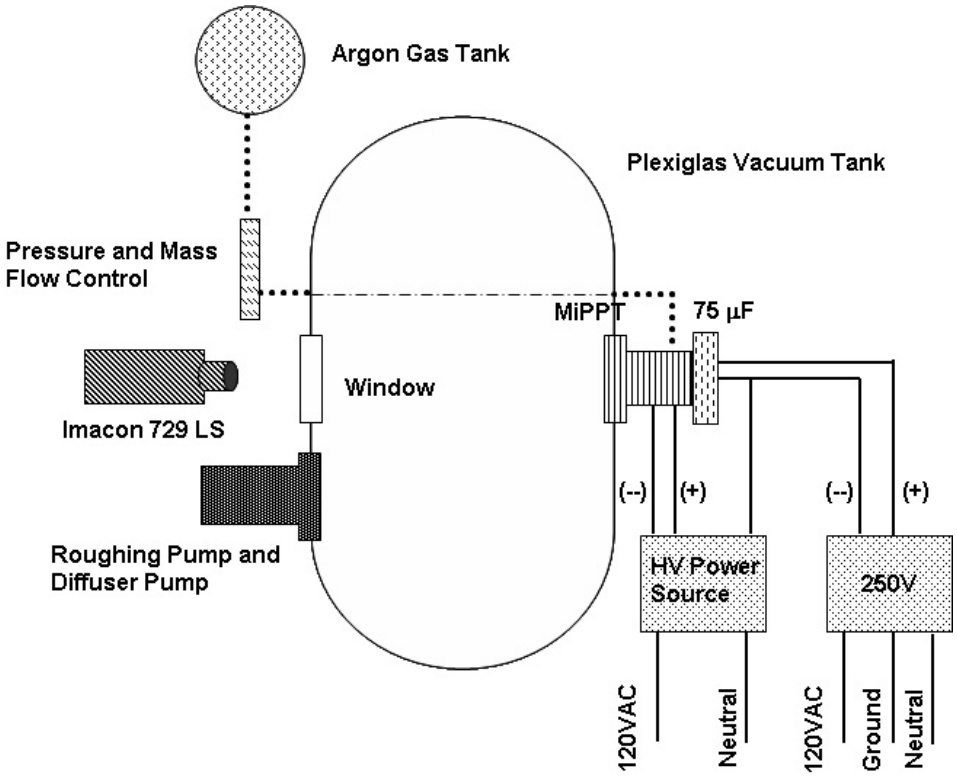

Figure 4.9: Simplified Experimental layout of the current sheet visualization experiment. A 75 uF capacitor charged to 250V is constantly monitored by an oscilloscope; the oscillatscope triggers the Imacon 729 LS ultra-high speed camera to capture current sheet of MiPPT. Missing from this schematic are the water cooling lines, the high speed oscilloscope, and the Stanford pulse generator.

One of the defining performance parameters of gas-fed pulsed plasma thrusters is the inductance of their system. In order to maximize the current flow

from the capacitors to the cathode and across the electrode gap, the inductance of the system would need to be minimized. To determine the frequency response of the current flow during a discharge, one would need to solve the second order LRC circuit equation with an AC source (see Eq. 4.1).

$$L\frac{\partial^2 q}{dt^2} + R\frac{dq}{dt} + \frac{q}{c} = V. \qquad \text{Eq. 4.1}$$

By solving the differential equation for the charge of the system, *q*, one could then differentiate the charge to determine the inductance. Finally, solving the second order differential equation results in three well-known responses: the case of an underdamped, overdamped, and critically damped system. The eigenvalue which determines the response of the system can be given by Eq. 4.2.

$$\Delta = R^2 - 4\frac{L}{C} \qquad \text{Eq. 4.2}$$

Case 1: When $\Delta < 0$, system response is over-damped.
Case 2: When $\Delta = 0$, system response is critically damped.
Case 3: When $\Delta > 0$, system response is under-damped.

While experimentally measuring the inductance of the MiPPT is fairly difficult to accomplish, one can measure the current flow and the voltage drop across the capacitors. With voltage and current flow measurements, one could also determine the resistance of the plasma and the inductance of this system by solving Eq. 4.1 and using proper numeric integration techniques (i.e., adaptive Lobatto quadrature integration technique). The resistance of the plasma can be derived simply from the definition of current and the well known relation V=IR (see Eq. 4.3).

$$R_{plasma}(t) = \frac{\frac{1}{C}\int I(t)dt}{I(t)} = \frac{Q_{total}}{C * I(t)} \qquad \text{Eq. 4.3}$$

The results from current and voltage drop measurements can be seen in Figure 4.9. Initially, when gas breaks down, one notices a sharp voltage drop, indicating a high instantaneous change in current with respect to time. One will also notice that the frequency response of the current flow is heavily over-damped; the current settles down to zero nearly after one period. Based on calculations on the resistance and inductance of the system, the eigenvalue of Eq. 1 is approximately -0.004, suggesting an over-damped system and confirming the data obtained.

The resistance of the plasma and cathode-capacitor circuit is around 200 mOhm with a standard deviation of 150 ohm. With a high standard deviation, the actual resistance of the plasma can vary from 0 – 500 mOhm, with a confidence interval of 95%. Relative to plasma resistances observed in previous GFPPTs, these resistance values are rather comparable; past GFPPTs have resistances ranging from 0 to 1 Torr. In terms of inductance, inductance of the MiPPT varies for different test conditions (see Table 4.2). Nevertheless, these values are relatively high compared to SRL GFPPT designs (<10 nH) **[2]**. This is partially due to the extended length between the cathode and capacitor and the inherent inductance in the wire connecting the cathode to the capacitors. Future design modifications will attempt to reduce this value, thus increasing the instantaneous current flow.

From Figure 4.9, the maximum current flow peaks around 2 kAmps and the discharge time occurs over a period of 20 μsec. In previous SRL discharges, maximum current flow is on the order of 20 kAmps with a discharge time of approximately 6 μsec. This suggests that the MiPPT current sheet takes much longer to develop and is much weaker than previous GFPPT designs, leading to a lower thrust output. This can be partially due to the high inductance of the system as well as the resistance of the plasma. Nevertheless, neglecting the performance aspect of the MiPPT, the goal of this project is to demonstrate current sheet uniformity. With a sluggish discharge, it still difficult to determine whether a current sheet has actually formed. During a discharge, one can observe a bright

flash of light followed by microwave breakdown in the resonant cavity. In previous studies, a bright flash of light is indicative of a current sheet, but it can also mislead one into believing that they have established a current sheet, when all they are observing is light being emitted from a low arc discharge. In order to truly determine whether a current sheet has formed, an ultra high speed camera capable of capturing at MHz rate, such as the Imacon 729 LS described above, would need to be focused onto the cathode-anode gap.

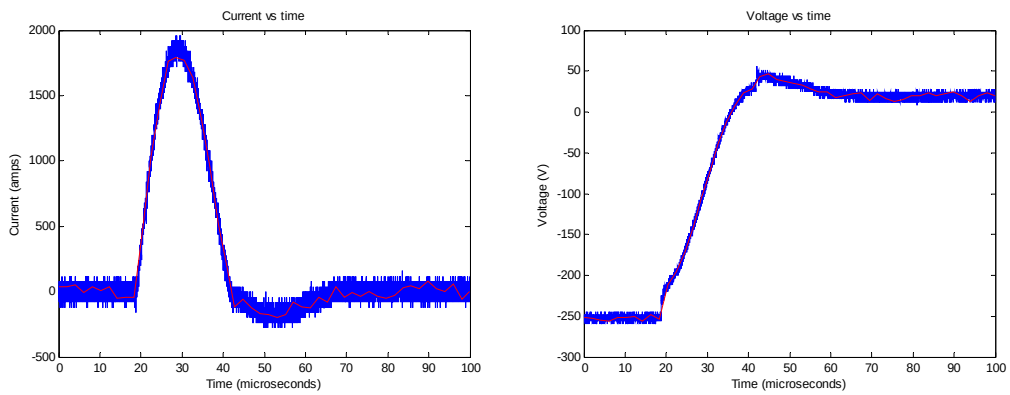

(a)

Figure 4.9(a): Current flow and voltage drop across the capacitor during a 2.3 J discharge. The blue curve represents actual data points; the red curve correspond to the spline smoothing function used to isolate noise and calculate resistance and inductance of plasma**. (a)** 9.0 Torr gas inlet pressure and 0.70 mg/sec mass flow rate.

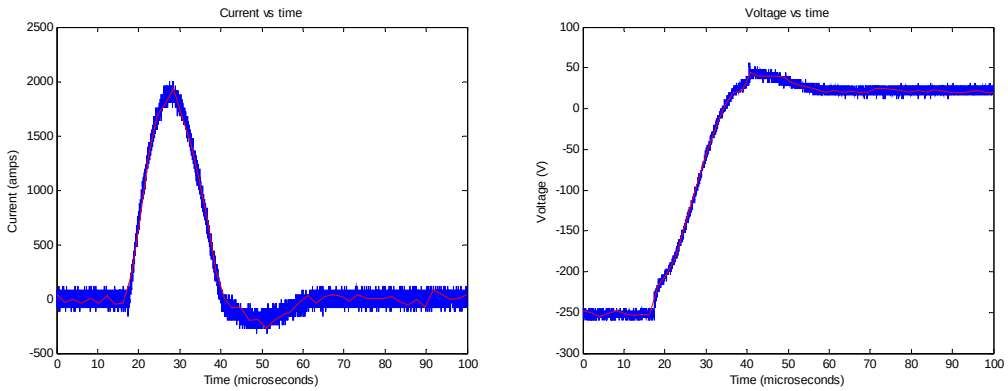

(b)

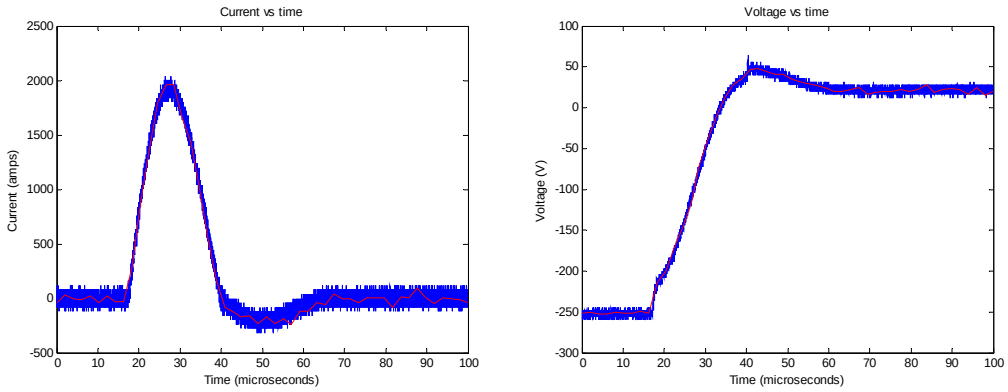

(c)

Figure 4.9: Current flow and voltage drop across the capacitor during a 2.3 J discharge. The blue curve represents actual data points; the red curve correspond to the spline smoothing function used to isolate noise and calculate resistance and inductance of plasma**. (b)** 10 Torr gas inlet pressure and 1.1 mg/sec, and **(c)** 13 Torr gas inlet pressure and 1.4 mg/sec.

Table 4.1: Mean Resistance of the Plasma and Discharge Circuit During a 2.3 J Discharge

Pressure and Mass Flow Rate	Mean Resistance (mOhm)	Standard Deviation (mOhm)
9.0 Torr, 0.70 mg/sec	190	150
10 Torr, 1.1 mg/sec	200	160
13 Torr, 1.4 mg/sec	190	160

Table 4.2: Mean Inductance of the Plasma and Discharge Circuit During a 2.3 J Discharge

Pressure and Mass Flow Rate	Mean Inductance (nHenry)	Standard Deviation (nHenry)
9.0 Torr, 0.70 mg/sec	840	~ 0 (10^{-10})
10 Torr, 1.1 mg/sec	690	~ 0 (10^{-10})
13 Torr, 1.4 mg/sec	1200	~ 0 (10^{-10})

For comparative purposes, the test conditions under which high speed images should be taken mimics test conditions of previous GFPPTs experimentation. Using previous studies of GFPPT as a reference point, the conditions under which these images should be taken range from a steady mass flow rate of 0.002 mg/sec to 2.0 mg/sec and a pulse energy of 2.5 J to 4.7 J **[3]**. Since the MiPPT can operate at a mass flow rate as low as 0.70 mg/sec and as high as 1.7 mg/sec with an energy pulse of 2.3 J, images taken of the MiPPT discharge can be directly compared to the images of previous GFPPTS (i.e., SRL PT-V).

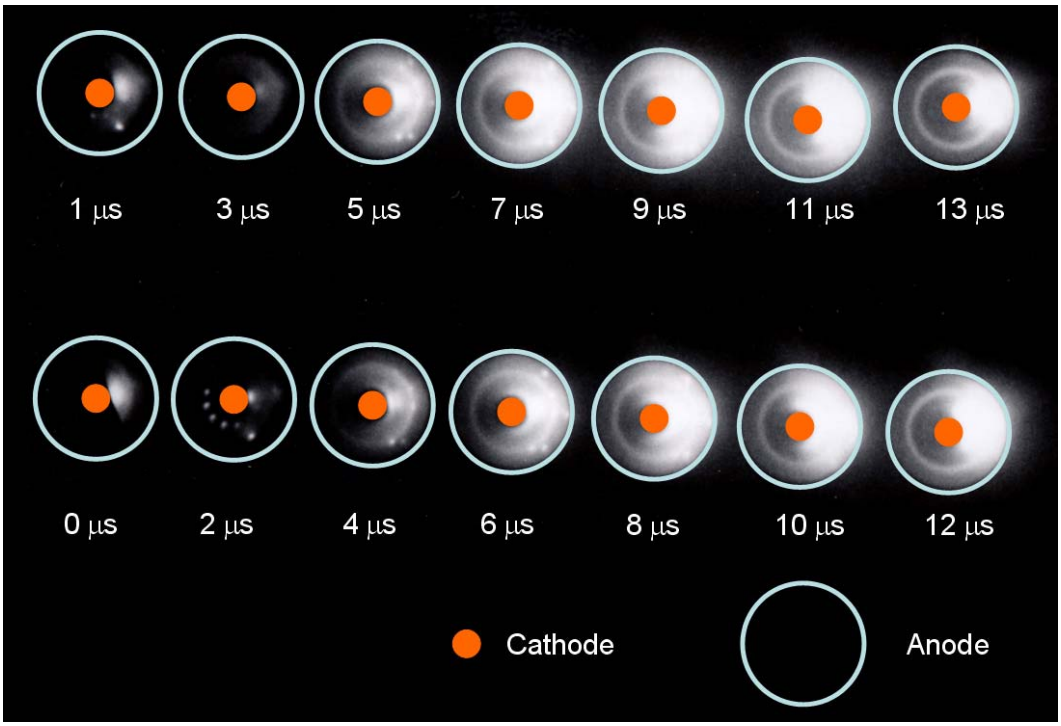

(a)

Figure 4.10 Current sheet visualization of a 2.3 J discharge with a steady state mass flow rate of 1.4 mg/sec. **(a)** Development of current sheet with time. An arc discharge can be observed in one corner of the center cathode, which initiates a breakdown between the electrodes. The visible ring around center cathode shows the location of the pre-ionized injection ports.

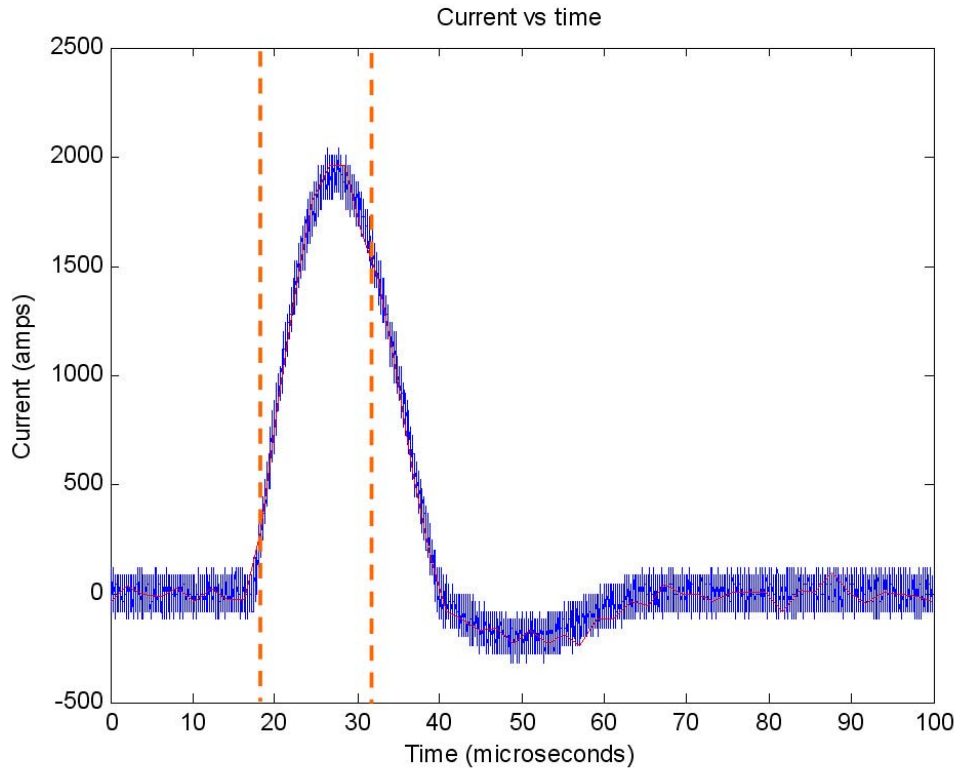

(b)

Figure 4.10 Current sheet visualization of a 2.3 J discharge with a steady state mass flow rate of 1.4 mg/sec. **(b)** Time frame of the captured images. The region between the dashed orange lines indicates when the Imacon camera is fired.

The results from high speed imagery of a current sheet development can be seen in Figure 4.10. Based upon the light intensity between the electrodes, it is evident that a current sheet has actually structuralized when pre-ionized plasma is injected into the electrodes gap. However, there are several peculiar details concerning the development of current sheet. The first detail is that that initial

discharge occurs in one region of the center cathode. This discharge initiates a breakdown between the electrodes which leads to the formation of a current sheet. The current sheet is non-uniform, because the initial discharge is biased in one section of the cathode. This is similar to the case of spark-initiated discharges, where initial discharges are highly localized. The reason for a biased discharge might be due to an asymmetric plasma distribution inside the resonant cavity. As seen in previous visualizations, the plasma inside the resonant cavity is denser in one region of the cavity (Figures 4.3 and 4.5). Thus, the injection of the pre-ionized plasma is non-uniform, leading to the bias seen in Figure 4.10.

There can be many explanations why the plasma distribution inside the cavity is non-symmetric, but the most apparent might be due to the geometry of the antenna. As one recalls from previous discussions about the electromagnetic wave distributions inside the cavity, the resonant mode inside the cavity is dominated by the localized field distributions around the antenna of the microwave source. If the antenna is designed to emit microwaves uniformly (such as a cylindrical stub antenna), then one would theoretically assume a uniform breakdown. However, if there are any small distortions within the geometry of the antenna, then the microwaves emitted are non-uniform, resulting in an asymmetric breakdown. Given that commercial magnetrons from microwave ovens are manufactured with the minimal cost, it is not certain that the microwaves emitted from the antenna are actually uniform.

The second detail worth discussing in the current sheet visualization is the quenching of the initial discharge. Based on Figure 4.10, the 2 μs and 3 μs frames suggest that the initial discharge is quenched, even though plasma is being injected into the electrode gap. This might be due to the high inductance of the MiPPT, which restricts the instantaneous current flow. The significance of this result is that the entire discharge is elongated and energy density per pulse is reduced. Hence, in order to obtain maximum performance, the inductance of the MiPPT would need to be reduced. Methods for reducing the inherent inductance of MiPPT are discussed in the next section of this report.

Chapter 5
Discussion and Future Design Modifications

The prototype MiPPT developed for this project is not by any means the final configuration for full scale production or immediate space application. Rather, it serves only as a test object to determine the initial operation and performance envelopes. Based upon these initial results, there are many improvements that can be made to push these envelops even further. In this following section, a discussion about implications from results and data collected in this project is going to follow. Upon insights from these data, design modifications are suggested for future development. Such modifications include tuning the resonant microwave cavity, lowering the inductance of the capacitor-cathode circuit, and designing a system architecture for pulsed MiPPT operation.

5.1 Tuning of TM_{010} Resonant Cavity

As noted in earlier sections of this report, the resonant cavity of the MiPPT prototype is designed to transfer about 200 – 300 watts of power from the magnetron antenna into gas and dielectric insertion. A good portion of this power is also dissipated as heat from the aluminum cavity. In order to design for improved antenna coupling (increasing the Q of the resonant cavity), one would need several specific equipment that are not available for this project. Specifically, one such equipment is a dual-directional coupler to measure absorbed and reflected microwave power. One should also consider incorporating a quartz tuning rod into the cavity or attempt varying the length of the antenna as a tuning method **[15]**, although data from this project has suggested that maximum antenna penetration is ideal for coupling power to the cavity.

While it hasn't been addressed in detail in this project, the tuning of the cavity plays a large role in the performance of the MiPPT. It has been experimentally shown that microwave induced breakdown for argon has a minimum breakdown potential when pressure is around 9.0 - 13 Torrs for a microwave frequency of 2.45 GHz. This operating pressure range is relatively high compared to previous GFPPT designs and the high pressure implies a high mass from flow. From compressible gas dynamics, mass flow rate across a hole increases as the back pressure increases (see Eqn. 2.21). Previous GFPPTs operates at a steady state mass flow rate as low as 0.03 mg/sec and as high as 2.0 mg/sec **[3]**. In order for MiPPT to operate at these ranges, it must reduce its operating pressure. Essentially, this would imply more power would need to be coupled to the resonant cavity in order for breakdown to occur. Hence, the tuning of the resonant cavity would need to be improved.

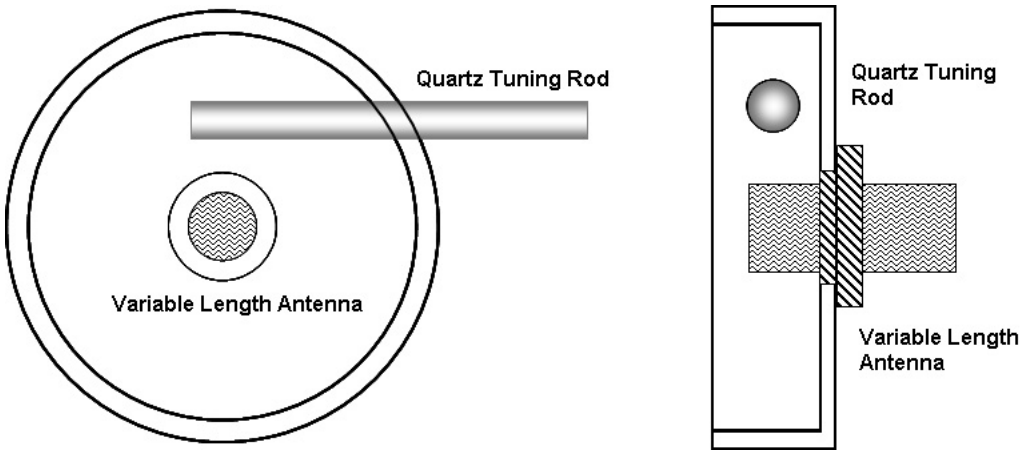

Figure 5.1: A possible tuning method for MiPPT using a quartz insertion and variable antenna insertion **[15]**. By varying the length of the quartz rod and the antenna, one could maximize the Q of the resonant cavity.

The tunning of the microwave cavity is also important when different materials are used to for the dielectric filling inside the cavity. Currently, Teflon is used to seal the gas from atmospheric conditions. Yet, as seen in previous results, the temperature inside the resonant cavity actually reaches high enough to melt the Teflon. Furthermore, thermal shocks from plasma pulses lead to fatigue and surface ablation of the Teflon. For long missions, this becomes a limiting factor in the life-span of MiPPT, since the Teflon can fail once the surface is ablated away. Hence, one design modification is to either use different dielectrics, such as machine-able ceramics, or have a hollow quartz tube segregate gas and plasma from the Teflon filling (Figure 5.2). This way, the Teflon is protected and not ablated.

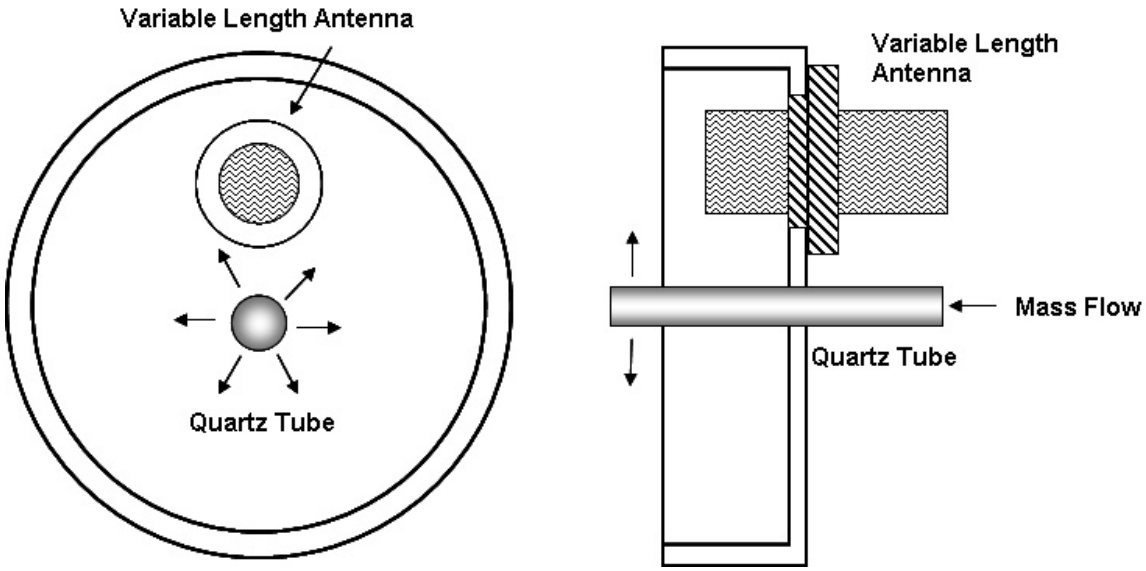

Figure 5.2: Using a quartz tube to contain gas and plasma inside the MiPPT resonant cavity **[15]**.

5.2 Minimizing MiPPT Inductance

Based upon current and voltage measurements, the inductance of the prototype MiPPT is 600-1000 nHenry. In comparison, the inductance of past of GFPPTs is usually less than 10 nHenry **[3]**. As previously discussed, the inductance of the system is critical to development of a current sheet which ionizes and accelerates neutral gas. In the past, careful attention has been taken to reduce the inductance in nearly every aspect of the capacitor-cathode circuit of the SRL family of GFPPTs (i.e. PT-V). This includes a direct attachment between the cathode and anode without use of wires. Furthermore, the design of internal capacitors is also configured to minimize induction by employing a multi-layered-coaxial configuration.

Unlike previous designs of GFPPTs, the initial design of the MiPPT prototype does not emphasize on minimizing the inductance. This is partially because the goal of the initial design is to test the concept of the MiPPT, and not to optimize performance. From CAD designs of the MiPPT, one notices that the capacitors are completely separated between the magnetron and microwave cavity. To connect these components in series, a wire is used to connect the capacitors to the case of the magnetron, which is connected to the resonant cavity and cathode. By using a wire to connect the capacitors to the cathode, this specific design adds impedance to the circuit. In order to reduce the inductance, one would need to remove the wire and redesign the capacitors such that it's directly coupled to the microwave cavity. With the current MiPPT design, the magnetron is too large to allow the capacitors to mount directly to the cathode. To overcome this challenge, one could replace the magnetron with a co-axial transmission one. As one recalls, a co-axial transmission line excites the same resonant mode as a stub antenna of a magnetron; it also couples with the cavity well enough to transfer a good deal of power. Hence one feasible way is to redesign the thruster is to couple a magnetron into a waveguide and then couple a co-axial transmission from the waveguide to the cavity.

5.3 System Architecture of MiPPT Pulsed Operation

The final phase of design for the MiPPT prototype is to demonstrate pulsed MiPPT operation. Pulsing the MiPPT would require critical timing schemes to allow sufficient time to charge the capacitors and efficient use gas propellants. With previous GFPPTs, the pulsed timing scheme is as follows **[3]**:

1) Capacitors are fully charged to their maximum potential.
2) A pulse of gas is injected into a mixing chamber where they are mixed and diffuse into the cathode and electrodes.
3) Spark plugs discharge and induce undervoltage breakdown.
4) After current sheet forms and accelerates out through the electrode gap, capacitors charge up to their full potential and the pulse takes place again.

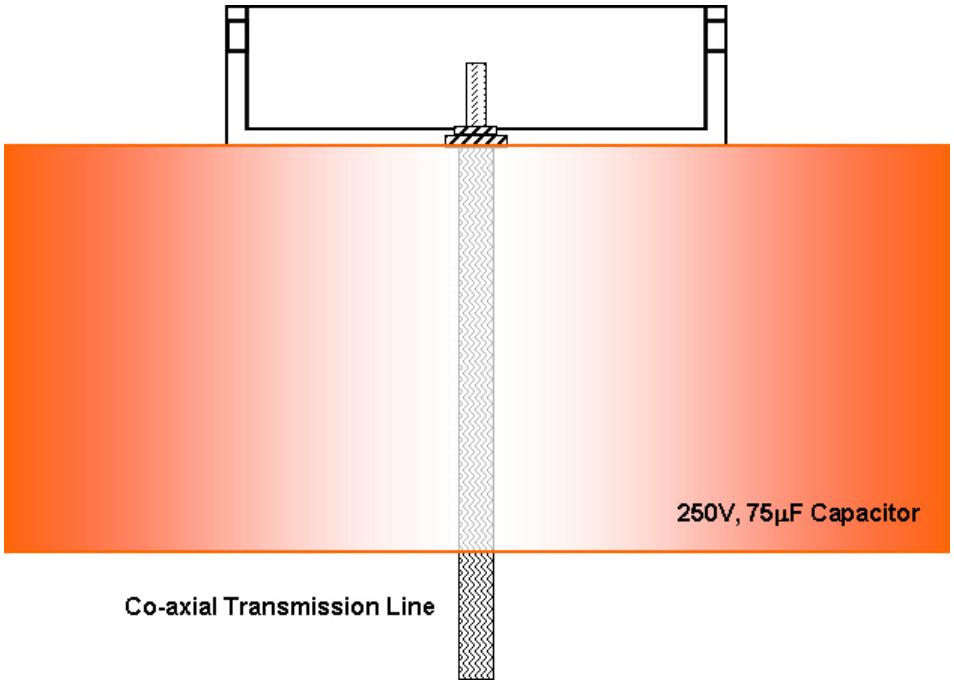

Figure 5.3: Potential MiPPT cavity and cathode design to reduce inductance by using a co-axial transmission line. The capacitor is mounted directly onto the resonant cavity and cathode. The capacitor also has a hollow center, which the co-axial transmission line travels through.

The entire event occurs during a span of several seconds. The pulse rate is effectively determined by the charging time of the capacitors, and they are essentially limited by the internal resistance and current output of the power supply. Nevertheless, pulsing the MiPPT at a rate of several seconds per pulse is not a difficult challenge. One could essentially adopt the same pulsing scheme for GFPPTs and modify it for MiPPT. However, two additional schemes are also being considered; the first is to pulse the gas supply and leave the microwave

source at steady state; the second is to pulse the microwave source and leave the gas supply at steady sate.

In order to pulse the gas supply, a high speed actuator valve would need to control the mass flow rate. With this approach, there are two issues which one has to consider. First, based on results obtained from this project, there is a delay from the time gas is injected into the microwave chamber to the time it takes for the gas to break down. This delay is essentially associated with the transient time for the cavity pressure to rise high enough to induce microwave breakdown. The length of this delay will be critical to the performance of the MiPPT, because if it's too short, a large amount of neutral gas would be contained in the microwave cavity once a current sheet forms; if the delay is too long, a large amount of injected gas would escape the thruster without being accelerated. Controlling this delay would be a crucial, and if one is to employ a pulsing gas flow rate scheme, one needs to carefully characterize this delay. One possible method for controlling the delay time include varying the power output of the magnetron antenna. By decreasing the power of the antenna, the pressure rise would need to be higher in order for breakdown to occur, and hence, the delay is lengthened. On the other hand, by increasing the power output, the pressure rise would need to be lower, and thus the delay is shortened.

The pulsing scheme using pulsed gas injection has its disadvantages. The main disadvantage is the lifetime of high speed valves; one of the primary reasons why GFPPTs has not been as popular as ablative Teflon pulsed plasma thrusters is the failure of the actuation valves, which degrade over a long period of time. Another disadvantage is simply the power consumption of the magnetron when there is no gas in the system and the magnetron is simply heating the cavity.

As an alternative to this pulsing scheme, a second pulsing scheme involves pulsing the microwave source while leaving the gas flow rate constant. The advantages of this approach are simply reduced power consumption by the magnetron and unnecessary need for a high speed actuation valve. The main challenge of this approach is to determine the optimum pulsing rate of the

magnetron. With a constant gas flow rate into the cavity, mass is constantly injected into the electrode gap. If the pulse frequency is too low, gas would escape the thruster without being accelerated. On the other hand, if the pulse frequency is too high, insufficient gas would be accelerated, resulting in a low thrust bit parameter (thrust per pulse). Nevertheless, the pulse frequency is essentially determined by the charging time of the capacitors. In a simple RC circuit, the charging time is an exponentially increasing function with a time constant RC. In order to have high pulsing rate, the resistance of the system would need to be very low to allow the capacitors to charge fully before each discharge. The source of resistance between the power source and the capacitors is simply resistance in the wires and capacitors.

While both alternative pulsing schemes are easier to implement than the conventional pulse-gas, pulse-microwave scheme, it might turn out that the disadvantages of each alternative pulsing scheme offset their advantages. If this is the case, the pulsing scheme for the MiPPT prototype would adopt the conventional pulsing scheme. Essentially, the scheme would be in the following steps:

1) Capacitors are fully charged to their maximum potential.
2) A pulse of gas is injected into a mixing chamber where they are mixed and diffuse through the injection ports into the cathode and electrodes.
3) Magnetron is pulsed and induces microwave breakdown in the resonant cavity. Pre-ionized plasma is injected into the electrode gap, inducing undervoltage breakdown, and a current sheet forms.
4) The current sheet accelerates down the electrode gap; after the event is over, the capacitors charge up to their full potential, and the process repeats.

Chapter 6
Conclusions

Gas-fed pulsed plasma thrusters (GFPPTs) are attractive propulsion systems for low-trust space missions. Their simple system architecture and low voltage requirement make them a reliable and competitive product for space applications. Nevertheless, even though these propulsion systems have been in operation since the 1960's, there are still improvements that can be to improve durability and performance. Over the past decade, studies have shown that GFPPT's lifespan are severely limited by their spark-ignition system used to induce undervoltage breakdown **[4]**. While a spark-ignition system is easy to implement, it is highly prone to corrosion and it has limiting capability in producing an azimuthally symmetric current sheet. Research has developed various alternative techniques to replace spark-initiation system, including a laser initiation concept **[9]**. However, given the low energy efficiency of laser technology, the practical application of laser initiation for GFPPTs does not seem too convincing.

The project described in this project explores a novel approach to undervoltage breakdown in GFPPTs using a microwave initiation system. Unlike lasers, microwave sources, such as a magnetron, can reach energy efficiencies as high as 85%. Furthermore, producing uniform current sheets in GFPPTs with microwave initiation is simply a matter of selecting a proper resonant mode. The purpose of this project is to exploit both of these advantages and to develop a microwave initiation system which could produce azimuthally symmetric current sheets and still be able to operate in the same test envelop as current GFPPT designs. The ultimate goal is to design a microwave-initiated pulsed plasma thruster (MiPPT) that is ready for immediate space applications.

The design infrastructure of the MiPPT is essentially the same as conventional GFPPTs. The design concept of using a microwave-initiation system is to inject pre-ionized plasma in a uniform pattern into the cathode-anode gap to induce undervoltage breakdown. The goal of this concept is to have undervoltage breakdown occur symmetrically. When this occurs, the capacitor bank connected in series to the cathode of the MiPPT will discharge, releasing a high current flow between the cathode and anode. This induces an arc discharge and the result is a symmetric current sheet, which acts upon the (J x B) Lorentz Force to accelerate down the electrode gap. In the process, it also ionizes and accelerates neutral gas particles, thus producing an impulsive force on the MiPPT.

One of the first challenges of this thesis is to design a microwave cavity which would serve as the pre-ionization chamber for the MiPPT. The specific geometry of this cavity determines the resonant mode at which the electromagnetic fields will be distributed inside the cavity. When the electric field strength exceeds the breakdown potential inside this cavity, breakdown will occur with the densest plasma regions located around the highest electric field intensities. The resonant mode selected for this cavity is TM_{010}, and through theoretical calculations, the dimensions needed to sustain this mode are 94 mm in diameter and 25 mm in length. The strongest electric fields are located along the center axis of the cylinder, with the strongest magnetic fields around the perimeter of the cylinder. This pre-ionization chamber also serves as the mixing chamber,

where gas are premixed and injected into the electrode gap at sonic speeds using an annular hole pattern.

While theoretical calculations predict that the resonant mode has a transverse magnetic field distribution and an axial electric field distribution, the exact field distribution is going to vary once the geometry of the cavity is distorted. Since holes have to be made for gas injection and antenna protrusion, the cavity can no longer be treated as an ideal configuration. In order to determine the field distribution, a finite element model is made using Comsol Multiphysics (Femlab) to analyze the all these effects on the field distribution of the cavity. Results indicate that the regions of highest electromagnetic field intensities lie along the stub antenna of the microwave source. Since the electromagnetic fields of the antenna dominate the resonant fields in the cavity, it is difficult to determine the resonant mode. Nevertheless, using a smaller antenna model, one can see that the exact field distribution does not vary much from a TM_{010} resonant mode. Furthermore, an additional model using a co-axial probe is analyzed for possible future applications of a co-axial microwave source. The results suggest that the field intensities are greatest around the antenna, but the resonant mode still resemble a TM_{010}.

Initial attempts to produce microwave plasma are unsuccessful, because tuning of the cavity is poor. Tuning is adjusted by increasing the antenna insertion depth, and it has been found that power transferred to the cavity varies directly with antenna depth. With a better tuned cavity, microwave plasma has been produced at conditions ranging from 9.0 Torr gas pressure to 15 Torr gas pressure and a mass flow rate of 0.70 mg/sec to 2.0 mg/sec, respectively. A series of experiments is then developed to determine the resistivity of the plasma. Results show that plasma forms initially for about 100 – 150 microseconds before it quenches. It reappears when the power density of the cavity is large enough to induce a secondary breakdown (about 2 milliseconds later). One possible explanation for this phenomenon is the de-tunning effects of the plasma on the microwave cavity; since plasma is a conductor, this significantly alters the Q-factor of the resonant cavity when it initially forms.

Once the resistivity of the microwave plasma has been determined, a new set of experiments is developed to look for current sheet formation with a microwave initiation system. Results show that a current sheet appears when microwave plasma is injected into the electrode gap, indicating that microwave initiation is successful. Time-dependent measurements of the current and voltage across the capacitors indicate that the frequency response of the current flow is highly damped with maximum current flow reaching as high as 2000 amps. Nevertheless, high speed imagery of the current sheet suggests that current sheet formation is biased, leading to an asymmetric current sheet. Previous experiments indicate that the plasma distribution inside the cavity is non-asymmetric, which explains the bias.

While the first phase of development of MiPPT is now complete with the successful production of a current sheet, there are still future design modifications that need to be implemented to maximize the performance of MiPPT. One modification is to increase the Q-factor of the microwave cavity such that discharge can be achieved under lower gas pressure conditions. This will allow the MiPPT to operate in the lower test envelop of conventional GFPPTs. Another improvement is to increase the inductance of the thruster. One approach is to attach the capacitors directly onto the microwave cavity and use a co-axial transmission line to transfer microwave energy to the cavity. Finally, the next phase of development for the prototype MiPPT is to design a system architecture for pulsed operation.

The results and data presented in this paper shows that the MiPPT is a major step forward in the development of GFPPTs. Not only has the MiPPT been able to successfully initiate undervoltage breakdown, it can also operate in the same test envelop as conventional GFPPTs. Moreover, with a microwave-initiation source, corrosion is no longer be a limiting factor is the life-span of GFPPTs. Both of these advantages, along with the energy efficiency of microwave sources, are compelling reasons why research and development of MiPPT should be continued in the future.

Appendix

A.1 Table of Zeros of Bessel Function of First Kind

Mode	Mth Zero	Of	Value of x
TE_{11}	1	$J'_1(x)$	1.84
TM_{01}	1	$J_0(x)$	2.40
TE_{21}	1	$J'_2(x)$	3.05
TM_{11}	1	$J_1(x)$	3.83
TE_{01}	1	$J'_0(x)$	3.83
TE_{31}	1	$J'_3(x)$	4.20
TM_{21}	1	$J_2(x)$	5.14
TE_{41}	1	$J'_4(x)$	5.32

A.2 MiPPT CAD Schematics

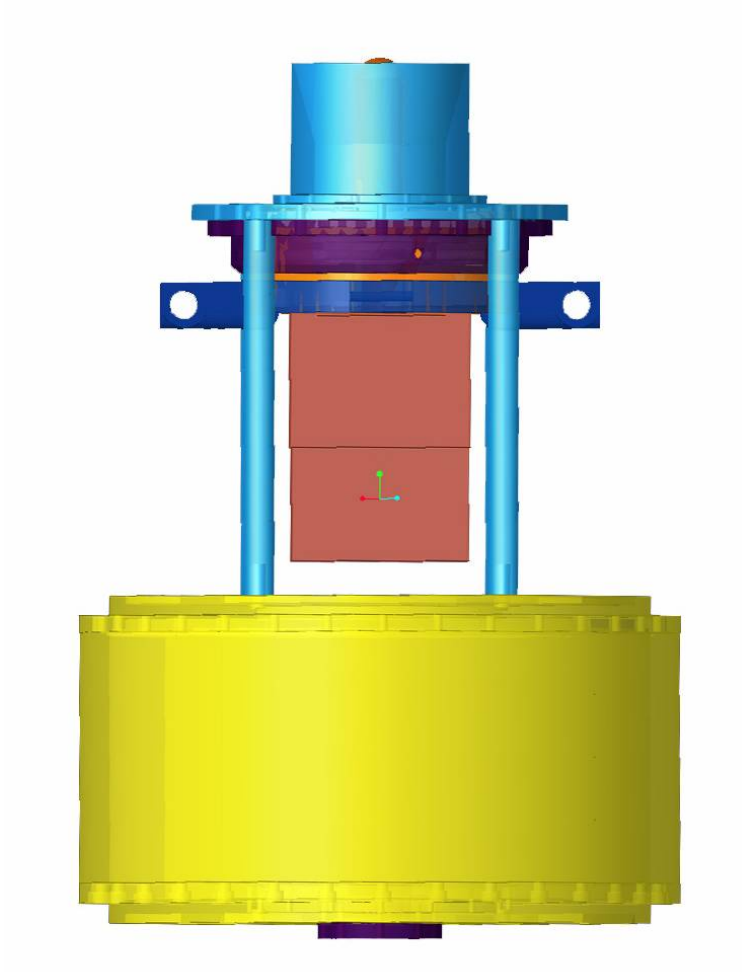

Figure A.2.1 CAD schematic of the MiPPT with all components. In the pages that follow, each component is drawn in greater detail with specific dimensions.

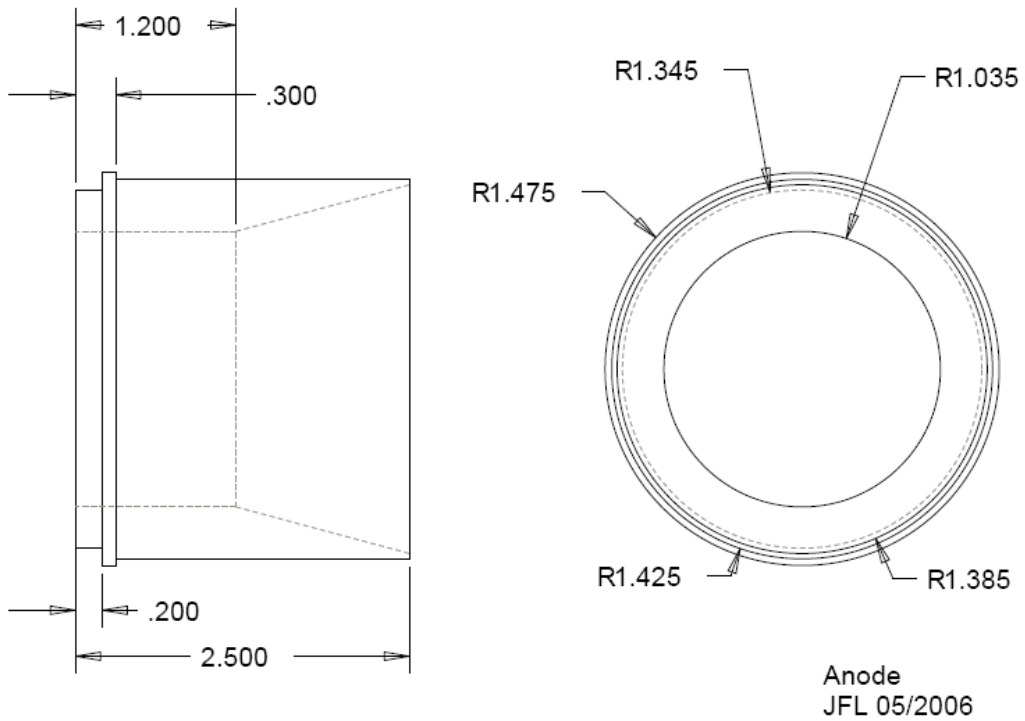

Figure A.2.2 Anode.

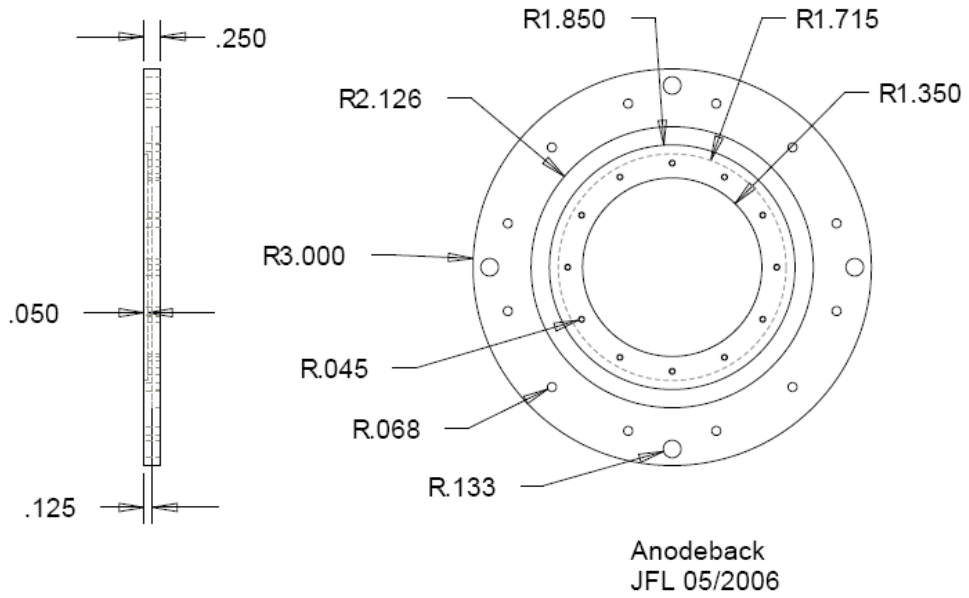

Figure A.2.3 Anodeback.

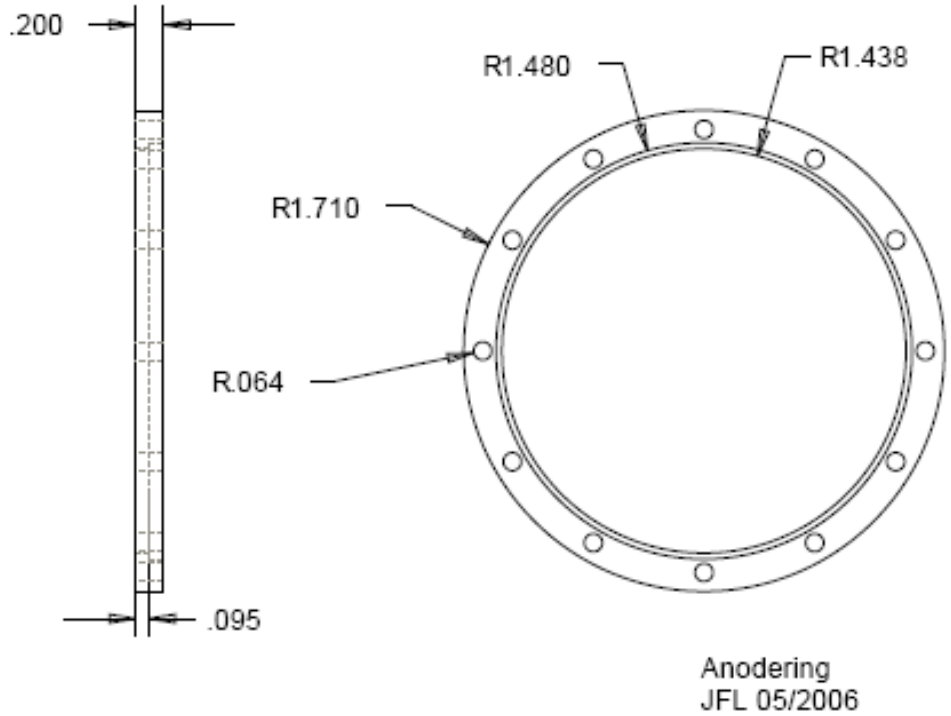

Figure A.2.4 Anodering.

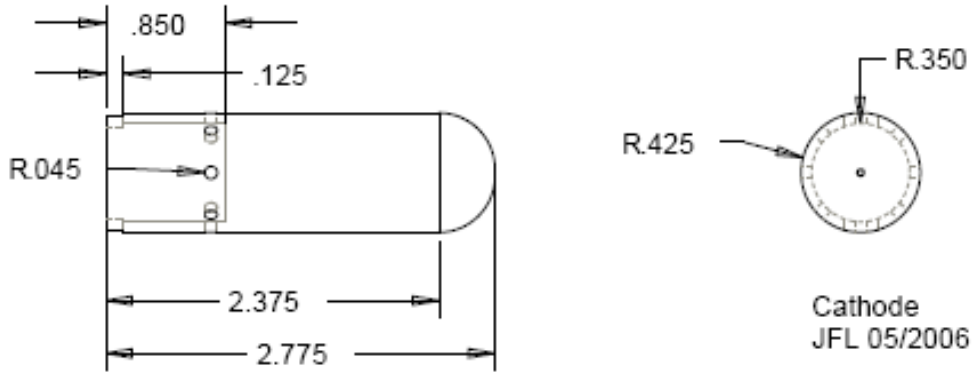

Figure A.2.5 Cathode.

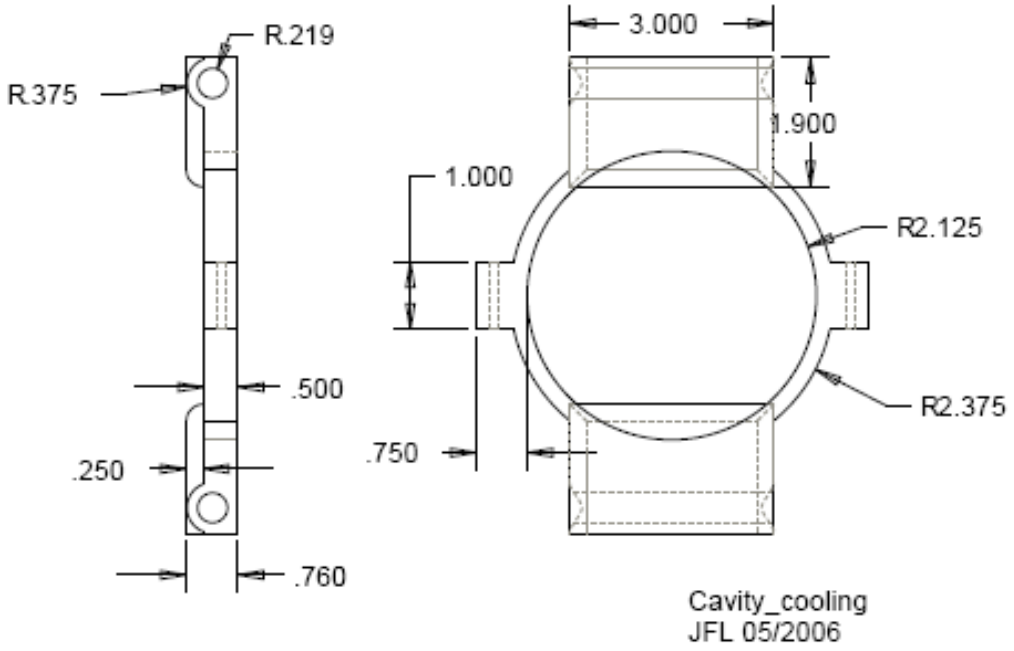

Figure A.2.6 Cavity_cooling.

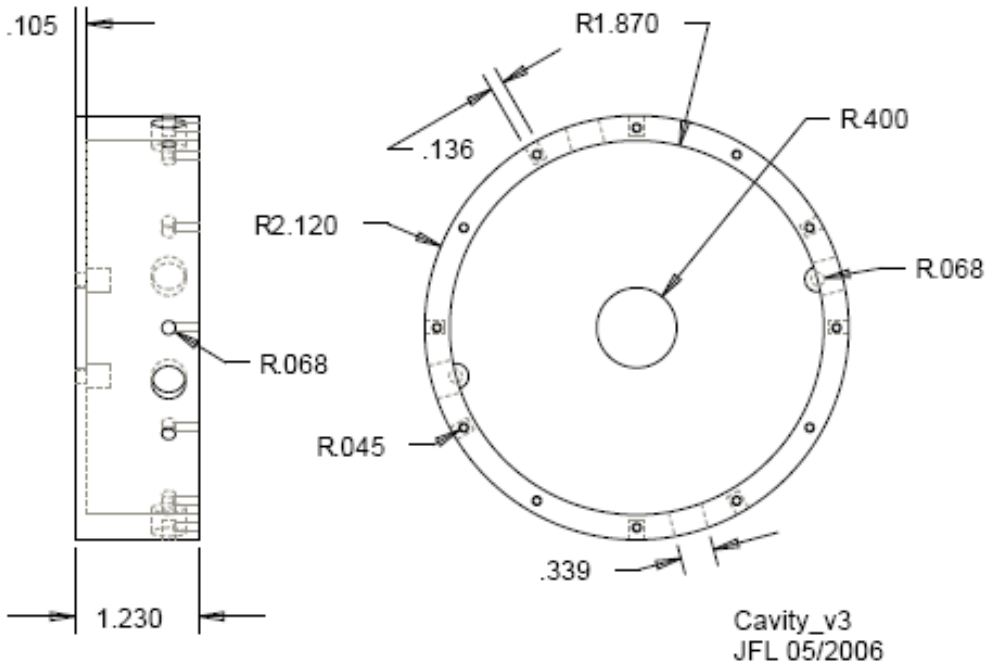

Figure A.2.7 Cavity_v3.

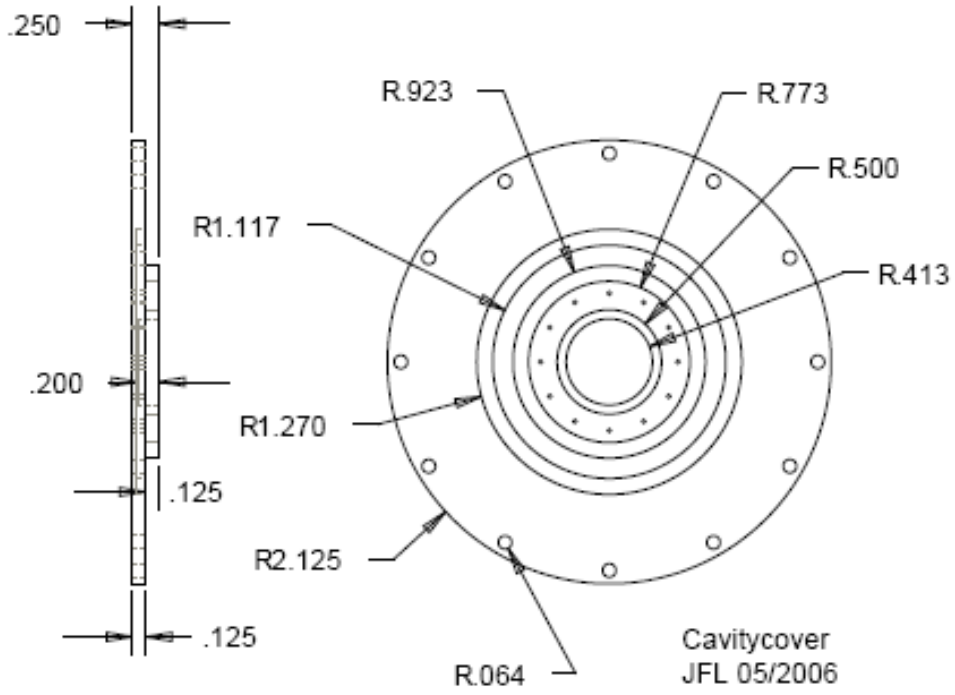

Figure A.2.8 Cavitycover.

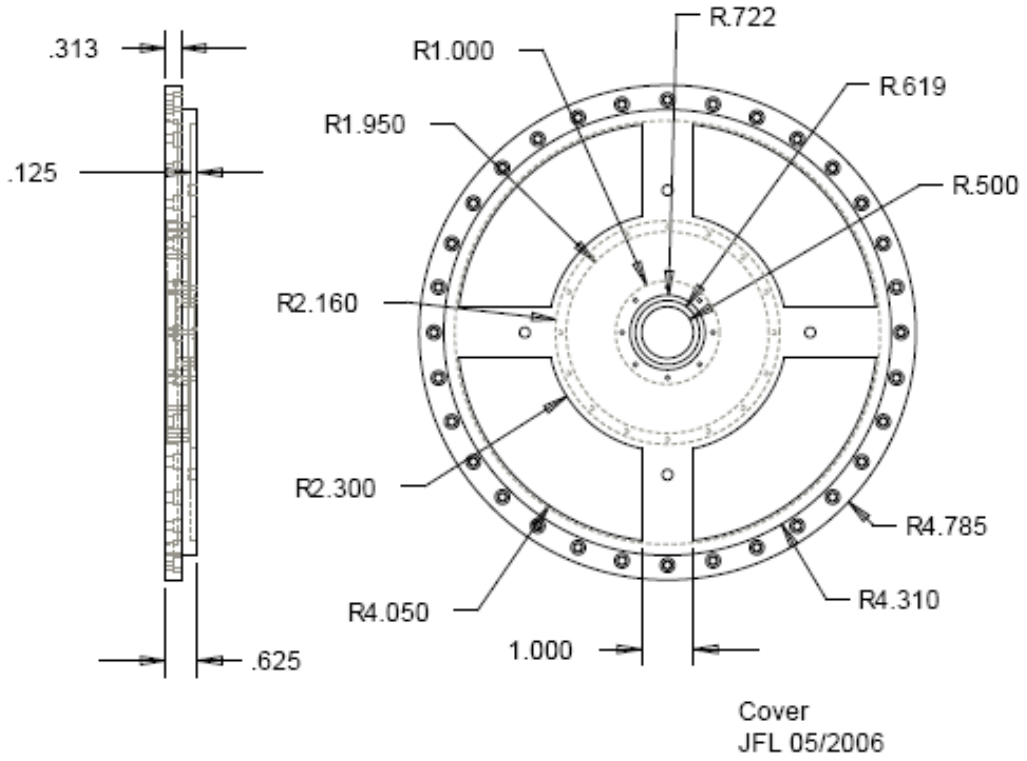

Figure A.2.9 Cover.

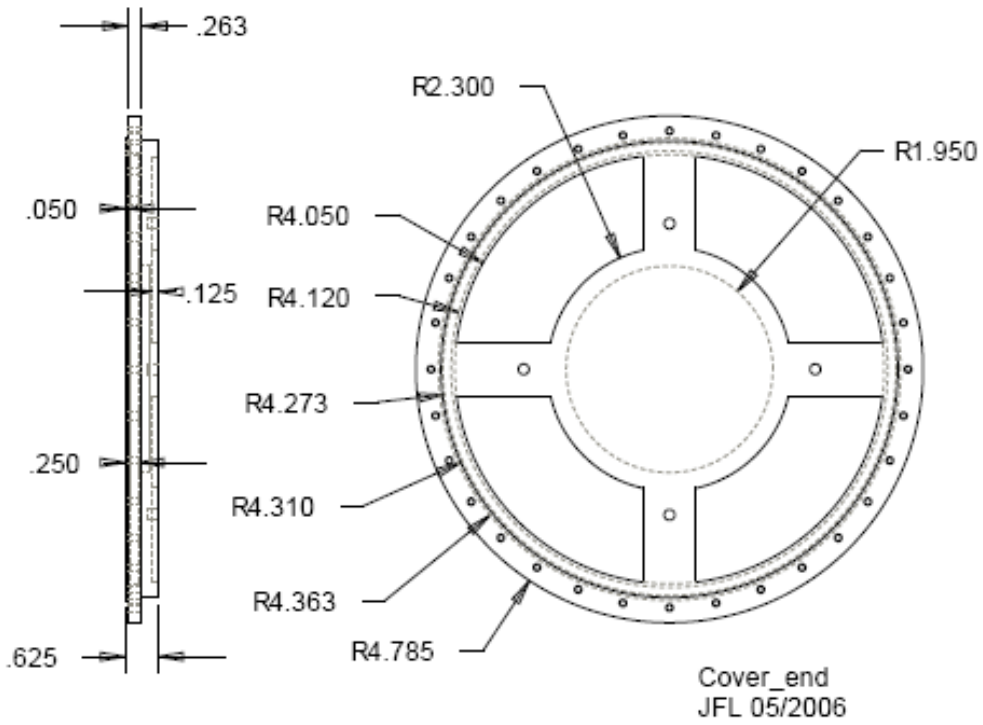

Figure A.2.10 Cover_end.

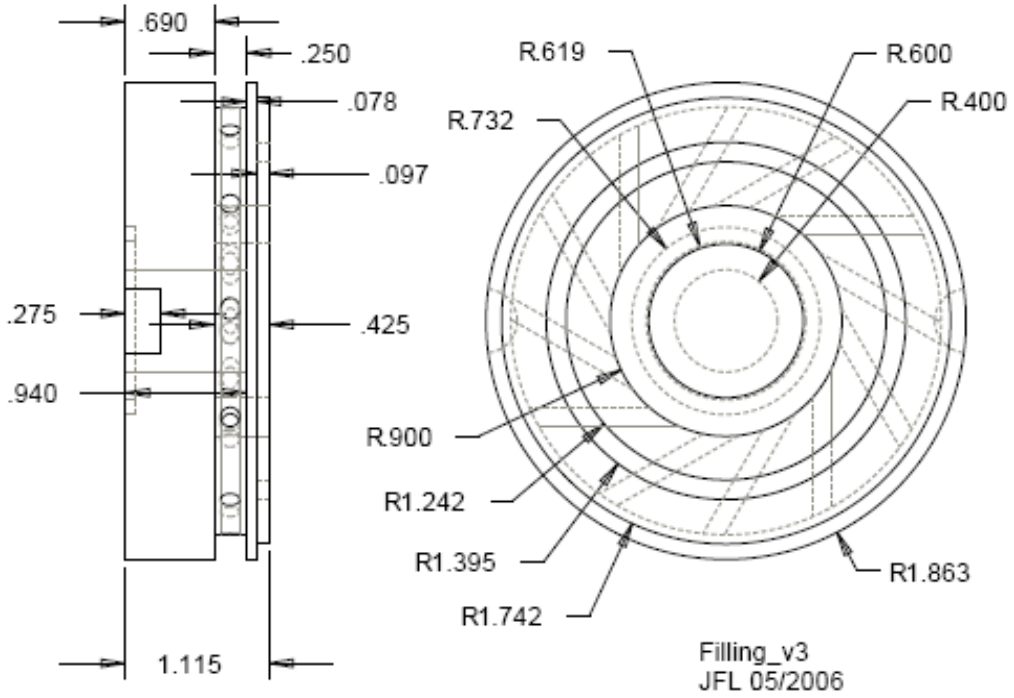

Figure A.2.11 Filling_v3.

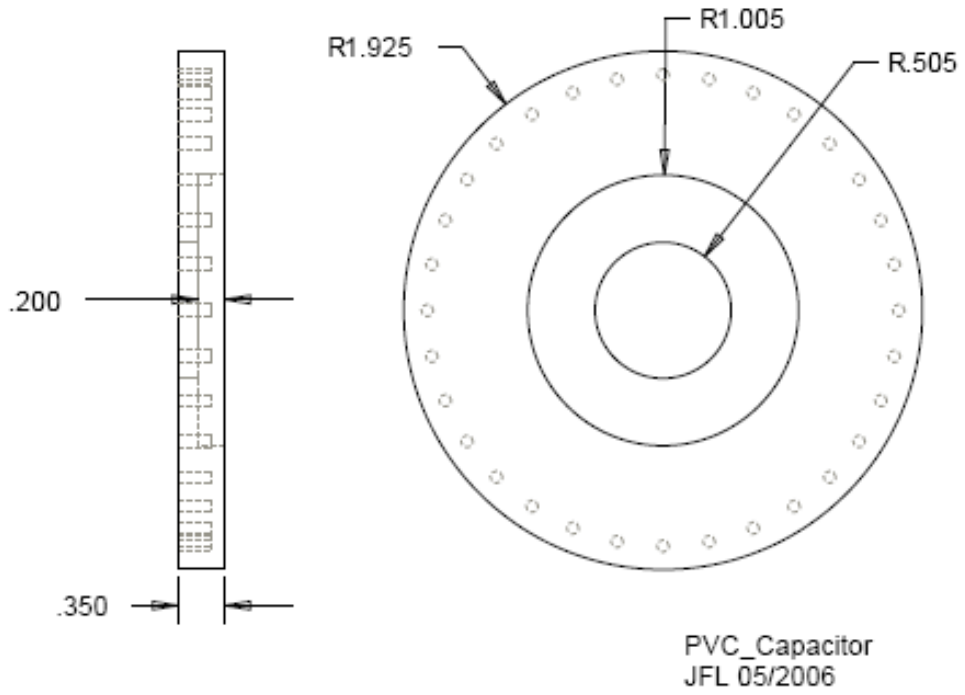

Figure A.2.12 PVC_Capacitor.

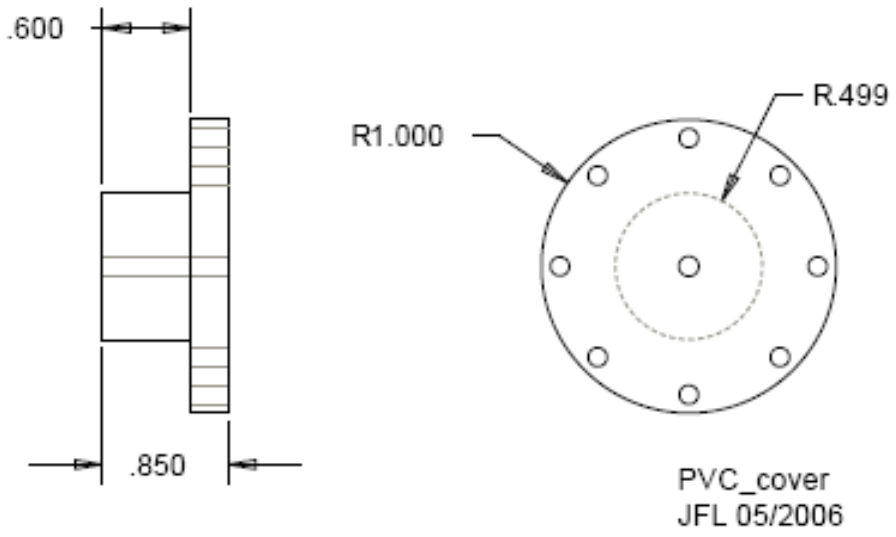

Figure A.2.13 PVC_Cover.

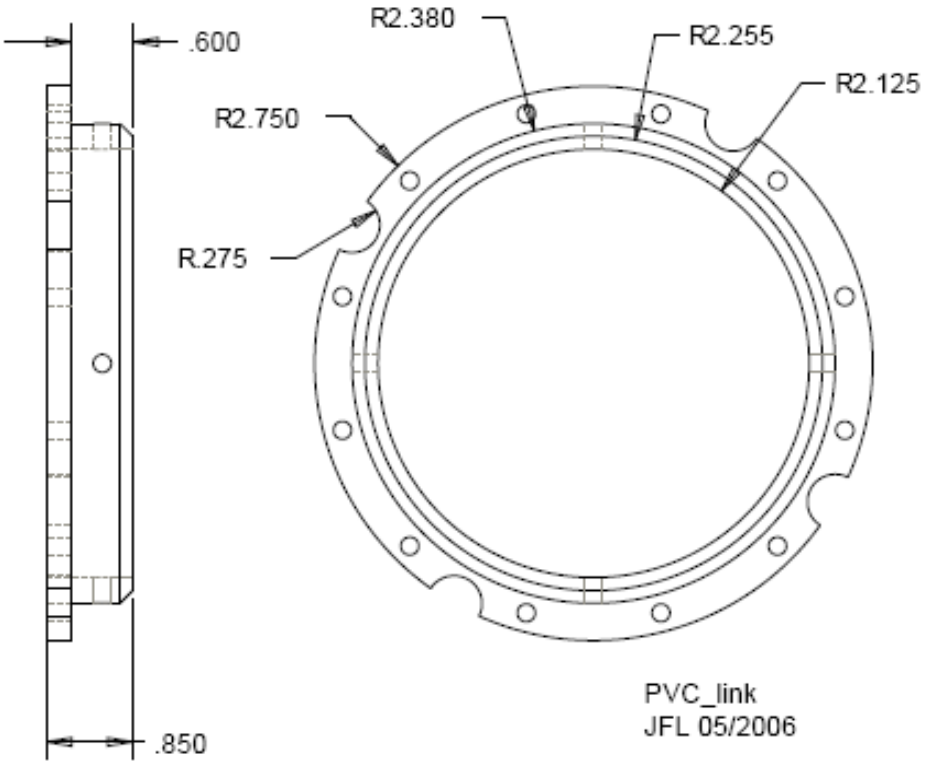

Figure A.2.14 PVC_link.

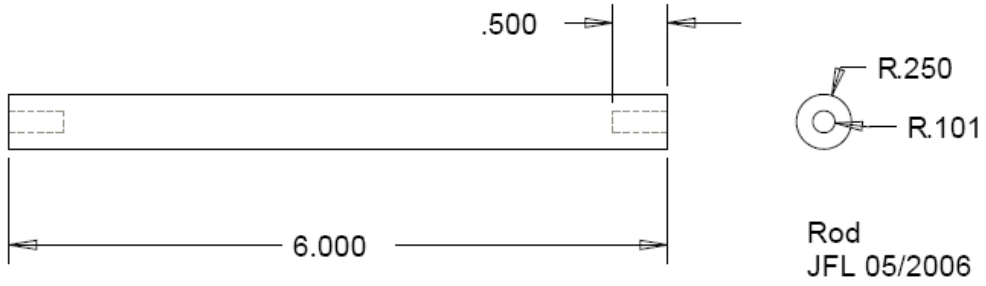

Figure A.2.15 Rod.

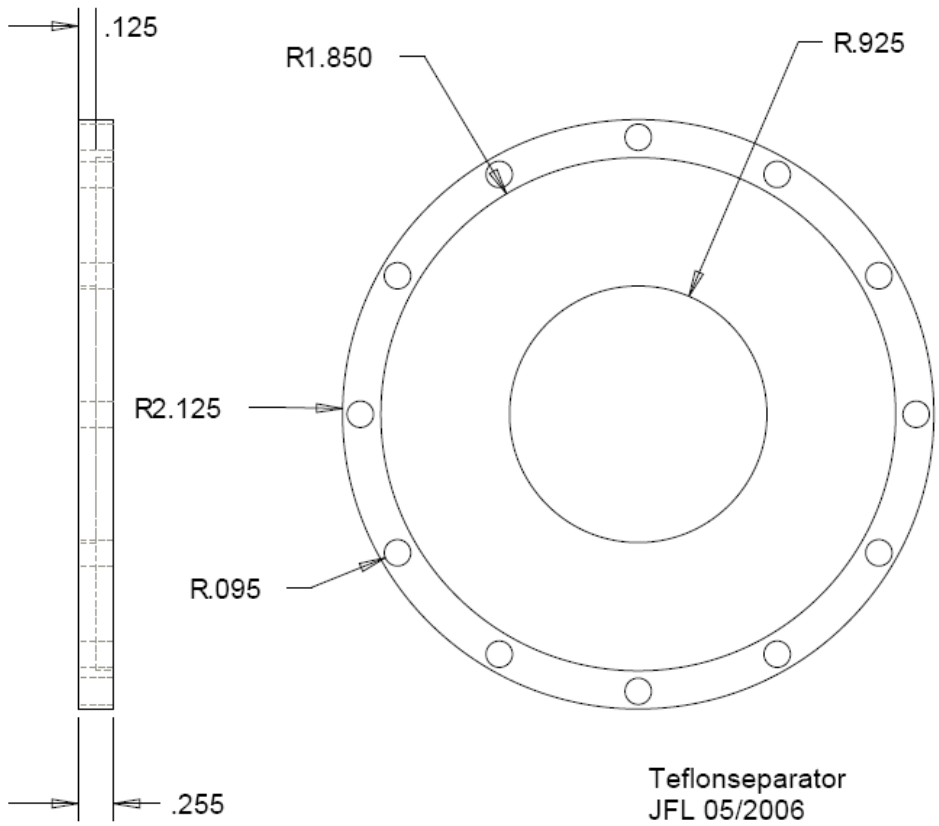

Figure A.2.16 Teflonseparator.

A.3 Supplementary Imacon Photographs

These additional images are provided solely for future reference. These images follow the same imaging format as Figure 4.10. Hardcopies of these photographs can be obtained from the Princeton University Electric Propulsion and Plasma Dynamics Laboratory.

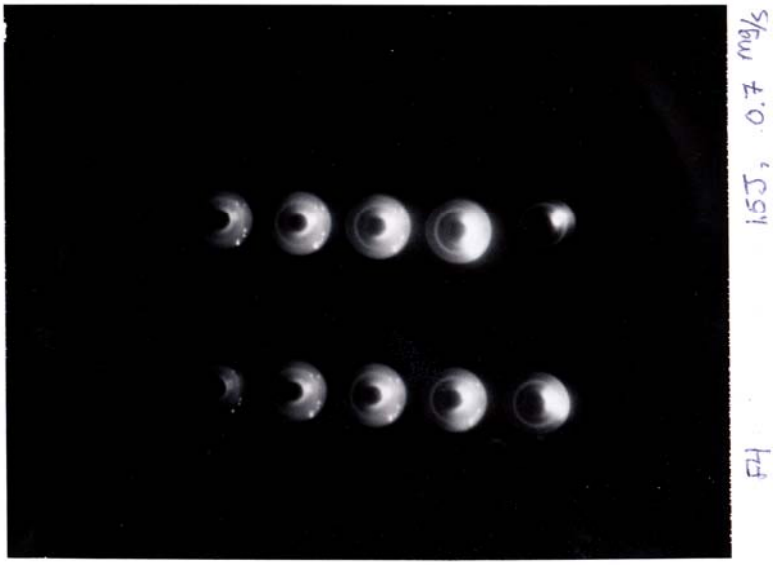

Figure A.3.1 Current sheet for a 1.5 J discharge, 9.0 Torr cavity pressure, 0.70 mg/s steady state mass flow rate, and F4 camera aperture.

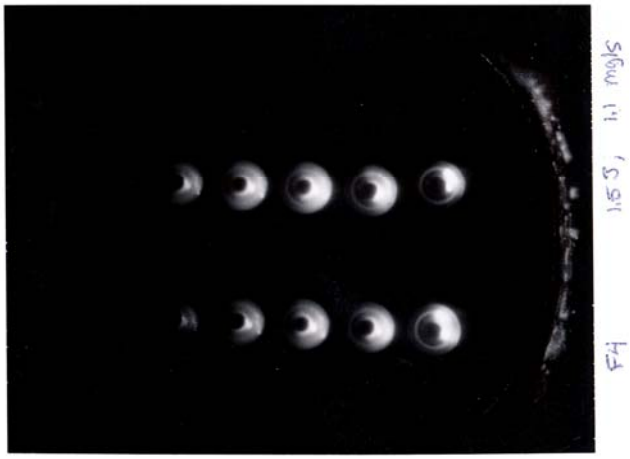

Figure A.3.2 Current sheet for a 1.5 J discharge, 10. Torr cavity pressure, 1.1 mg/s steady state mass flow rate, and F4 camera aperture.

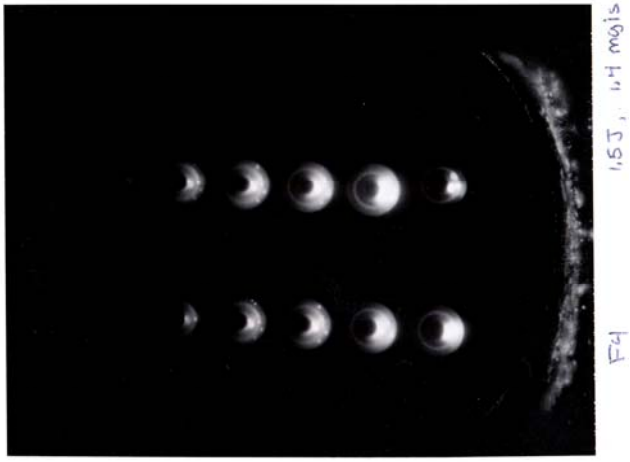

Figure A.3.3 Current sheet for a 1.5 J discharge, 13 Torr cavity pressure, 1.4 mg/s steady state mass flow rate, and F4 camera aperture.

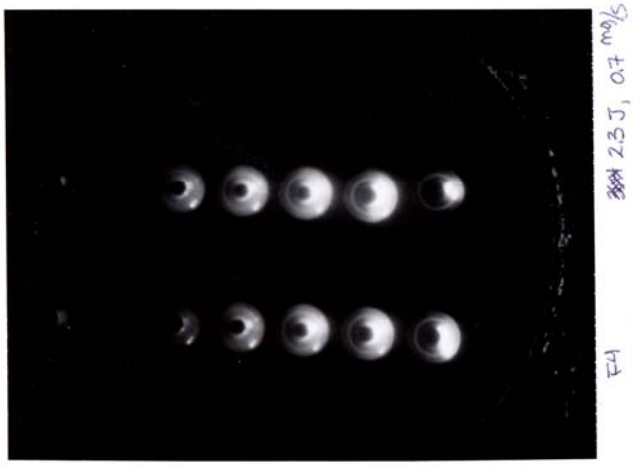

Figure A.3.4 Current sheet for a 2.3 J discharge, 9.0 Torr cavity pressure, 0.70 mg/s steady state mass flow rate, and F4 camera aperture.

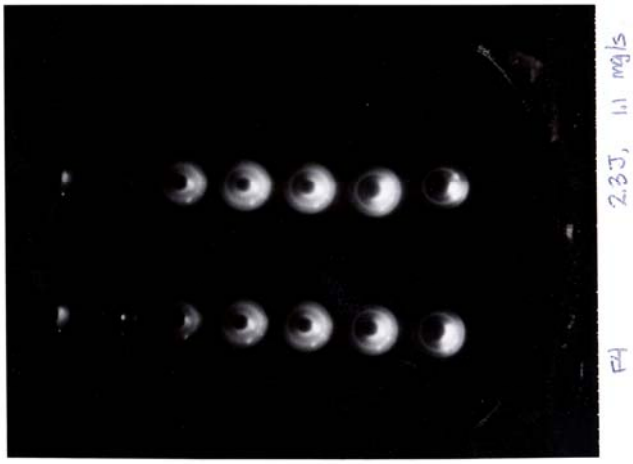

Figure A.3.5 Current sheet for a 2.3 J discharge, 10. Torr cavity pressure, 1.1 mg/s steady state mass flow rate, and F4 camera aperture.

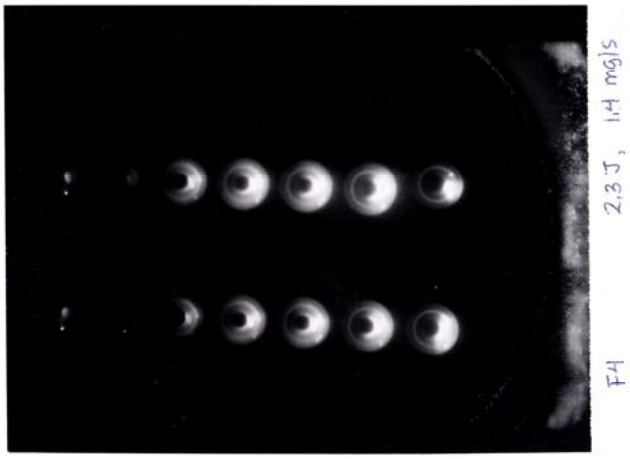

Figure A.3.6 Current sheet for a 2.3 J discharge, 13 Torr cavity pressure, 1.4 mg/s steady state mass flow rate, and F4 camera aperture.

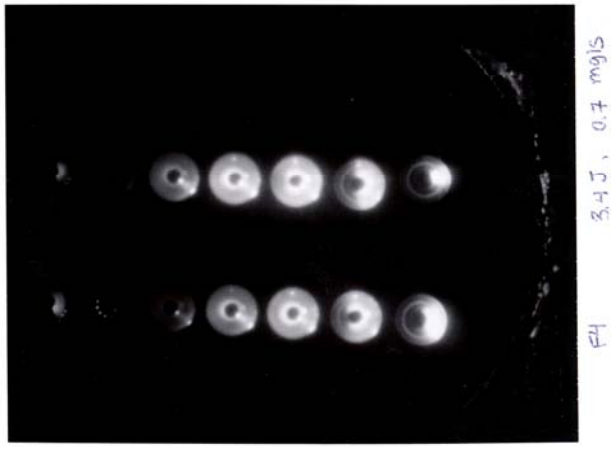

Figure A.3.7 Current sheet for a 3.4 J discharge, 9.0 Torr cavity pressure, 0.70 mg/s steady state mass flow rate, and F4 camera aperture.

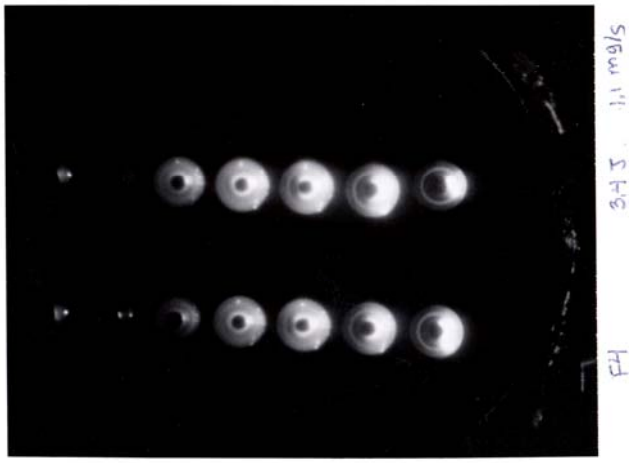

Figure A.3.8 Current sheet for a 3.4 J discharge, 10 Torr cavity pressure, 1.1 mg/s steady state mass flow rate, and F4 camera aperture.

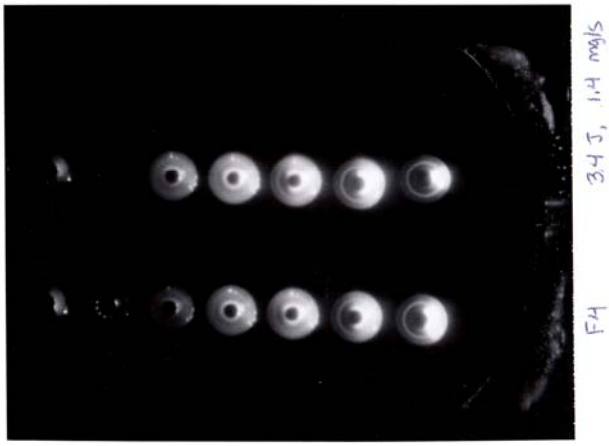

Figure A.3.9 Current sheet for a 3.4 J discharge, 13 Torr cavity pressure, 1.4 mg/s steady state mass flow rate, and F4 camera aperture.

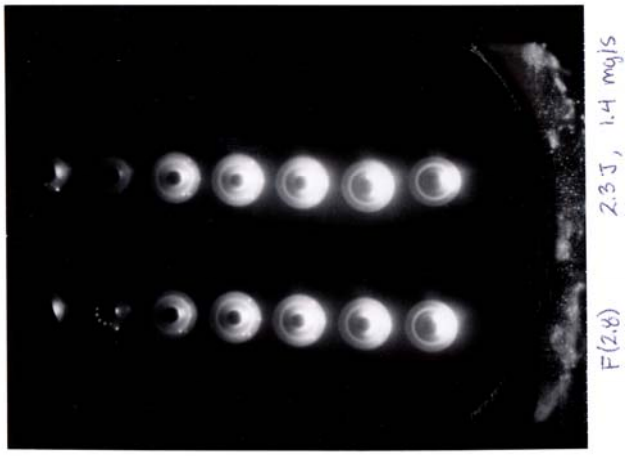

Figure A.3.10 Current sheet for a 2.3 J discharge, 13 Torr cavity pressure, 1.4 mg/s steady state mass flow rate, and F2.8 camera aperture.

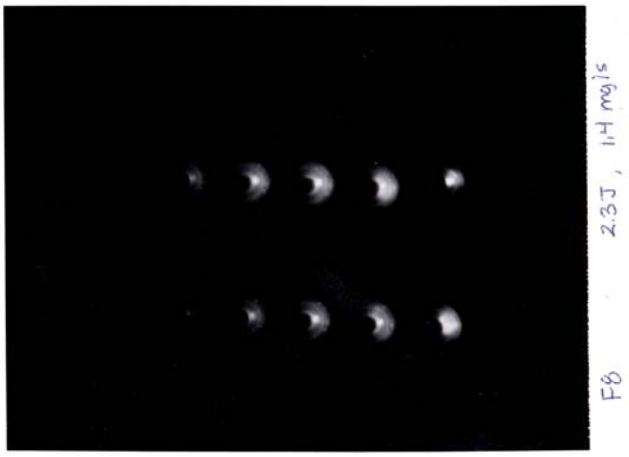

Figure A.3.11 Current sheet for a 2.3 J discharge, 13 Torr cavity pressure, 1.4 mg/s steady state mass flow rate, and F8 camera aperture.

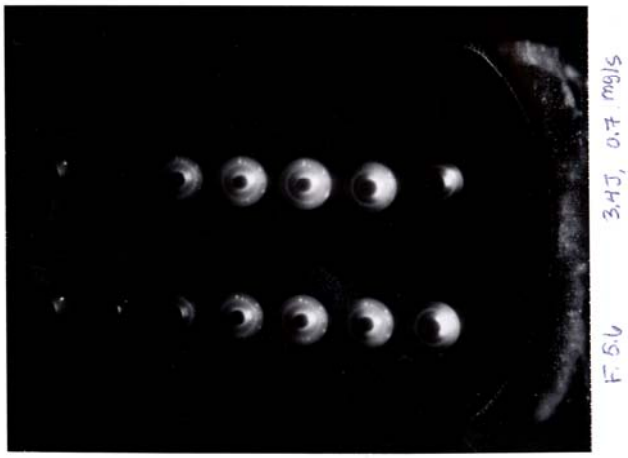

Figure A.3.12 Current sheet for a 3.4 J discharge, 9.0 Torr cavity pressure, 0.70 mg/s steady state mass flow rate, and F5.6 camera aperture.

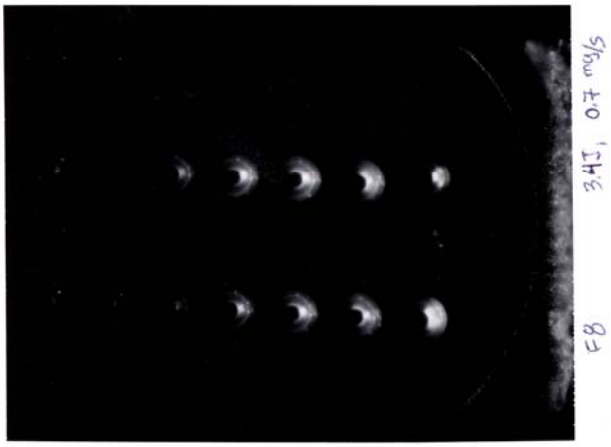

Figure A.3.13 Current sheet for a 3.4 J discharge, 9.0 Torr cavity pressure, 0.70 mg/s steady state mass flow rate, and F8 camera aperture.

References

[1] Sutton, G.P. Biblarz, O. Rocket Propulsion Elements. John Wiley and Sons, Inc. New York, 2001.

[2] Ziemer, J.K. Choueiri, E.Y. "Performance Characterization of a High Efficiency Gas-Fed Pulsed Plasma Thruster." AIAA-97-2925. 33rd Joint Propulsion Conference, Seattle, WA. 1991.

[3] Ziemer, J.K. "Scaling Laws in Gas-Fed Pulsed Plasma Thrusters." PhD Thesis, Department of Mechanical and Aerospace Engineering, Thesis No. 3016-T, Princeton University, Princeton, NJ 2001.

[4] Zimer, J.K. "Effects of Ignition on Discharge Symmetry in Gas-Fed Pulsed Plasma Thrusters." AIAA-98-3808. 34th Joint Propulsion Conference, Cleveland, OH. 1998.

[5] Cooley, J.E. "IR-Assisted Discharge Initiation in Pulsed Plasma Thrusters." AIAA-2002-4274. 38th AIAA Joint Propulsion Conference, Indianapolis, IN. 2002.

[6] Sullivan, D.J., Micci, M. M. "Performance Testing and Exhaust Plume Characterization of the Microwave Arcjet Thruster." AIAA-94-3127. 30th Joint Propulsion Conference, Indianapolis, IN. 1994.

[7] Chiravalle, V.P. A Numerical and Experimental Study of a Two-Stage Microwave Electrothermal Thruster for Spacecraft Propulsion. Ph.D Thesis, Princeton University, 2003.

[8] Zimer, J.K. "Effects of Ignition on Discharge Symmetry in Gas-Fed Pulsed Plasma Thrusters." AIAA-98-3808. 34th Joint Propulsion Conference, Cleveland, OH. 1998.

[9] Cooley, J.E. "IR-Assisted Discharge Initiation in Pulsed Plasma Thrusters." AIAA-2002-4274. 38th AIAA Joint Propulsion Conference, Indianapolis, IN. 2002.

[10] Sullivan, D.J. *Development and Performance Characterization of a Microwave Electrothermal Thruster Prototype.* Ph.D. Thesis, Pennsylvania State University, 1995.

[11] Baden Fuller, A.J. "Microwaves: An Introduction to Microwave Theory and Techniques." Pergamon Press., 1979.

[12] Zimmerman, D.C. "Two-Dimensional Ion Velocity Distribution Functions in Inductively Coupled Argon Plasma." Plasma Sources Sci. Tech.. Vol 14. 581-588, 2005.

[13] Raizer, Y.P. *Gas Discharge Physics.* Springer-Verlag, 1997.

[14] http://en.wikipedia.org/wiki/Magnetron. May 02, 2006.

[15] Beenakker, C.I.M, Bosman, B. Boumans, P.W.J.M. "As Assessment of a Microwave-Induced Plasma Generated in Argon with a Cylinderical TM010 cavity as an excitation source of emission spectrometric analysis of solutions." Spectrochimica Act, Vol. 33B., 373 – 381, 1978.

[16] van Dalen, J.P.J. "Improvements of the Cylindrical TM010 cavity for an atmosphercica pressure microwave-induced plasma.

[17] Drawin, H.W., Emard, R. "Influences of Atom-Atom Collisions on the Collisional-Radiative Ionization and Recombination Coefficient of Helium Plasma." Z. Physik, vol.254, 202-217; 1972.

[18] Vlcek, J. "A Collisional-Radiative Model Applicable to Argon Discharged Over a Wide Range of Conditions. I: Formulation and basic data." Journal of Physics D: Applied Physics. Vol 22, 623-631, 1989.

[19] Shiu, Y.S., Biondi, M.A. "Dissociative Recombination in Argon: Dependence of the Total Rate Coefficient and Excited-State Production on Electron Temperature." Physical Review A. Vol 17, 3, March 1978.

[20] Smith, H.B., Charles, C., Boswel, R.W. "Breakdown Behavior in Radio-Frequency Argon Discharges." Physics of plasmas. Vol 10, 3. March 2003.